Microstructural Response of Magnesium Alloys : 3D Crystal Plasticity and Experimental Validation

by

Sriram Ganesan

A dissertation submitted in partial fulfillment
of the requirements for the degree of
Doctor of Philosophy
(Aerospace Engineering and Scientific Computing)
in The University of Michigan
2017

Doctoral Committee:

Associate Professor Veera Sundararaghavan, Chair
Professor John Edmond Allison
Associate Professor Samantha Hayes Daly, University of California, Santa Barbara
Professor Krishnakumar R. Garikipati
Professor John A. Shaw

Dream, Dream Dream, Dreams transform into thoughts.

And thoughts result in action.

A.P.J. Abdul Kalam

Sriram Ganesan

sriramg@umich.edu

ORCID iD: 0000-0002-8765-7544

To all my teachers and my beloved family

ACKNOWLEDGEMENTS

I would like to express my sincere gratitude to my thesis advisor Professor Veera Sundararaghavan. He has always been a source of inspiration and guidance throughout my stay at the University of Michigan. I will always be thankful for the amount of freedom he has provided me along the course of this research. His gracious guidance, valuable suggestions, and understanding nature have helped me the most in the successful completion of the present work.

I would like to thank all my committee members Professors John Allison, Samantha Daly, Krishnakumar Garikipati and John Shaw for serving on my committee. I have been privileged to be a part of the Center for PRedictive Integrated Structural Materials Science (PRISMS) under the leadership of Prof. Allison, who has been a guiding force in my research. I am thankful to Prof. Daly and members of the Daly group, Alan Githens and Dr. Zhe Chen for sharing data and insights on the wonderful experiments on Magnesium alloys, which form the backbone of my thesis. I am thankful to Prof. Garikipati for introducing me to the open-source finite element software deal.II through a course on Advanced Finite Element Methods. I would like to thank Prof. Shaw for his time and efforts to serve on my committee and his suggestions to improve my work. My special thanks to Prof. Rudraraju who has guided me through the development of PRISMS-Plasticity and for always providing ideas and encouragement in my research. I would also like to thank my advisor from IIT Kanpur, Prof. Chandrashekhar Upadhyay for igniting my interest in solid mechanics and mentoring me through my studies.

I gratefully acknowledge the funding support provided by the U.S. Department of Energy, Office of Basic Energy Sciences, Division of Materials Sciences and Engineering under Award #DE-SC0008637 as part of the Center for PRedictive Integrated Structural Materials Science (PRISMS) at the University of Michigan.

I would like to thank all my MSSL lab mates for their help and support throughout the years: Aaditya, Abhishek, Adam, Ali, Arunabha, Christian, Nick, Pinar, Jiangyi, Shang, Shardul and Siddhartha. I would also like to thank all the current and past members of the labs of Professors Allison, Daly, Garikipati, Jones and Waas for insightful discussions on mechanics. I would like to acknowledge the services of Advanced Research Computing at the University of Michigan over the years. My special thanks to graduate coordinator, Denise Phelps and Bonnie Bryant for their immense help throughout my studies.

I would also like to express my gratitude to friends and family from Michigan who have made this journey a delightful and memorable one: Abhishek, Adam, Anna, Anurag, Ashwani, Christian, Clara, Corin, Daniel, Doga, Michael, Nishant, Pinar, Prashanth, Priyam, Puneet, Riddhimann, Ritika, Rohit, Shardul, Ziyang, Sriram and Meenakshy. My officemates Abhishek, Andrew, Anna, Chih-Kuang, Corin, Nhung and Sneha have always made the workplace livelier over the years. I have wonderful memories of organizing the SPICMACAY events and thank all the team members over the years. My special thanks to all members of my hostel-wing and friends from IIT Kanpur who have always been a source of support for me.

Finally, I would like to thank my parents, sister, and family for their continued blessings and support throughout my time away from home.

TABLE OF CONTENTS

CHAPTER

LIST OF FIGURES

FIGURE

LIST OF TABLES

TABLE

LIST OF APPENDICES

Appendix

ABSTRACT

Chair: Veera Sundararaghavan

Lightweight materials such as Aluminum are prevalent in aerospace and automotive vehicles, but the use of lighter Magnesium alloys will significantly increase fuel efficiency and cut emissions. Magnesium alloys present a wide array of unsolved scientific challenges, such as the deformation response of the slip and twin systems and the influence of dislocation interactions and twinning on tensile and fatigue behavior. In this thesis, a parallel three-dimensional(3D) crystal plasticity finite element open-source code was developed based on the deal.II finite element framework as part of PRISMS-Plasticity. Rate-independent crystal plasticity was implemented by developing a nonlinear algorithm which enables all the slip systems to lie on or inside the yield surface, and a consistent tangent modulus ensures convergence for small loading increments. A twin activation mechanism was incorporated into the framework based on a quadrature point sensitive scheme. Furthermore, by bounding the L^2-norm of the plastic-slip, load-step adaptivity is enabled. The code demonstrates parallel performance and scaling on large-scale problems running on hundreds of processors.

Using experimental microstructure images as input, the code has been used to compute, validate and investigate response of crystalline aggregates to mechanical loading; this leads to insights on slip and twin activity. Boundary value problems were set up to compare the displacement and strain fields obtained by Scanning Electron Microscope - surface Digital Image Correlation (DIC) experiments for Magnesium alloy WE-43 T5 and T6 tempers with the crystal plasticity finite element simulations. The results indicate a strong correlation between experiments and crystal plasticity finite element simulations.

For further insight into the material behavior and to interpret the surface observations better, it is important to know the subsurface effects on the surface behavior. 3D reconstruction of microstructures is growing to be a major topic of interest in the field of modeling and simulation for comparison with experiments. An inverse Voronoi problem approach is used to construct an approximate Voronoi representation of the surface microstructure by generating a convexified representation of the microstructure. The output is combined with random sections of Electron backscatter diffraction observations to build a 3D microstructure. Comparisons are made with surface DIC measurements for random samples of 3D microstructures and they indicate the effect of the underlying microstructure on the surface plastic strain. These developed methods will serve as powerful tools in an Integrated Computational Materials Engineering framework towards accelerating alloy development and in better understanding the mechanical behavior of materials.

CHAPTER I

Introduction

The study of micromechanisms governing strength, ductility and failure plays a key role in the development of engineering metallic alloys and the assessment of the mechanical integrity of structures. Developing damage-tolerant microstructures is essential in many fields of engineering, such as automotive vehicles or for the next generation aerospace materials. For a long time, these developments have largely remained considerably empirical. However, more recently, computational methodologies have been introduced thus leading to increased research in this field.

While new materials are being developed to provide such superior properties (often by manipulating the material at the micron-scale), it becomes more and more difficult to analyze, understand and predict their behavior with existing techniques. This is especially challenging for metals, where the industrial drive towards enhanced performance is strongest.

In this context, Integrated Computational Materials Engineering (ICME) [9] is a new field of study that emphasizes the integration of material models at multiple length and time scales enabling concurrent analysis of manufacturing, design and materials within this framework. The goal of the PRedictive Integrated Structural Materials Science (PRISMS) center at the University of Michigan, that funded this work, is to create open source software to predict microstructural evolution and mechanical behavior of materials. The PRISMS-Plasticity code, developed by the coauthor, is a parallel numerical framework for implementing continuum and crystal plasticity models critical to multiscale modeling.

Magnesium and its alloys serve as test materials to demonstrate the capability of the developed software tools. Magnesium alloys are lightweight and have a more favorable strength to weight ratio as compared to the more common aerospace material, Aluminum.

1.1 Magnesium Alloys

Magnesium is, in fact, the lightest structural metal and hence is attractive to automotive and aerospace applications [6, 75, 87]. Magnesium also has an electromagnetic interference shielding property making it suitable for electronic applications [5].

Use of Magnesium alloys in U.S. Military applications is presented in [75]. Magnesium was profoundly used in many aircraft during World War II (1939 - 1945), a key example being the B-36 bomber which had 5555 kg of magnesium sheet, which covered 25% of the exterior, 700 kg of magnesium forgings and 300 kg of magnesium castings [75].

However, corrosion behavior, particularly poor galvanic corrosion characteristics made it difficult for aerospace applications. Some of the corrosion and flammability problems were evident in the 1950s and 1960s. Many magnesium alloys also exhibit poor ductility and formability at room temperature [6, 19, 87]. Poor low-temperature formability, low fracture toughness, poor elevated temperature creep response and cost issues are other minor limitations [75]. Designers are now well aware of galvanic and general corrosion issues, and the use of high purity alloys which restrict the use of Fe, Co, Ni and Cu have improved corrosion resistance [75].

With the arrival of rare-earth containing alloys, the strength issue has been mostly resolved [75]. The formability issue is still a field of active research and here is where the models developed in this thesis are useful. Development of WE alloys (Mg-Y-rare earth) has helped produce alloys with relatively high yield and tensile strength, superior corrosion resistance and largely retained strength properties at elevated temperatures (up to 523K) [75]. Rare-earth alloying additions have also improved ductility by weakening the basal texture during rolling and extrusion processing. [54, 89]. This occurs during recrystallization after rolling or extrusion where shear bands develop in these alloys, containing nucleation sites for growth of new grains. [89]. Rare-earth alloying also improves strength by forming precipitates on crystallographic planes that disrupt the dislocation motion [73].

Magnesium casting alloys ZE41, QE22 and particularly WE43 are used to an extent in aircraft and helicopter components such as gearbox housings, compressor and filter casings, canopy and brackets [5, 32]. The most prominent current application is that of magnesium transmission and gear housings in U.S. Army and Navy aircraft such as the Sikorsky Black Hawk [75]. Therefore, Integrated computational materials engineering (ICME) [9] and design of alloys [114] can enable new design frameworks, and thus open the doors for widespread magnesium applications in aerospace and automotive industry.

1.2 Crystal Plasticity Modeling of Magnesium Alloys

Unlike the face centered cubic (FCC) materials, deformation of hexagonal close packed (HCP) material is highly anisotropic. The deformation resistances of different slip systems are different and deformation twinning also plays a major role in the plastic deformation of the material. Also, twinning is sensitive to the direction of the applied stress; therefore the yield strengths in tension and compression are different [59].

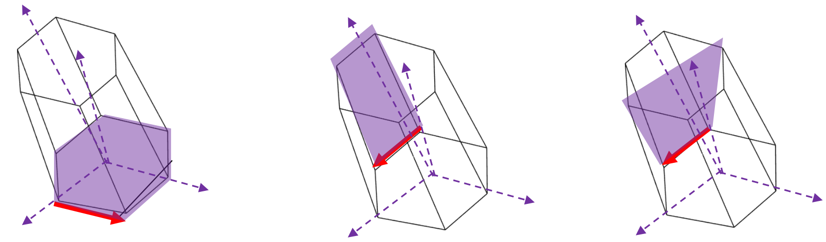

Basal slip system<a>

$(0001)<11\bar{2}0>$

Prismatic slip<a>

$\{10\bar{1}0\}<11\bar{2}0>$

Pyramidal slip<a>

$\{10\bar{1}1\}<11\bar{2}0>$

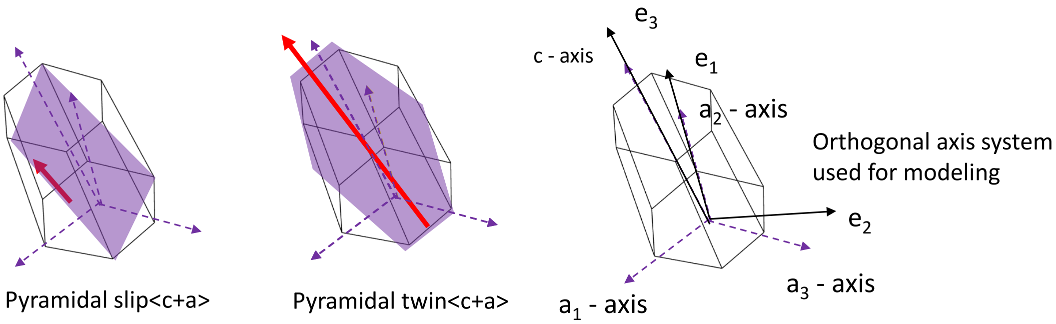

Pyramidal slip<c+a>

$\{11\bar{2}2\}<11\bar{2}3>$

Pyramidal twin<c+a>

$\{10\bar{1}2\}<\bar{1}011>$

Figure 1.1: Slip and twin systems of Magnesium alloys

Fig. 1.1 shows the slip systems of Magnesium alloys and the orthogonal axes (e_1, e_2, e_3) used in modeling. Magnesium is a HCP material with a c/a ratio of 1.624. The dominant mode of plastic deformation in magnesium alloys is due to basal slip, but other modes of deformation such as prismatic$< a >$ and pyramidal$< a >$ slip have also been observed at room temperature [28, 91].

The critical resolved shear stress (CRSS) for basal slip is significantly lower than the other slip systems and as a result, the grains tend to reorient themselves such that the c-axis aligns perpendicular to the rolling axis [117]. This strongly basal texture limits ductility by preventing easy activation of slip. When a specimen with a strongly basal texture is loaded in uniaxial tension along the rolling direction, the basal slip system is not favorably oriented in grains and therefore the non-basal systems with higher critical resolved shear stress would be activated, thus inhibiting its ductility.

Therefore, a weakly basal texture which can enable more basal slip would lead to improvements in ductility of the material [46].

The evolution of texture in polycrystals has been well studied in the past (e.g. for a review see [60]). Many of the relevant literature apply the Taylor-type micro-macro transition which assumes a purely kinematic constraint mainly that all grains are subjected to the same deformation. This assumption satisfies compatibility but fails to account for equilibrium across grain boundaries [96]. The effect of stereology and formation of misoriented regions within crystals due to non-uniform deformation are not taken into consideration. To model these heterogeneities, discretized grain structures have been modeled [20, 21, 27, 55, 72, 101, 61], where microstructural constituents are idealized grains with a fixed topology, or realistic polyhedral grains in two or three dimensions [70, 84]. In many of these cases, a velocity-based finite element formulation is used [20, 81, 72, 84, 98], or displacement-based finite element formulations are used, frequently implemented into commercial finite element codes [21]. In crystal plasticity finite element theory, the reorientation of crystals (texturing) is modeled by deforming an aggregate of grains. Deformation mechanisms such as dislocation slip and twinning are modeled using constitutive laws based on state variables such as dislocation densities or slip system resistances along various slip systems. Reorientation of grains and evolution of the threshold stress along each slip system due to various hardening mechanisms (self-hardening, latent hardening etc.) are modeled. The grain-level stresses are averaged to obtain the macroscopic response (stress-strain curve), and crystallographic texture is post-processed. The understanding of the relationship between the deformation process route and the macroscopic response which is, in turn, governed by the evolving microstructure is critical for designing materials with tailored properties for high performance applications in the aerospace industry [100, 102, 104, 65, 1, 2]. Such a microstructure–process–property relationship is provided by crystal plasticity finite element models.

In addition to crystallographic slip, magnesium alloys also exhibit twinning as a deformation mode. Chin and Mammel [34] were the first to incorporate twinning within the maximum work formulation of Bishop and Hill [24] . Thornburg and Piehler [111] improved the treatment of Chin and Mammel and provided a analysis of the vertices of the Single Crystal Yield Surface (SCYS) in terms of the relative values of the CRSS's. Van Houtte [115] was the first to propose a way of dealing with reorientation by twinning during the simulation of texture development and to apply the model for the prediction of rolling textures in f.c.c, brass, assuming $\{1\bar{1}1\}(110)$ slip and $\{111\}(11\bar{2})$ twinning. Tome et al. [112] proposed the Predominant Twin Reorientation (PTR) Scheme. The accumulated volume fraction represented by the twin-reoriented grains is made to match the accumulated twinned fraction associated with the twinning shears.

Elastoplastic self-consistent (EPSC) models, viscoplastic self-consistent (VPSC) models [7, 69, 83] and finite element crystal plasticity models [92, 93, 103, 105] are valuable tools for better understanding the CRSS and relative activation of the different slip systems during plastic deformation. If crystal plasticity models can precisely predict flow curves in magnesium alloys, the next step is to predict full-field strains accurately [46]. Full-field strains at the microstructural level can thus reveal information about the strain heterogeneities on the surface, and their relationships to the local microstructure, which are averaged in the macroscopic stress-strain data.

1.3 Digital Image Correlation Experiments

Optical deformation tracking methods, including digital image correlation, have been widely utilized to quantify the mechanical behavior of magnesium alloys at the macroscale and mesoscale. Digital Image Correlation (DIC) is a useful technique for characterizing macroscopic and microscopic surface strains. It tracks the deformation of a speckle pattern placed on a material surface during thermo-mechanical loading [86]. The technique is length scale independent, but a suitable speckle pattern must be applied to a surface at the desired field of view [46].

The details of the SEM-DIC experiments that were performed for the WE43 alloys are described in [46]. The primary material used for the experiments [46] was a hot rolled and annealed WE43 plate of thickness 31 mm. The plate was annealed at 477K for 48 hours [46]. This material is referred to as T5 temper. The samples were solution treated in an open-air furnace at 798K for 8 hours, followed by a water quench [46]. Subsequently, it is subjected to aging treatment in a silicone oil bath at 523K for a peak aging time of 16 hours followed by water quench [46]. This heat treated material is referred to as T6 temper.

One of the objectives of this work is to validate the crystal plasticity theory by comparing with tensile and compressive microscopic plastic strain response of magnesium alloy WE43 and relating this response to the underlying microstructure.

With this background, the thesis is organized as follows :

1. In Chapter 2, we describe the formulation of the rate independent crystal plasticity model, and incorporation of deformation twinning within the model is explained. The model is set in an incremental form to describe the computational procedure to solve the problem. It is supported by example problems for FCC and BCC polycrystals which help in benchmarking the code with the literature. The performance of the code is examined for an example problem. Furthermore, reading external microstructures are described in this chapter.

2. In Chapter 3, we describe the modeling of slip and twin systems in HCP WE-43 alloys. The methodology to construct Representative Volume Element (RVE) with a similar texture to the one observed in the experiments is described. This makes use of orientation distribution function (ODF) to represent the texture of the microstructure. Using stress-strain curves obtained from experiments and a texture matched

RVE obtained from [82], the parameters required for crystal plasticity simulations are identified. Relative activity of slip systems for different modes of deformation and the corresponding pole figures are examined.

3. In Chapter 4, Boundary Value Problems (BVP) are set up to compare the SEM-DIC experiments with the crystal plasticity finite element simulations. The methodology to compare the experiments with the simulations is explained and the problem is set-up for WE43-T6 temper. Comparisons are made between the SEM-DIC experiments and CPFE simulations for the displacement and strain fields and the effect of basal schmid factor, grain size , boundary conditions are studied.

4. In Chapter 5, the DIC results are compared against crystal plasticity finite element (CPFE) simulations for WE-43 T5 temper in order to test the CPFE model against DIC data, identify Schmid factor variations due to the effects of neighbor grains, and to differentiate the slip traces observed in the DIC data into various slip and twin systems.

5. In Chapter 6, we explore the effect of subsurface grains on the CPFE/DIC comparison and use a generalized inverse Voronoi problem approach to construct an approximate Voronoi representation of the 3D microstructure given the 2D surface image. Comparisons are made with surface DIC measurements for random samples of 3D microstructures as compared to columnar 2D microstructures.

6. We conclude in Chapter 7 of the thesis and propose some ideas for future work such as accommodating Hall-Petch effect, grain boundary sliding effects into the CPFE-DIC comparisons. For 3D reconstruction of microstructures, we discuss the extension of this theory to non-convex microstructures and modeling twinned regions within the grain. Code snippets are attached in the appendix.

CHAPTER II

PRISMS-Plasticity Crystal Plasticity finite element code: Formulation, Numerical Implementation and Examples

A parallel 3-D crystal plasticity finite element (CPFE) open-source code was developed based on the deal.II [17] finite element framework as part of PRISMS-Plasticity. The code demonstrates parallel performance and scaling on large-scale problems running on hundreds of processors. Rate-independent crystal plasticity was implemented by developing a non-linear algorithm which enables all the slip systems to lie on or inside the yield surface and a consistent tangent modulus ensures convergence for small loading increments. A twin activation mechanism is incorporated into the framework based on a quadrature point sensitive scheme. Furthermore, load-step adaptivity is included by bounding the L^2-norm of the plastic slip within the constitutive model.

In this chapter, the formulation of the rate independent crystal plasticity model and incorporation of deformation twinning into the model is described. It is followed by example problems for FCC and BCC polycrystals which help in benchmarking the code with the literature. The performance of the code is analyzed for an example problem. Furthermore, reading external microstructures are detailed in this chapter.

2.1 Crystal plasticity constitutive model

Classical single-crystal plasticity theory is used to model the deformation within each grain. The theory is based on the notion that plastic flow takes place through slip on prescribed slip systems. For a material with $\alpha = 1, \ldots, N$ slip systems defined by ortho-normal vector pairs $(\boldsymbol{m}_0^\alpha,\boldsymbol{n}_0^\alpha)$ denoting the slip direction and slip plane normal respectively at time $t = 0$, the constitutive equations relate the following basic fields (all quantities expressed in crystal lattice coordinate frame): the deformation gradient defined with respect to the initial undeformed crystal $\boldsymbol{F}$ which can be decomposed into elastic and plastic parts as $\boldsymbol{F} = \boldsymbol{F}^e\ \boldsymbol{F}^p$ (with $\det(\boldsymbol{F}^p) = 1$), the Cauchy stress $\boldsymbol{\sigma}$ and the slip resistances $s^\alpha > 0$. In the constitutive equations to be defined below, the Green elastic strain measure $\bar{\boldsymbol{E}}^e = \frac{1}{2}\left(\boldsymbol{F}^{eT}\boldsymbol{F}^e - \boldsymbol{I}\right)$ defined on the relaxed configuration (plastically deformed, unstressed configuration) is utilized. The conjugate stress measure is then defined as $\bar{\boldsymbol{T}} = \det(\boldsymbol{F}^e)(\boldsymbol{F}^e)^{-1}\boldsymbol{\sigma}(\boldsymbol{F}^e)^{-T}$ (refer to appendix A). Kinematics of single crystal slip is illustrated in Fig. 2.1.

The constitutive relation, for stress, is given by $\bar{\boldsymbol{T}} = \boldsymbol{\mathcal{L}}^e\left[\bar{\boldsymbol{E}}^e\right]$ where $\boldsymbol{\mathcal{L}}^e$ is the fourth-order anisotropic elasticity tensor. It is assumed that deformation takes place through dislocation glide and the evolution of the plastic velocity gradient is given by:

$$\boldsymbol{L}^p = \dot{\boldsymbol{F}}^p(\boldsymbol{F}^p)^{-1} = \sum_\alpha \dot{\gamma}^\alpha \boldsymbol{S}_0^\alpha \text{sign}(\tau^\alpha) \tag{2.1}$$

where $\boldsymbol{S}_0^\alpha = \boldsymbol{m}_0^\alpha \otimes \boldsymbol{n}_0^\alpha$ is the Schmid tensor and $\dot{\gamma}^\alpha$ is the plastic shearing rate on the α^{th} slip system.

The resolved stress on the α^{th} slip system is given by $\tau^\alpha = (\boldsymbol{C}^e\ \bar{\boldsymbol{T}}) \cdot \boldsymbol{S}_0^\alpha$. This follows from Anand [11] that the plastic power per unit volume in this configuration may be defined by $\dot{\omega} = (\boldsymbol{C}^e\ \bar{\boldsymbol{T}}) \cdot \boldsymbol{L_p}$ with $\boldsymbol{C}^e = \boldsymbol{F}^{eT}\boldsymbol{F}^e$ (refer to appendix A). The resolved shear stress is defined through the relation $\dot{\omega} = \sum_\alpha \tau^\alpha\dot{\gamma}^\alpha$.

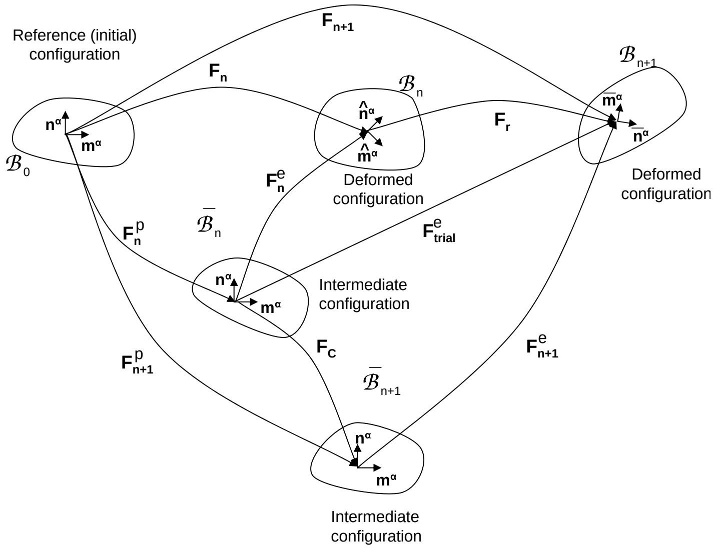

Figure 2.1: Schematic of the various material configurations, for a single crystal, used in the integration of the constitutive model. The slip systems ($\boldsymbol{m}^\alpha, \boldsymbol{n}^\alpha$ are known on the reference (initial) configuration. Also, $\hat{\boldsymbol{m}}^\alpha$, $\bar{\boldsymbol{m}}^\alpha$ are the slip directions (different from $\boldsymbol{m}^\alpha$ because of crystal re-orientation) in the deformed configurations $\mathcal{B}_n$ and $\mathcal{B}_{n+1}$, respectively.

A rate independent algorithm is employed to solve the single crystal problem [12]. The resolved shear stress τ^α is taken to attain a critical value s^α (the slip system resistance) on the systems where slip occurs. These active systems have a plastic shearing rate $\dot{\gamma}^\alpha > 0$, where $\dot{\gamma}^\alpha$ is assumed to be constant during the time step. There is no plastic shearing rate, i.e., $\dot{\gamma}^\alpha = 0$ on inactive slip systems where the resolved shear stress does not exceed s^α. The evolution of slip system resistance given by the following expression:

$$\dot{s}^\alpha(t) = \sum_\beta h^{\alpha\beta}(t)\dot{\gamma}^\beta(t), \quad s^\alpha(0) = \tau_0^\alpha \tag{2.2}$$

where

$$h^{\alpha\beta}(t) = \begin{cases} h_o^\beta \left(1 - \frac{s^\beta(t)}{s_s^\beta}\right)^a, & \text{if } \alpha = \beta, \quad \text{or for coplanar systems} \\ h_o^\beta q \left(1 - \frac{s^\beta(t)}{s_s^\beta}\right)^a, & \text{otherwise.} \end{cases}$$

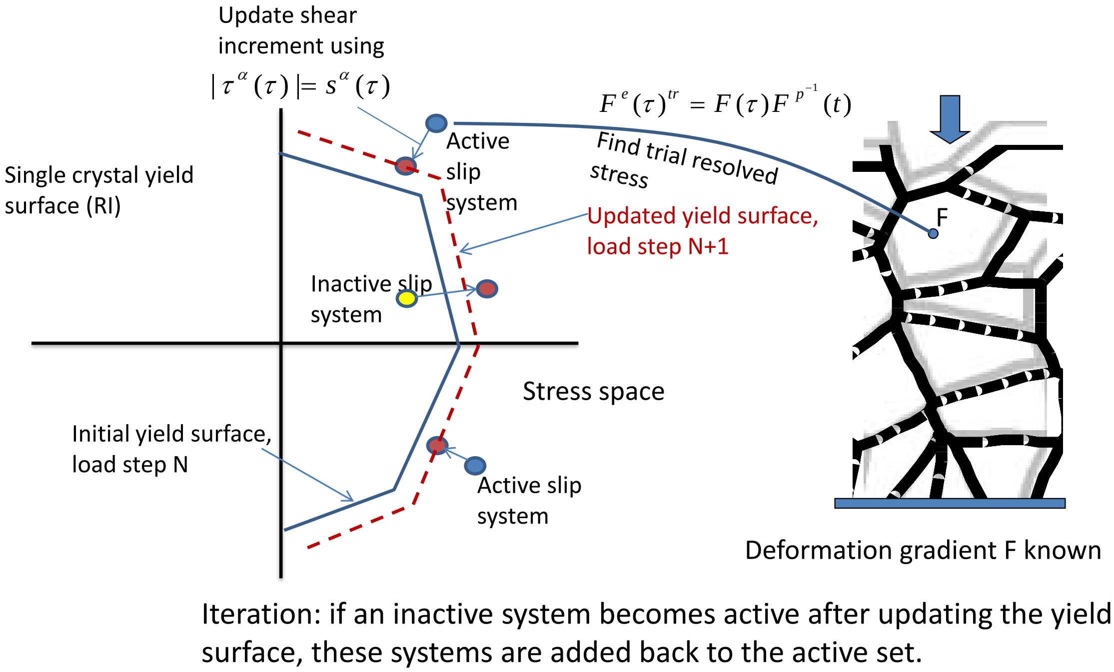

Figure 2.2: Schematic of the active slip systems and computation of the updated yield surface. The iterative algorithm ensures that that all the slip systems lie on or inside the yield surface.

with h_o^{β} indicating the self-hardening rate and the parameter q, with values in the range $1 < \mathrm{q} < 1.4$, representing a latent-hardening parameter. Subsequently, the plastic part of the deformation gradient is updated using Eq. (2.1), the elastic part computed from $\boldsymbol{F} = \boldsymbol{F}^{e}\ \boldsymbol{F}^{p}$. The conjugate stress measure, $\bar{\boldsymbol{T}}$ is then computed from $\bar{\boldsymbol{T}} = \boldsymbol{\mathcal{L}}^{e}\left[\bar{\boldsymbol{E}}^{e}\right]$ and converted to Cauchy stress and the Piola-Kirchhoff-I stress, $\boldsymbol{P} = (\det\boldsymbol{F})\boldsymbol{\sigma}\boldsymbol{F}^{-T}$ for further use. The slip resistances are also updated at the end of the time step using Eq. 2.2 .

The rate independent model is used to find the PKI stress and tangent modulus for getting the finite element nodal displacements. The deformation gradient can be decomposed into elastic and plastic parts as follows,

$$\boldsymbol{F} = \boldsymbol{F}^e \ \boldsymbol{F}^p \tag{2.3}$$

where $\boldsymbol{F}^e$ is the elastic deformation gradient, while $\boldsymbol{F}^p$ is plastic deformation gradient with $\det(\boldsymbol{F}^p) = 1$. The plastic flow rule is given by the sum of strain rate over all slip systems,

$$\dot{\boldsymbol{F}}^p(\boldsymbol{F}^p)^{-1} \ = \ \sum_\alpha \dot{\gamma}^\alpha \boldsymbol{S}_0^\alpha \mathrm{sign}(\tau^\alpha) \tag{2.4}$$

where $\boldsymbol{S}_0^\alpha = \boldsymbol{m}^\alpha \otimes \boldsymbol{n}^\alpha$ is the Schmid tensor and $\dot{\gamma}^\alpha$ is the plastic shearing rate on the α^{th} slip system. The solution of $\boldsymbol{F}^p$ is computed by assuming a constant shearing rate $\dot{\gamma}^\alpha$ for the time-step:

$$\boldsymbol{F}^p_{n+1} = \exp(\sum_\alpha \Delta\gamma^\alpha \boldsymbol{S}_0^\alpha \mathrm{sign}(\tau^\alpha))\boldsymbol{F}^p_n \tag{2.5}$$

The use of matrix exponential function ensures that the plastic deformation is isochoric. This can be seen from the fact that $\mathrm{tr}(\boldsymbol{S}_0^\alpha) = \mathrm{tr}(\boldsymbol{m}_0^\alpha \otimes \boldsymbol{n}_0^\alpha) = 0$. Therefore, $\det\left[\exp(\sum_\alpha \Delta\gamma^\alpha \boldsymbol{S}_0^\alpha \mathrm{sign}(\tau^\alpha))\right] = 1$.

The term $\dot{\gamma}$ from Eq. 2.1 changes to $\Delta\gamma$ here, because it is now the increment in infinitesimal time Δt. In Eq. 2.3, $\boldsymbol{F}^e$ can be obtained as follows:

$$\boldsymbol{F}^e = \boldsymbol{F}^e_{tr} \exp(-\sum_\alpha \Delta\gamma^\alpha \boldsymbol{S}_0^\alpha \mathrm{sign}(\tau^\alpha)) \tag{2.6}$$

where $\boldsymbol{F}^e_{tr}$ is the trial elastic deformation gradient and is given by $\boldsymbol{F}_{n+1}(\boldsymbol{F}^p_n)^{-1}$. Lagrange strain in relaxed configuration can be written as:

$$\boldsymbol{E}^e \ = \ \frac{1}{2}((\boldsymbol{F}^e)^T \boldsymbol{F}^e - \boldsymbol{I}) \tag{2.7}$$

Let t denote the current time, Δt an infinitesimal time increment, and $\tau = t + \Delta t$. Then, given $\boldsymbol{F}(t), \boldsymbol{F}(\tau)$, $\boldsymbol{m}_0^\alpha, \boldsymbol{n}_0^\alpha, \boldsymbol{\sigma}(t), \boldsymbol{F}^p(t)$ and $s^\alpha(t)$, $\boldsymbol{F}^p(\tau), s^\alpha(\tau), \sigma(\tau)$ need to be determined. First, deformation gradient and Lagrangian strain are shown as

$$\boldsymbol{F}_{tr}^e(\tau) = \boldsymbol{F}(\tau)\ \boldsymbol{F}^p(t)^{-1} \tag{2.8}$$

$$\boldsymbol{E}_{tr}^e(\tau) = \frac{1}{2}((\boldsymbol{F}_{tr}^e(\tau))^T \boldsymbol{F}_{tr}^e(\tau) - \boldsymbol{I}) \tag{2.9}$$

In order to find the resolved shear stress, the conjugate stress measure is then defined by

$$\bar{\boldsymbol{T}} \ = \ \det(\boldsymbol{F}^e)(\boldsymbol{F}^e)^{-1}\boldsymbol{\sigma}(\boldsymbol{F}^e)^{-T} \tag{2.10}$$

while $\bar{\boldsymbol{T}}(\tau)$ is expressed as

$$\bar{\boldsymbol{T}}(\tau) \ = \ \boldsymbol{\mathcal{L}}^e\left[\bar{\boldsymbol{E}}^e(\tau)\right] \tag{2.11}$$

where $\bar{\boldsymbol{T}}_{tr}(\tau)$ is calculated in the same manner as $\boldsymbol{\mathcal{L}}^e\left[\bar{\boldsymbol{E}}^e{}_{tr}(\tau)\right]$, where $\boldsymbol{\mathcal{L}}^e$ is the fourth-order anisotropic elasticity tensor. The resolved shear stress is given by

$$\tau^\alpha = (\boldsymbol{C}^e(\tau)\bar{\boldsymbol{T}}(\tau)) \cdot \boldsymbol{S}_0^\alpha \tag{2.12}$$

while the trial resolved shear stress is defined in the same way as $\tau_{tr}^\alpha(\tau) = (\boldsymbol{C}_{tr}^e(\tau)\bar{\boldsymbol{T}}_{tr}(\tau)) \cdot \boldsymbol{S}_0^\alpha$.

In crystal plasticity theory, the hardening law for the slip resistance s^α at time τ is given as:

$$s^\alpha(\tau) = s^\alpha(t) + \sum_\beta h^{\alpha\beta}(t)\Delta\gamma^\beta \tag{2.13}$$

where $h^{\alpha\beta}$ describes the rate of increase of the deformation resistance on slip system α due to shearing on slip system β. Now we can determine $\Delta\gamma$ using the equality

$|\tau^{\alpha}| = s^{\alpha}$, with $\alpha, \beta \in \mathcal{A}$, the active set of slip systems:

$$\sum_{\beta \in \mathcal{A}} A^{\alpha\beta} \Delta\gamma^{\beta} = b^{\alpha} \tag{2.14}$$

where,

$$\begin{aligned}
&A^{\alpha\beta} = h^{\alpha\beta}(t) + \mathrm{sign}(\tau_{tr}^{\alpha}(\tau))\mathrm{sign}(\tau_{tr}^{\beta}(\tau))(\boldsymbol{C}_{tr}^{e}(\tau)\boldsymbol{\mathcal{L}}^{e}\left[\boldsymbol{B}^{\beta}\right] + 2\boldsymbol{B}^{\beta}\bar{\boldsymbol{T}}_{tr}(\tau)) \cdot \boldsymbol{S}_0^{\alpha},\\
&b^{\alpha} = |\tau_{tr}^{\alpha}(\tau)| - s^{\alpha}(t) > 0, \qquad (2.15)\\
&\Delta\gamma^{\beta} > 0
\end{aligned}$$

$$\boldsymbol{B^{\beta}} = \tfrac{1}{2}((\boldsymbol{S}_0^{\beta})^T(\boldsymbol{F}_{tr}^{e})^T\boldsymbol{F}_{tr}^{e} + (\boldsymbol{F}_{tr}^{e})^T\boldsymbol{F}_{tr}^{e}\boldsymbol{S}_0^{\beta})$$

Eq. 2.14 is a system of linear equations. However, the elements of the set $\mathcal{A}$ are not known. They are determined in an iterative fashion. It is initially assumed that all the potentially active systems are active

$$\sum_{\beta \in \mathcal{PA}} A^{\alpha\beta} \Delta\gamma^{\beta} = b^{\alpha} \tag{2.16}$$

and this linear system is solved. We look for elements with $\Delta\gamma^{\beta} > 0$, the systems with $\Delta\gamma^{\beta} \leqslant 0$ are considered inactive and are removed from the list of active slip systems. The reduced system is solved and the procedure is repeated until all $\Delta\gamma^{\beta} > 0$. Only values of $\Delta\gamma$ larger than 0 are kept.

Then, $\boldsymbol{F}^{p}(\tau)$ can be updated by Eq. 2.5, $\boldsymbol{F}^{e}(\tau)$ updates through Eq. 2.3 or Eq. 2.6. In order to update $\boldsymbol{\sigma}(\tau)$, $\bar{\boldsymbol{T}}(\tau)$ needs to be updated first, Eq. 2.11. Then $\boldsymbol{\sigma}(\tau)$ can be found by $\boldsymbol{\sigma}(\tau) = \boldsymbol{F}^{e}(\tau)(\det(\boldsymbol{F}^{e}(\tau)))^{-1}\bar{\boldsymbol{T}}(\tau)\boldsymbol{F}^{e}(\tau)^{T}$ from Eq .2.10, and $s^{\alpha}(\tau)_i$ can be specified by Eq.2.13. Once $\boldsymbol{F}^{p}(\tau)$ and $s^{\alpha}(\tau)_i$ are updated, we use Eqns. 2.8 -2.12 to update the trial resolved shear stresses $\tau_{tr}^{\alpha}(\tau)_i$. Now, these potentially active systems may not lie on the new yield surface, so we correct for the non-linear model as follows

$$\sum_{\beta\in\mathcal{A}} A^{\alpha\beta}\delta(\Delta\gamma^{\beta}) = b_i^{\alpha} \tag{2.17}$$

Eq. (2.17) is solved repeatedly only for the initial active slip systems with $b_i^{\alpha} = |\tau^{\alpha}(\tau)|_i - s^{\alpha}(\tau)_i$ and $A^{\alpha\beta} = h^{\alpha\beta}(t) + \mathrm{sign}(\tau^{\alpha}_{tr}(\tau))\mathrm{sign}(\tau^{\beta}_{tr}(\tau))(\boldsymbol{C}^{e}_{tr}(\tau)\boldsymbol{\mathcal{L}}^{e}\left[\boldsymbol{B}^{\beta}\right] + \boldsymbol{B}^{\beta}\bar{\boldsymbol{T}}_{tr}(\tau))\cdot \boldsymbol{S}_0^{\alpha}$ and $\Delta\gamma^{\beta}$ is updated and used to compute until $\boldsymbol{F}^{p}(\tau)$, $\tau^{\alpha}_{tr}(\tau)_i$ and $s^{\alpha}(\tau)_i$ until $b_i^{\alpha} < \epsilon$ is reached. Here ϵ is the specified stress tolerance and i is the iterative step. If ϵ is set high, it is equivalent to doing one iteration, which is similar to [12].

Once $\boldsymbol{F}^{p}(\tau)$ and $s^{\alpha}(\tau)$ are updated, we use Eqns. (2.8 -2.12) to update the trial resolved shear stresses $\tau^{\alpha}_{tr}(\tau)$ for all the other slip systems. If for some of the slip systems $|\tau^{\alpha}_{tr}(\tau)| > s^{\alpha}(\tau) + \epsilon$, then the procedure is repeated from 2.14 to ensure that all the slip systems lie on or inside the new yield surface.

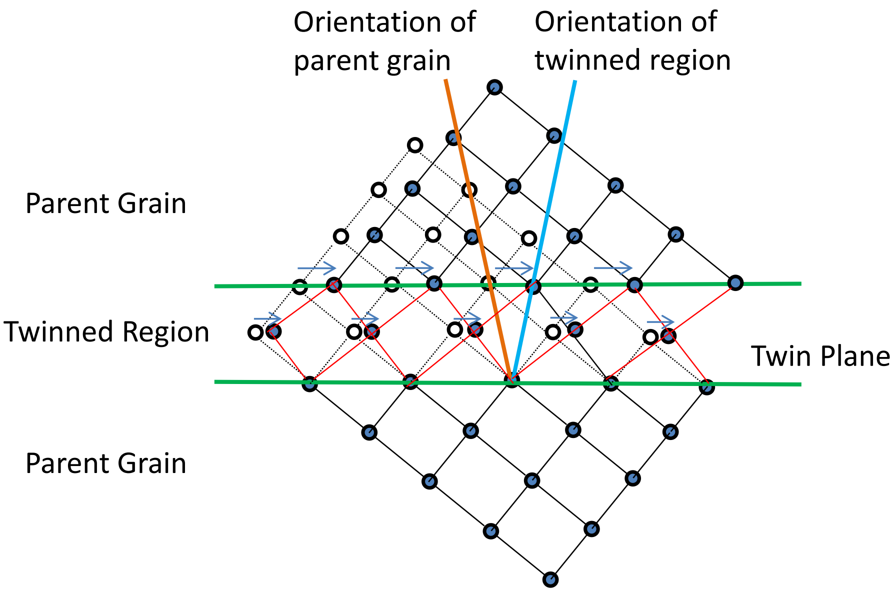

Figure 2.3: Crystallography of twinned region

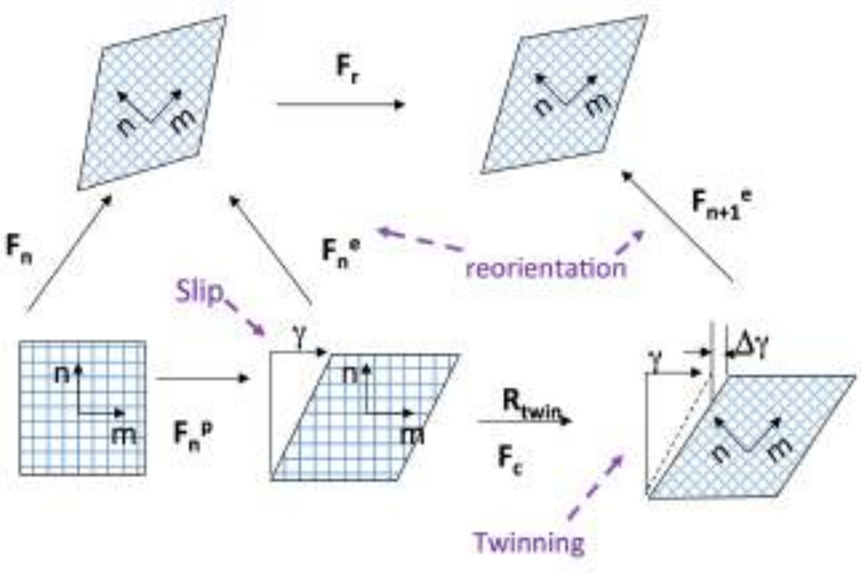

Figure 2.4: Kinematics of slip and twinning

Modeling Deformation Twinning in WE-43 Magnesium Alloys

The crystallography of twins is shown in Fig. 2.3 indicating the parent grain, twinned region and the orientation of the corresponding regions. The kinematics of slip and twinning is shown in Fig. 2.4. Twin systems are initially considered as slip systems and are sheared until they are reoriented. Our formulation for twinning closely follows the approach adopted by Staroselsky et al. [91] . The differences in the approach are as follows :

1) We adopt the Predominant Twin Reorientation scheme (PTR) [112] instead of the scheme proposed by Van Houtte [115] . As more elements are reoriented, the PTR scheme inhibits further reorientation by twinning until accumulated fraction catches up as the deformation proceeds.

2) The individual quadrature points are reoriented as compared to reorienting the entire grain. We keep track of the orientations of all quadrature points in the FE simulation and reorient the individual points which satisfy the PTR scheme [112].

The approach in [91] considers each grain as represented by a single element whereas in the current approach each grain is represented by multiple elements.

3) We use Implicit FEM which enforces static equilibrium at each time step compared to Explicit FEM used by Staroselsky et al.

Reorientation Scheme

Fraction of the grain associated with each twinning system is given by

$$g^{n,t_i} = \Sigma_{steps} \Delta g^{n,t_i} \tag{2.18}$$

where $g^{n,t_i} = \frac{\Delta \gamma^{n,t_i}}{S}$, n is the n^{th} quadrature point, steps is the number of time-steps, t_i is the i^{th} twinning system and S is the characteristic twin shear strain, which is calculated to be 0.129 for Magnesium [36].

Threshold fraction for twinning is calculated locally at each element making the method locally-sensitive

$$F_T = 0.25(1 + \frac{N}{\Sigma_i g^{n,t_i}}) \tag{2.19}$$

where N is total reoriented volume fraction of the grain. If $g^{n,t_i} > F_T$, the quadrature point is reoriented due to twinning. For the purpose of CPFE-DIC comparisons in this study, we assume a simplified model of F_T=0.25.

Lattice Reorientation Due To Twinning

A schematic diagram of reorientation due to twinning is shown in Fig. 2.5. The procedure to find the new orientation for the reoriented grain,

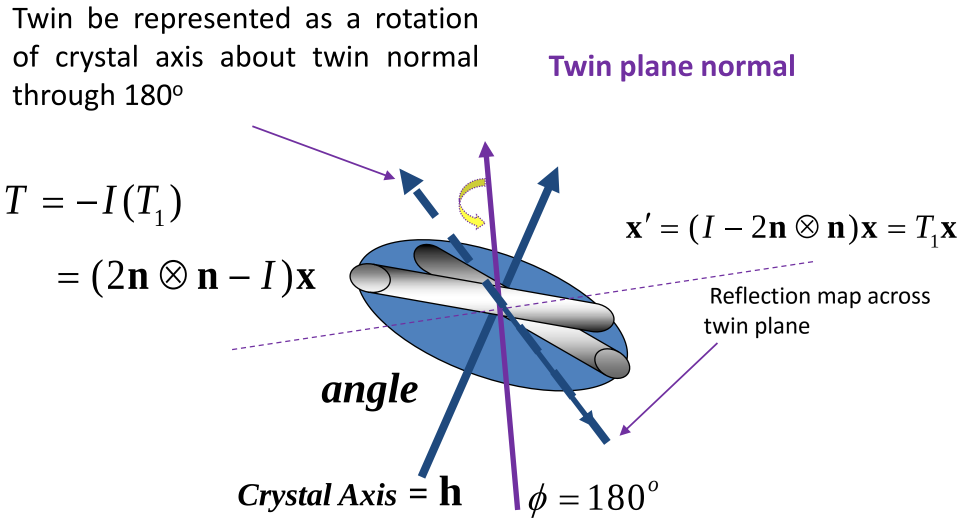

Figure 2.5: Reorientation due to twinning

1) Find the rotation matrix for reference frame to crystal frame, $\boldsymbol{R_1}$

2) Find the rotation matrix for rotating the crystal frame about the twin plane by 180^o , $\boldsymbol{R_2}$

3)New rotation matrix $\boldsymbol{Q} = \boldsymbol{R_1} \cdot \boldsymbol{R_2}$.

4)Project $\boldsymbol{Q}$ to the fundamental region (QF) based on crystal symmetries.

5) Convert the rotation matrix QF to Rodrigues vector.

The plastic component of the deformation gradient is updated in the crystal frame to accommodate the reorientation due to twinning. The rotation matrix for rotating the crystal frame about the twin plane $\boldsymbol{R_2}$ is given by

$$\boldsymbol{R_2} = 2\boldsymbol{n_i} \otimes \boldsymbol{n_i} - \boldsymbol{I} \tag{2.20}$$

2.2 Deformation Solver

The kinematic problem can be expressed in Lagrangian framework as

$$\nabla_0 \cdot \boldsymbol{P} + \boldsymbol{f} = \boldsymbol{0} \tag{2.21}$$

where ∇_0 is the divergence in the initial reference configuration, $\boldsymbol{P}$ is the polycrystal Piola-Kirchhoff-I stress and $\boldsymbol{f}$ is the reference body force.

$$\boldsymbol{P} = \det(\boldsymbol{F})\boldsymbol{\sigma}\boldsymbol{F}^{-T} \tag{2.22}$$

Principle of virtual work states that $\mathcal{B}_0$ is in equilibrium if and only if the Piola-Kirchoff stress field, $\boldsymbol{P}$, satisfies the virtual work functional for any kinematically admissible test function $\tilde{\boldsymbol{u}}$,

$$\mathcal{G}(\boldsymbol{u}, \tilde{\boldsymbol{u}}) \equiv \int\limits_{\mathcal{B}_0} \boldsymbol{P} \cdot \nabla_0 \tilde{\boldsymbol{u}} dV - \int\limits_{\partial\mathcal{B}_0} \boldsymbol{\lambda} \cdot \tilde{\boldsymbol{u}} dA - \int\limits_{\mathcal{B}_0} \boldsymbol{f} \cdot \tilde{\boldsymbol{u}} dV = 0 \qquad \forall \tilde{\boldsymbol{u}} \in \mathcal{V} \tag{2.23}$$

where $\boldsymbol{u}$ is the displacement field, $\mathcal{V}$ is a finite dimensional vector space of all admissible shape functions in the material domain, where $\boldsymbol{f}$ and $\boldsymbol{\lambda}$ denote, respectively, the reference body force and surface traction field.

The dependence of $\mathcal{G}$ on the unknown function $\boldsymbol{u}$ follows from the constitutive dependence of the stress tensor on the strain tensor which, in turn depends on the field $\boldsymbol{u}$. In the above, $\boldsymbol{P}$ is a function of the displacement field due to its constitutive dependence on the deformation gradient $\boldsymbol{F} = \boldsymbol{I} + \nabla_0 \boldsymbol{u}$.

Newton-Raphson iterative scheme with a line search procedure is employed. The Gâteaux derivative of $\mathcal{G}$ at $\boldsymbol{u}_n$ in the direction of $\Delta \boldsymbol{u}$ is given by

$$\frac{\partial \mathcal{G}(\boldsymbol{u}_n, \tilde{\boldsymbol{u}})}{\partial \boldsymbol{u}_n}\Delta \boldsymbol{u} = \int\limits_{\mathcal{B}_0} \boldsymbol{A}\frac{\partial \boldsymbol{F}}{\partial \boldsymbol{u}_n} \cdot \nabla_0 \tilde{\boldsymbol{u}} dV \Delta \boldsymbol{u} \tag{2.24}$$

where

$$\boldsymbol{A} \equiv \left.\frac{\partial \boldsymbol{P}}{\partial \boldsymbol{F}}\right|_{\boldsymbol{F}_n} \tag{2.25}$$

is generally termed the material tangent modulus.

The Piola-Kirchhoff-I stress, shown as $\boldsymbol{P}$ can be expanded as

$$\begin{aligned}
\boldsymbol{P} &= \det(\boldsymbol{F})\boldsymbol{\sigma}\boldsymbol{F}^{-T} \\
&= \det(\boldsymbol{F})((det(\boldsymbol{F}^e))^{-1}\boldsymbol{F}^e\bar{\boldsymbol{T}}(\boldsymbol{F}^e)^T)\boldsymbol{F}^{-T} \\
&= \boldsymbol{F}^e\bar{\boldsymbol{T}}(\boldsymbol{F}^e)^T\boldsymbol{F}^{-T} \quad (\quad \det(\boldsymbol{F}) = \det(\boldsymbol{F}^e).)
\end{aligned} \tag{2.26}$$

The variation of PKI stress at time τ is given by

$$\begin{aligned}
\delta\boldsymbol{P} &= \delta(\boldsymbol{F}^e\bar{\boldsymbol{T}}(\boldsymbol{F}^e)^T\boldsymbol{F}^{-T}) \\
&= \delta(\boldsymbol{F}^e)\bar{\boldsymbol{T}}(\boldsymbol{F}^e)^T\boldsymbol{F}^{-T} + \boldsymbol{F}^e\delta(\bar{\boldsymbol{T}})(\boldsymbol{F}^e)^T\boldsymbol{F}^{-T} + \boldsymbol{F}^e\bar{\boldsymbol{T}}\delta((\boldsymbol{F}^e)^T)\boldsymbol{F}^{-T} \\
&\quad + \boldsymbol{F}^e\bar{\boldsymbol{T}}(\boldsymbol{F}^e)^T\delta(\boldsymbol{F}^{-T}) \\
&= \delta(\boldsymbol{F}^e)\bar{\boldsymbol{T}}(\boldsymbol{F}^e)^T\boldsymbol{F}^{-T} + \boldsymbol{F}^e\delta(\bar{\boldsymbol{T}})(\boldsymbol{F}^e)^T\boldsymbol{F}^{-T} + \boldsymbol{F}^e\bar{\boldsymbol{T}}(\delta\boldsymbol{F}^e)^T\boldsymbol{F}^{-T} \\
&\quad + \boldsymbol{F}^e\bar{\boldsymbol{T}}(\boldsymbol{F}^e)^T\delta(\boldsymbol{F}^{-1})^T \\
&= \delta(\boldsymbol{F}^e)\bar{\boldsymbol{T}}(\boldsymbol{F}^e)^T\boldsymbol{F}^{-T} + \boldsymbol{F}^e\delta\bar{\boldsymbol{T}}(\boldsymbol{F}^e)^T\boldsymbol{F}^{-T} + \boldsymbol{F}^e\bar{\boldsymbol{T}}(\delta\boldsymbol{F}^e)^T\boldsymbol{F}^{-T} \\
&\quad - \boldsymbol{F}^e\bar{\boldsymbol{T}}(\boldsymbol{F}^e)^T(\boldsymbol{F}^{-1})^T\delta(\boldsymbol{F})^T(\boldsymbol{F}^{-1})^T
\end{aligned} \tag{2.27}$$

where $\delta\boldsymbol{F}^e$ is obtained as:

$$\begin{aligned}
\delta(\boldsymbol{F}^e) &= \delta\boldsymbol{F}(\boldsymbol{F}^p)^{-1} + \boldsymbol{F}\delta((\boldsymbol{F}^p)^{-1}) \\
&= \delta\boldsymbol{F}(\boldsymbol{F}^p)^{-1} - \boldsymbol{F}(\boldsymbol{F}^p)^{-1}\delta\boldsymbol{F}^p(\boldsymbol{F}^p)^{-1}
\end{aligned} \tag{2.28}$$

Then the computation of $\delta\bar{\boldsymbol{T}}$ can be obtained as from Eq. 2.11,

$$\delta\bar{\boldsymbol{T}} \;=\; \boldsymbol{\mathcal{L}}^e\left[\delta\bar{\boldsymbol{E}}^e\right] \tag{2.29}$$

while

$$\delta\bar{\boldsymbol{E}}^e \;=\; \frac{1}{2}((\delta\boldsymbol{F}^e)^T\boldsymbol{F}^e + (\boldsymbol{F}^e)^T\delta(\boldsymbol{F}^e)) \tag{2.30}$$

The variation of plastic deformation gradient, $\delta(\boldsymbol{F}^p)$ is computed in an iterative manner as follows

$\delta\boldsymbol{F}^e_{tr}$ is obtained as:

$$\begin{aligned}\delta(\boldsymbol{F}^e_{tr_i}) &= \delta\boldsymbol{F}(\boldsymbol{F}^p_{i-1})^{-1} + \boldsymbol{F}\delta((\boldsymbol{F}^p_{i-1})^{-1})\\ &= \delta\boldsymbol{F}(\boldsymbol{F}^p_{i-1})^{-1} - \boldsymbol{F}(\boldsymbol{F}^p_{i-1})^{-1}\delta(\boldsymbol{F}^p_{i-1})(\boldsymbol{F}^p_{i-1})^{-1}\end{aligned} \tag{2.31}$$

where $\boldsymbol{F}^p_i$ is the plastic deformation gradient in the i^{th} active set search completed to include the slip systems lying outside the yield surface. Before the beginning of active set search, $\boldsymbol{F}^p_0 = \boldsymbol{F}^p_n$ and $\delta\boldsymbol{F}^p_0 = \boldsymbol{0}$, where $\boldsymbol{F}^p_n$ is the plastic deformation gradient from the previous time-step.

$$\delta\bar{\boldsymbol{E}}^e{}_{tr_i} = \frac{1}{2}((\delta\boldsymbol{F}^{\boldsymbol{e}}{}_{tr_i})^T\boldsymbol{F}^e + (\boldsymbol{F}^e)^T\delta(\boldsymbol{F}^e_{tr_i})) \tag{2.32}$$

$$\delta\bar{\boldsymbol{T}}_{tr_i} \;=\; \boldsymbol{\mathcal{L}}^e\left[\delta\bar{\boldsymbol{E}}^e{}_{tr_i}\right] \tag{2.33}$$

$\delta(\Delta\gamma^\beta)$ in this equation is evaluated as following:

$$\begin{aligned}\delta b^\alpha_i &= \operatorname{sign}(\tau^\alpha_{tr_i})\delta(\boldsymbol{C}^e_{tr_i}\bar{\boldsymbol{T}}_{tr_i})\cdot\boldsymbol{S}^\alpha_0 - \delta(s^\alpha_{i-1})\\ &= \operatorname{sign}(\tau^\alpha_{tr_i})(\delta(\boldsymbol{C}^e_{tr_i})\bar{\boldsymbol{T}}_{tr_i} + \boldsymbol{C}^e_{tr_i}\delta(\bar{\boldsymbol{T}}_{tr_i}))\cdot\boldsymbol{S}^\alpha_0 - \delta(s^\alpha_{i-1})\\ &= \operatorname{sign}(\tau^\alpha_{tr_i})(2\delta(\bar{\boldsymbol{E}}^e{}_{tr_i})\bar{\boldsymbol{T}}_{tr_i} + \boldsymbol{C}^e_{tr_i}\delta(\bar{\boldsymbol{T}}_{tr_i}))\cdot\boldsymbol{S}^\alpha_0 - \delta(s^\alpha_{i-1})\end{aligned} \tag{2.34}$$

The variation of slip system resistance s^α is computed as follows

$$\begin{aligned}
\delta(s_i^\alpha) &= \delta(s_{i-1}^\alpha) + \sum_\beta \delta h_i^{\alpha\beta}\Delta\gamma^\beta + \sum_\beta h_i^{\alpha\beta}\delta(\Delta\gamma^\beta) \\
&= \delta(s_{i-1}^\alpha) + \sum_\beta h_i^{\alpha\beta}\delta\Delta\gamma^\beta \\
&\quad + \sum_\beta h_o^\beta(q+(1-q)\delta^{\alpha\beta})\left(1-\frac{s_i^\beta}{s_s^\beta}\right)^{(a-1)}\left(\frac{-1}{s_s^\beta}\right)\delta(s_{i-1}^\beta)\Delta\gamma^\beta \qquad (2.35)
\end{aligned}$$

The variation of slip shear increment $\delta(\Delta\gamma_i^\beta)$ is therefore

$$\begin{aligned}
\delta(\Delta\gamma_i^\beta) &= (A_i^{\alpha\beta})^{-1}(\delta b_i^\alpha - \delta A_i^{\alpha\beta}\Delta\gamma_i^\beta) \qquad (2.36)\\
\delta A_i^{\alpha\beta} &= \delta h_i^{\alpha\beta} + \mathrm{sign}(\tau_{tr}^\alpha(\tau))\mathrm{sign}(\tau_{tr}^\beta(\tau))(\delta\boldsymbol{C}_{tr_i}^e(\tau)\boldsymbol{\mathcal{L}}^e\left[\boldsymbol{B}_i^\beta\right] \\
&\quad + \boldsymbol{C}_{tr_i}^e(\tau)\boldsymbol{\mathcal{L}}^e\left[\delta\boldsymbol{B}_i^\beta\right] + 2\delta\boldsymbol{B}_i^\beta\bar{\boldsymbol{T}}_{tr_i}(\tau) + 2\boldsymbol{B}_i^\beta\delta\bar{\boldsymbol{T}}_{tr_i}(\tau))\cdot\boldsymbol{S}_0^\alpha \qquad (2.37)
\end{aligned}$$

while, $\delta\boldsymbol{B}_{\boldsymbol{i}}^{\boldsymbol{\beta}} = 0.5((\boldsymbol{S}_0^\beta)^T\delta\bar{\boldsymbol{E}}_{tr_i}^e + \delta\bar{\boldsymbol{E}}_{tr_i}^e\boldsymbol{S}_0^\beta)$ and $\delta h_i^{\alpha\beta} = h_o^\beta(q+(1-q)\delta^{\alpha\beta})\left(1-\frac{s_i^\beta}{s_s^\beta}\right)^{(a-1)}\left(\frac{-1}{s_s^\beta}\right)\delta(s_{i-1}^\beta)$

$\boldsymbol{F}^p$ is updated as follows :

$$\delta(\boldsymbol{F}_i^p) = \delta(\exp(\textstyle\sum_\alpha \Delta\gamma_i{}^{\boldsymbol{\alpha}}\boldsymbol{S}_0^\alpha\mathrm{sign}(\tau^\alpha)))(\boldsymbol{F}_{i-1}^p) + \exp(\textstyle\sum_\alpha \Delta\gamma_i{}^{\boldsymbol{\alpha}}\boldsymbol{S}_0^\alpha\mathrm{sign}(\tau^\alpha))\delta(\boldsymbol{F}_{i-1}^p) \qquad (2.38)$$

The solver was implemented using deal.ii library [17] which is based on a Finite Element Method (FEM) framework and MPI parallelization was used for speed–up. A scaling study was performed on FLUX cluster at the University of Michigan in 2.5 GHz Intel Xeon E5-2680v3 processors with 3.8 GB/core. The solution to an FEM problem consists of assembly and solve, where assembly process runs the constitutive

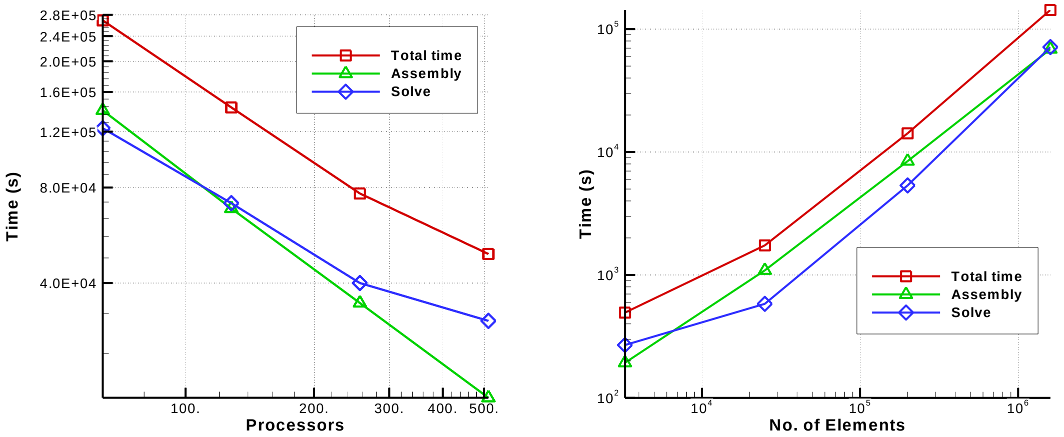

a)

b)

Figure 2.6: Scaling study for CPFE simulation of BCC Titanium microstructure a) strong scaling b) weak scaling

model and computes the tangent modulus and the solve process proceeds to solve the assembled system to compute the displacements across the nodes. A scaling study is shown in Fig. 2.6. Linear scaling is observed for the assembly and the solve has almost linear scaling with number of processors. The largest problem done was for a real 92 grain BCC microstructure [81] and solved for 1.6 million elements as can be seen in Fig. 2.6 b).

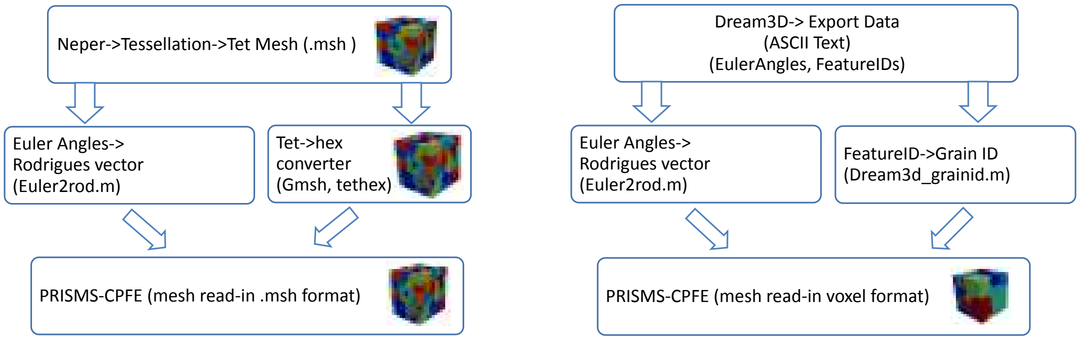

a)

b)

Figure 2.7: Flow-chart of methodology to read external microstructures from a) Neper b) DREAM.3D

2.3 Reading external microstructure

Neper is a open source software package for polycrystal generation and meshing [82]. Neper generates polycrystals by various types of voronoi tessellation such as centroidal and laguerre tessellations. Neper generates tessellation and grain-boundary conforming tetrahedral meshes. The input mesh format for the PRISMS-Plasticity code are hexahedral meshes. Therefore a procedure to convert tetrahedral meshes to hexahedral meshes is outlined in Fig. 2.7 a).

DREAM.3D is another open source, cross-platform and modular software package that can be used to reconstruct 3D microstructures or synthetically generate microstructures [50]. DREAM.3D outputs microstructures in the form of voxelated meshes or grain-boundary conforming surface meshes. The voxelated form of the microstructure can be input into the PRISMS-crystal plasticity code using the procedure described in Fig. 2.7 b).

2.4 Example

We evaluate the present formulation of the rate independent model by comparing the stress-strain response of the FCC and BCC polcrystals against the predictions of the rate independent model of [12] and rate dependent model of [81] respectively .

2.4.1 FCC polycrystal

For comparison, the values for the slip hardening parameters and initial value of the slip deformation resistance for single crystal copper are considered and are taken from [12] , also available in Appendix B.

$$h_0 = 180MPa \quad s_s = 148MPa \quad a = 2.25 \quad s_0 = 16MPa \tag{2.39}$$

In [12], a polycrystal with 343 elements, where each element is represented by

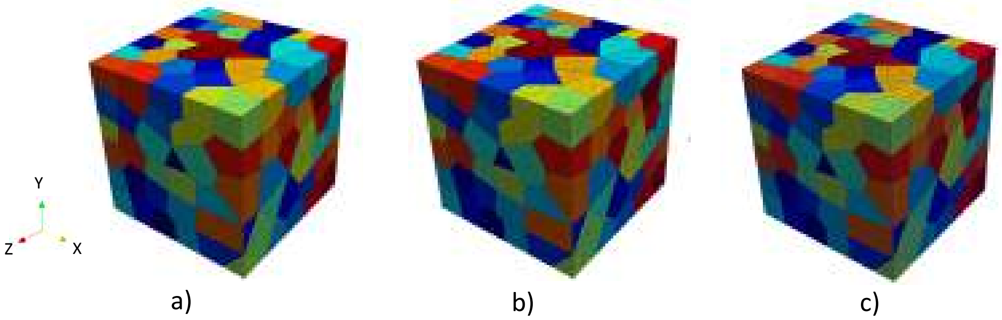

Figure 2.8: Virtual microstructures generated with Neper. (a) A 200 grain microstructure with a tetrahedral mesh comprising of 6750 elements. (b) A hexahedral mesh of 27000 elements generated with Gmsh tool. (c) A refined hexahedral mesh with 78000 elements.

a random orientation was considered to perform the simple compression simulation. In this study, we use a 200 grain polycrystal generated from Neper using Voronoi tessellation [82] as shown in Fig. 2.8 (a) comprising of 6750 elements. The procedure described in Fig. 2.7 a) is followed to obtained hexahedral elements as shown in Fig. 2.8 (b) and (c). Also, a regular mesh with 32*32*32 elements is used to the model the same polycrystal. The stress strain curves predicted by the non-conforming mesh is compared with the corresponding stress-stress curves from [12] as shown in Fig. 2.9 a). It shows that the PRISMS-Plasticity model slightly underpredicts the stress-strain curve as compared to [12]. The effect of conforming mesh on stress-strain curves is shown in Fig. 2.9 b). Non-conforming mesh of 32000 elements converges with lesser number of elements as compared to a conforming mesh of 27000 elements and has a similar stress-strain curve as compared to a conforming mesh of 78000 elements.

2.4.2 BCC polycrystal

In BCC materials, slip may occur on 48 individual slip systems. These systems represent three families of planes : 12 systems are in the $< 111 > \{110\}$ family, 12 in the $< 111 > \{112\}$ family, and 24 in the $< 111 > \{123\}$ family. Approximate material behavior can be computed by considering a subset of the total number of

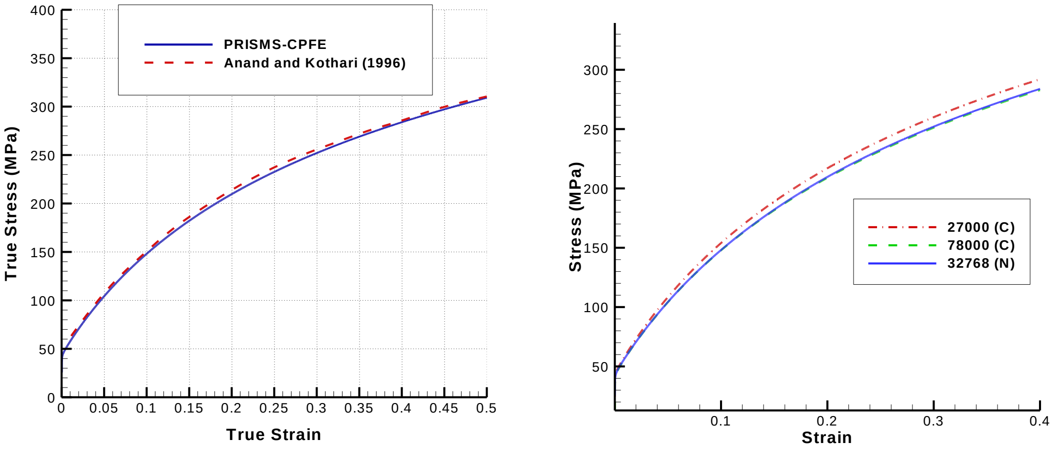

a) b)

Figure 2.9: Stress-strain curves for simple compression of a 200 grain polycrystal for Copper microstructure a) comparison of PRISMS-Plasticity with [12] b) convergence of stress-strain curves with no. of elements for conforming (C) and non-conforming (N) mesh.

slip systems, only the $< 111 > \{110\}$ family of slip systems is considered in a 92 grain microstructure of β Ttitanium alloy Timetal 21S which is studied in [81].

For comparison with PRISMS-Plasticity, the values for the slip hardening parameters and initial value of the slip deformation resistance for β Ttitanium are considered and are taken from [81], also available in Appendix C.

$$h_0 = 1500MPa \quad s_s = 500MPa \quad a = 0.1 \quad s_0 = 200.0MPa \tag{2.40}$$

Fig. 2.10 a) shows the comparison of the stress-strain curve obtained from PRISMS-Plasticity with the rate-independent model considered in [81]. The PRISMS-Plasticity model is able to capture the stress-strain curve of the Titanium polycrystal. Fig. 2.10 b) shows the convergence of the stress-strain curve with increasing the number of elements. The time scaling of the problem is shown in Fig. 2.6 and the visualization plots of stress, inverse pole figure maps and pole figures are shown in Figs. 2.11, 2.13 and 2.14 respectively.

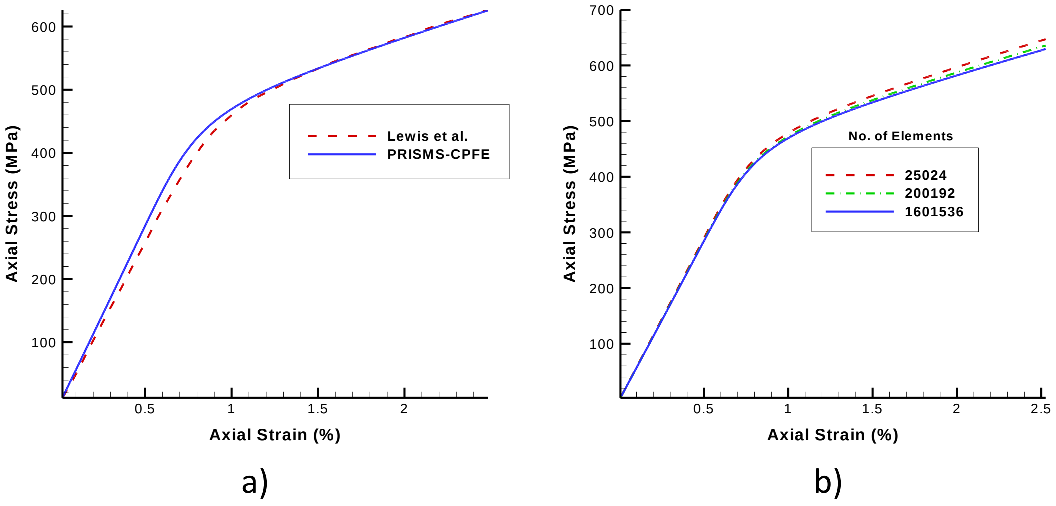

Figure 2.10: Stress-strain curves for simple tension of a 92 grain polycrystal for β Ttitanium real microstructure [81] a) comparison of PRISMS-Plasticity with [81] b) convergence of stress-strain curves with no. of elements.

2.5 Visualization

The output of the CPFE simulations can be visualized using popular open-source visualization tools such as ParaView [8] and VisIt [33]. Paraview is an open-source, multi-platform data analysis and visualization application. MTEX is a free Matlab toolbox for analyzing and modeling crystallographic textures by means of EBSD or pole figure data [15]. In this study, we use ParaView and MTEX to visualize the deformation, stress, strain contours and texture of the resultant microstructures. Fig. 2.11 shows the von Mises equivalent stress mapped on the deformation field using Paraview and the axial strain that outputs from the PRISMS-plasticity code. ParaView has tools to visualize microstructures by thresholding, clipping and slicing the microstructure as shown in Fig. 2.12 . The inverse pole figures maps and pole figures for the BCC microstructure are shown in Fig. 2.13 and Fig. 2.14.

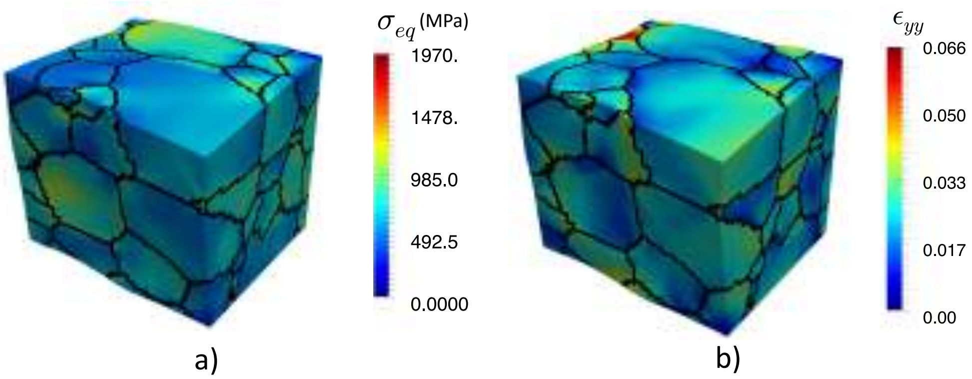

Figure 2.11: Visualization of (a) von Mises equivalent stress and (b) axial strain on a deformation field(x5) using ParaView.

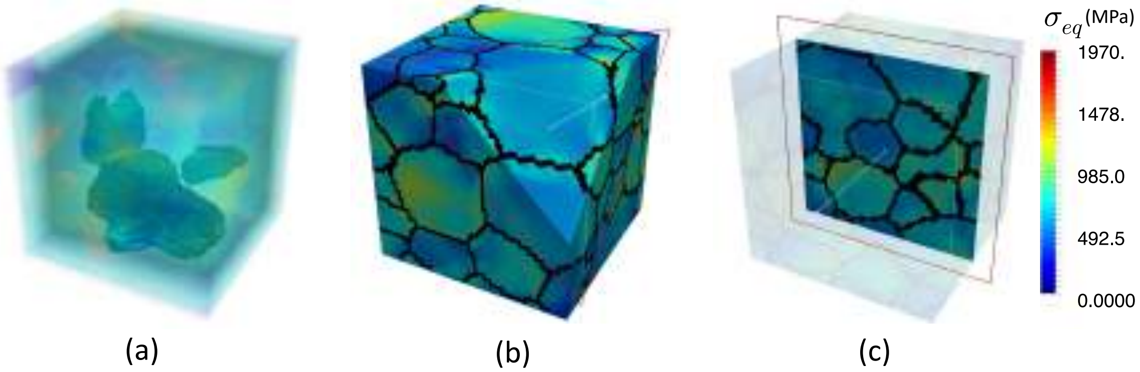

(a) (b) (c)

Figure 2.12: Visualization of von Mises equivalent stress using (a) threshold (b) clip (c) slice options in ParaView.

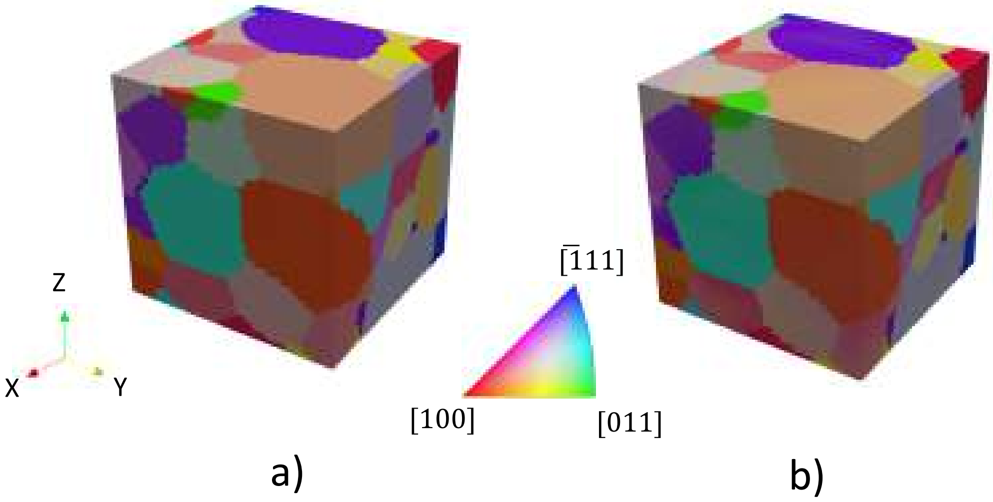

Figure 2.13: Visualization of Inverse Pole Figure (IPF) maps of BCC Titanium microstructure using MTEX (a) before deformation (b) after deformation.

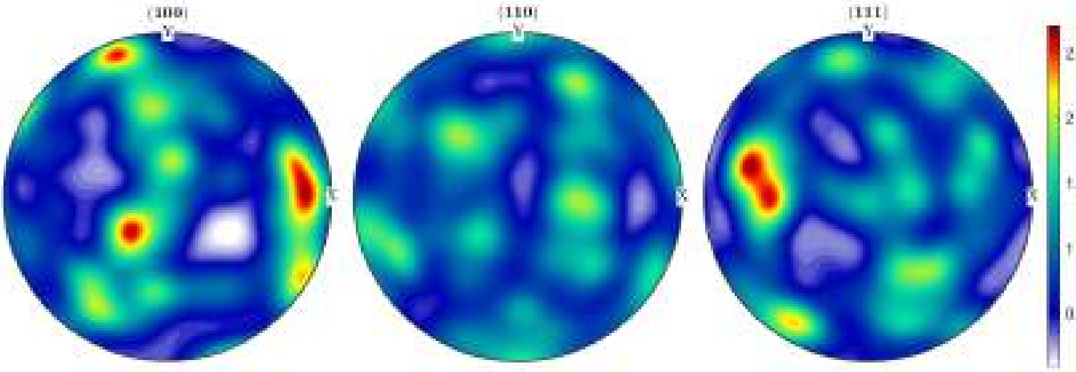

Figure 2.14: Visualization of Pole Figures for BCC Titanium microstructure using MTEX.

CHAPTER III

Calibration of slip and twin parameters in HCP alloys

In this chapter, a methodology to construct a Representative Volume Element (RVE) with a similar texture to the one observed in the experiments is described. This makes use of orientation distribution function (ODF) to represent the texture of the microstructure. Using stress-strain curves obtained from experiments and a texture matched RVE obtained from Neper [82], the parameters required for crystal plasticity simulations are identified. Section 3.1 provides the background for ODF and the procedure to compute the independent nodal values A^{node}. Section 3.2 describes the procedure to construct the RVE of the microstructure with the use of a texture matching procedure. In section 3.3, the results of the convergence studies, calibration of CPFE parameters, the relative activity of the slip systems and pole figures are discussed.

3.1 Mathematical background

The complete orientation space of a polycrystal can be reduced to a smaller subset, called the fundamental region (Fig. 3.1), as a consequence of crystal symmetries. Within the fundamental region, each crystal orientation is represented uniquely by

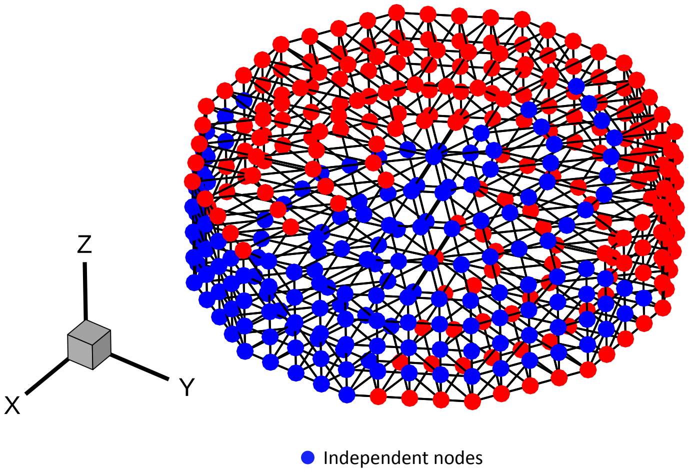

Figure 3.1: ODF representation in the Rodrigues fundamental region for hexagonal crystal symmetry showing the location of the k=388 independent nodes of the ODF in blue color.

a coordinate, r, the parametrization for the rotation (e.g. Euler angles, Rodrigues vector etc.). The ODF, represented by $\mathcal{A}(r)$, describes the volume density of crystals of orientation r. The fundamental region is discretized into N independent nodes with N_{elem} finite elements (and N_{int} integration points per element) as shown in Fig. 3.1.

The ODF is normalized to unity over the fundamental region as:

$$\boldsymbol{\int_{\mathcal{R}} \mathcal{A} dv = \sum_{n=1}^{N_{elem}} \sum_{m=1}^{N_{int}} A(r_m) w_m |J_n| \frac{1}{(1 + r_m \cdot r_m)^2} = 1} \tag{3.1}$$

where $A(r_m)$ is the value of the ODF at the m^{th} integration point with global coordinate r_m of the n^{th} element, $|J_n|$ is the Jacobian determinant of the n^{th} element and w_m is the integration weight associated with the m^{th} integration point. This is equivalent to the linear constraint: ${q^{int}}^T A^{int} = 1$, where $q_i^{int} = w_i |J_i| \frac{1}{(1+r_i \cdot r_i)^2}$ and $A_i^{int} = A(r_i)$, where $i = 1, \ldots, N_{int} \times N_{elem}$.

Using reduced integration with one integration point per element at local coordinate of $(0.25, 0.25, 0.25)$ and an integration weight of $w = \frac{1}{6}$, the simplified matrix q^{int} corresponding to the normalization Eq. 3.1 is given as:

$$\boldsymbol{q} = \begin{bmatrix} \frac{1}{6}|\boldsymbol{J_1}|\frac{1}{(1+\boldsymbol{r_1}\cdot\boldsymbol{r_1})^2} \\ \frac{1}{6}|\boldsymbol{J_2}|\frac{1}{(1+\boldsymbol{r_2}\cdot\boldsymbol{r_2})^2} \\ \cdots \\ \frac{1}{6}|\boldsymbol{J_{N_{el}}}|\frac{1}{(1+\boldsymbol{r_{N_{el}}}\cdot\boldsymbol{r_{N_{el}}})^2} \end{bmatrix}$$

Crystallographic symmetry is enforced by considering the set of independent nodal points instead of the integration points. Independent nodal points are the reduced set of nodes obtained by accounting for symmetry conditions at the boundaries of the ODF (see Fig. 3.1). Let matrix H be such that it converts the independent nodal values to the integration point values $A^{int} = HA^{node}$. The H matrix can be defined from the equation $A^{int}_e = 0.25\sum_{i=1}^{4} A^i_e$ where A^{int}_e is the integration point ODF value at element e and $A^i_e, i = 1, \ldots, 4$ refers to the ODF values at the four nodes of the tetrahedral element e. The q matrix is formed as $q = H^T q$ so that normalization can be represented as the scalar product $q^T A$ with the ODF values (A) at the independent nodal points.

The orientations from the EBSD data are binned pixel–by–pixel to the element containing the orientation, specifically to the integration point in the element. After binning is complete, the ODF value (A^{int}_i) at the integration point in an element i contains the total number of pixels in the EBSD image that have orientations lying within the element. The data is then normalized by ${q^{int}}^T A^{int}$. We use matrix T to convert the integration point values A^{int} to the independent nodal values A^{node}, ie., $A^{node} = TA^{int}$. Using one integration point, this matrix is defined as $T_{ij} = \delta_{ij}/f$ where δ_{ij} is one if node i (or its symmetric equivalent) is a vertex of element j and zero otherwise. The factor f is the number of elements with node i (or symmetric equivalent) as one of its vertices. This matrix is always positive and thus, $A^{node} \geq 0$.

Once the ODF (A^{node}) is obtained, it is sampled to the RVE obtained from Neper.

3.2 Construction of Representative Volume Element

The representative volume element for the polycrystal was constructed with open-source software package Neper [82]. Multiple RVE's with centroidal voronoi tessellation were generated using Lloyd's algorithm [66] to represent the microstructure with the grains. As grain size effects were not considered in the current computation, centroidal voronoi tessellation ensures well-shaped and uniformly sized convex cells. The presence of larger number of grains in the RVE allows it to map to the experimental texture accurately. Fig. 3.2 shows the microstructures of 1000 grains used in the study, termed RVE1 and RVE2. The microstructures generated from Neper were matched to a weakly basal texture as observed in the experiments as described next.

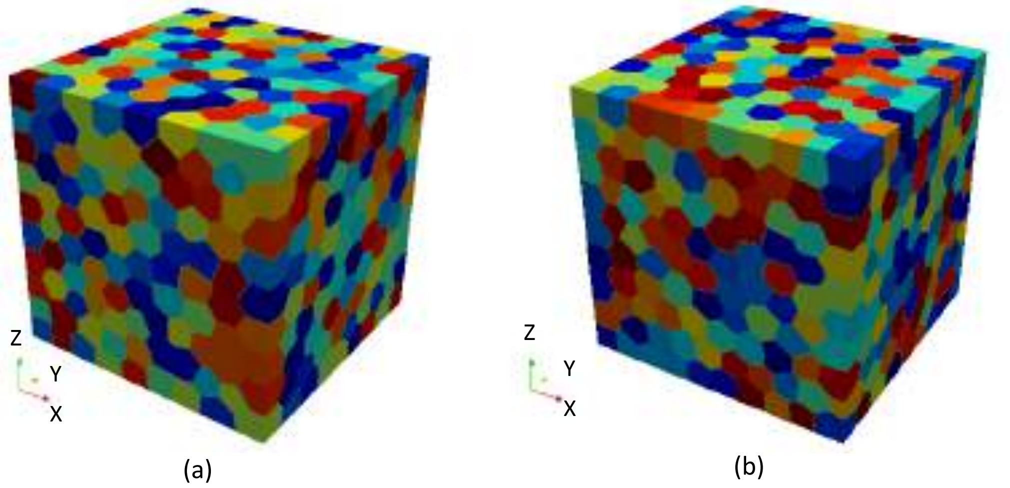

Figure 3.2: Microstructures considered in the study constructed from Neper (a) RVE1 (b) RVE2

3.2.1 Texture-matching procedure

Once the ODF is obtained, it is matched to the microstructure using a texture matching algorithm. The ODF (A^{node}) is matched to the RVE by assigning the orientations of independent nodes to the individual grains of the microstructure. Fig. 3.3 shows the texture match for 1000 grains with the ODF for both T5 and T6 temper. The ODF values ($q_i A_i$) are multiplied by the number of grains (N). Each ODF then is N$q_i A_i$ contains the approximate number of grains that constitute that orientation. However, two issues occur. Firstly, the volumes of all grains are not equal. Secondly, the values ($q_i A_i$) are in the form of fractions. We split each value of N$q_i A_i$ into equal parts(P$_i$) by dividing it with its rounded number (eg. 3.3 split into 3 parts of 1.1 each). The number obtained ranges from 0.6-1.4 in our case. These numbers can be directly matched to the relative grain volumes (defined as $NV_i/(\Sigma_i V_i)$, N : no. of grains, V$_i$: volume of each grain) of different grains. Larger grains are assigned to orientations of grains with larger P$_i$ values. It is to be noted that more number of grains leads to a better match between the curves. Here, we define texture match error as the L^1-norm of the difference of the weighted ODF (${q^{int}}^T A^{int}$) between the texture of the sample and RVE of the microstructure.

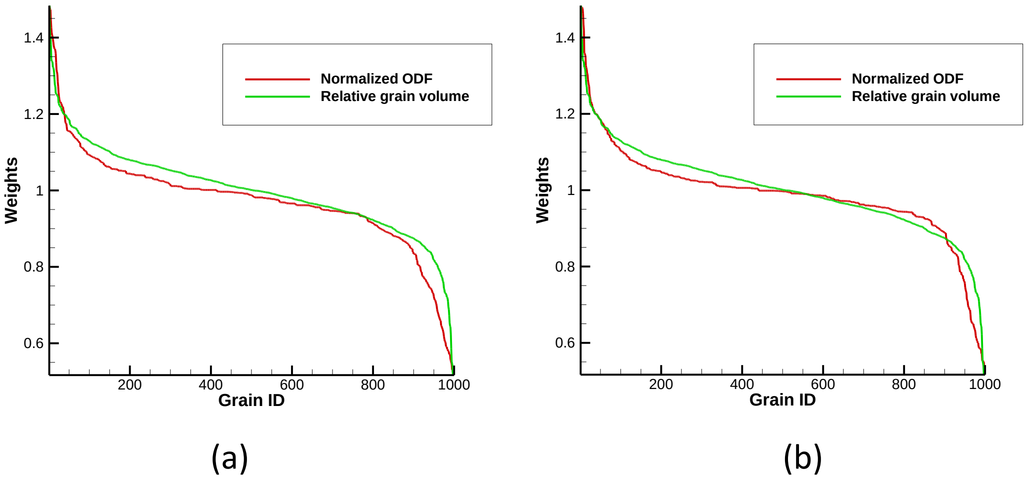

Figure 3.3: The texture-match algorithm works by matching the relative grain volume to the weight of the normalized odf (a) T5 temper (b) T6 temper

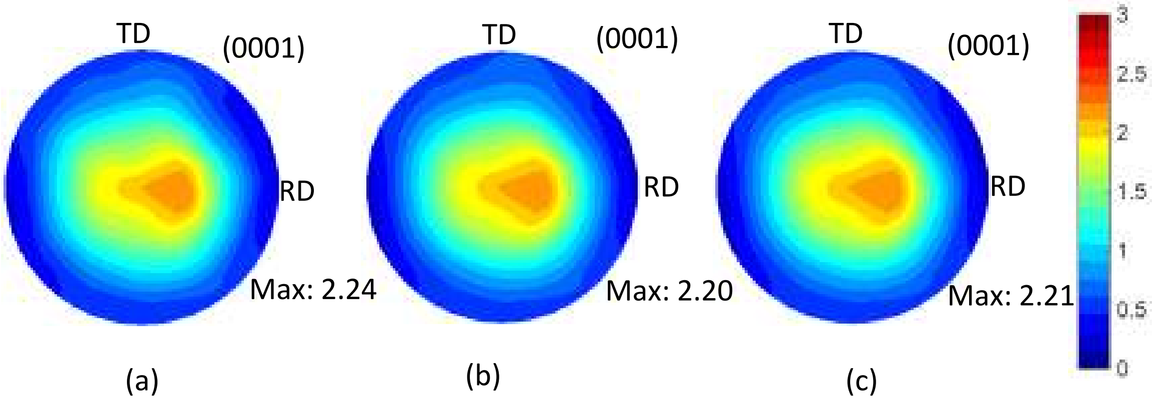

Figure 3.4: The (0001) calculated pole figures for WE-43 T5 a) EBSD data b) RVE 1 c) RVE2

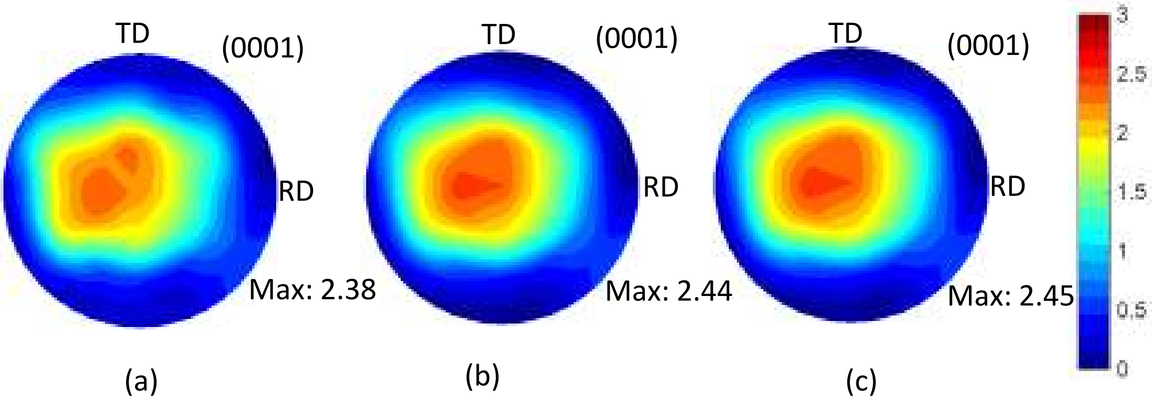

Figure 3.5: The (0001) calculated pole figures for WE-43 T6 a) EBSD data b) RVE 1 c) RVE2

3.3 Results

3.3.1 Convergence

The stress-strain response under tension is studied as a function of increasing number of elements per grain in the CPFE model in Fig. 3.6 (a). The RVE used for this study is comprised of 500 grains which were generated from Neper. We see that the response changes about 10% from a 16 element/grain mesh to the 686 element/grain mesh. Convergence to 1% difference is seen when 432 elements/grain on average was used. Rest of the results use a conservative number of 1000 number of elements/grain. Fig. 3.6 (b) shows that the results are insensitive to the RVE used in the CPFE model, with both RVEs having different grain distribution but overall same texture, grain number and average grain size.

In addition, we also studied the error in texture comparison as a function of number of grains used in the model. The error as expected reduces with number of grains, but also reaches an error less than 0.1 for 500 grains and above. The stress-strain response in Fig. 3.7 (b) shows that the average stress increases with the number of grains but mostly converges at about 500 grains. The comparison of (0001) pole figures for the experimental texture, RVE1 and RVE2 is shown in Figs. 3.4 and 3.5.

3.3.2 Calibration of CP parameters

CP parameters were found by optimization from tension/compression experiments for T5 and T6 alloys. Both alloys have a tension-compression response asymmetry due to twinning (as described in later chapters). T5 also has a significantly higher yield strength due to its smaller grain size. In CPFE, grain size effect is not explicitly modeled using Hall-Petch or gradient plasticity. Instead we consider calibrating T5 and T6 with different CP parameters reflecting the stress-strain responses of T5 and T6.

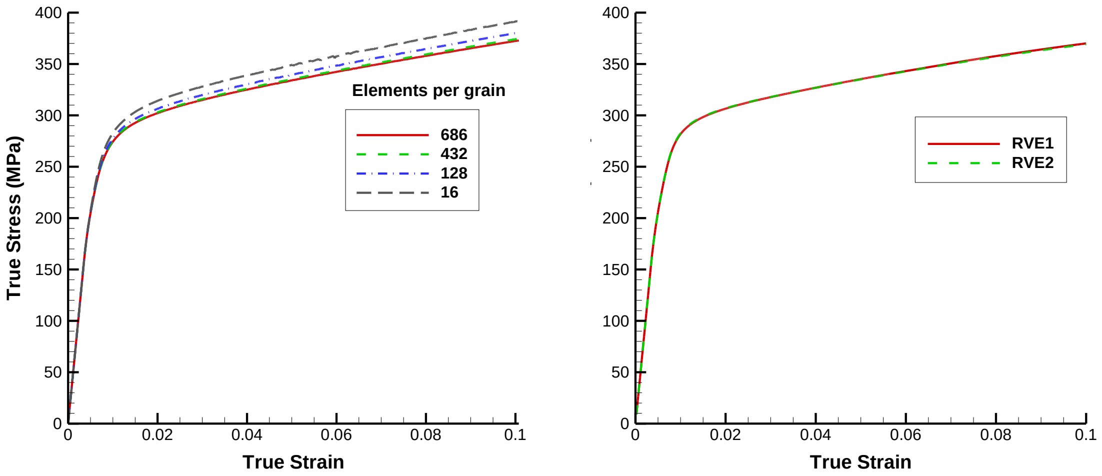

a) b)

Figure 3.6: (a) Convergence of stress-strain curves with number of elements/grain for tension (b) Comparison of stress-strain curves for two different RVE 's

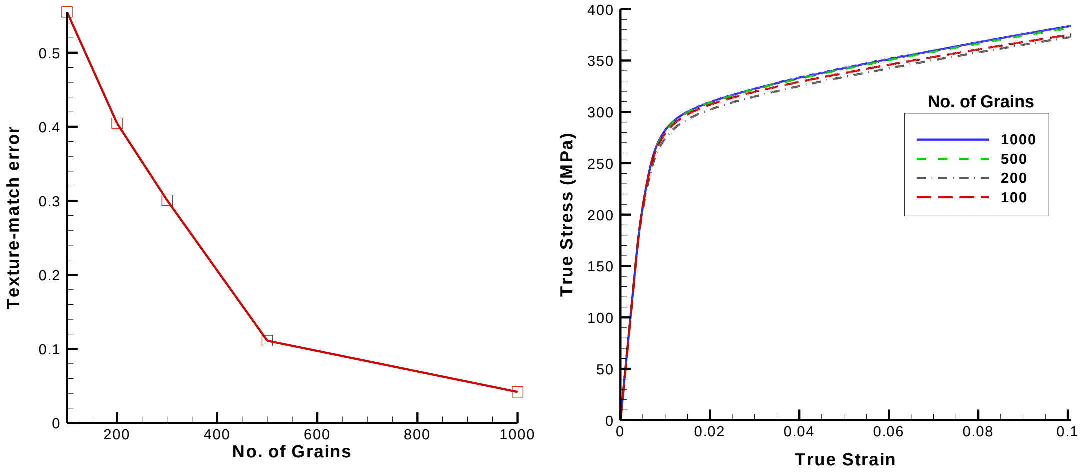

(a) (b)

Figure 3.7: (a) Texture-match error for T5 temper as a function of number of grains (b) Comparison of stress-strain curves for different number of grains in the RVE

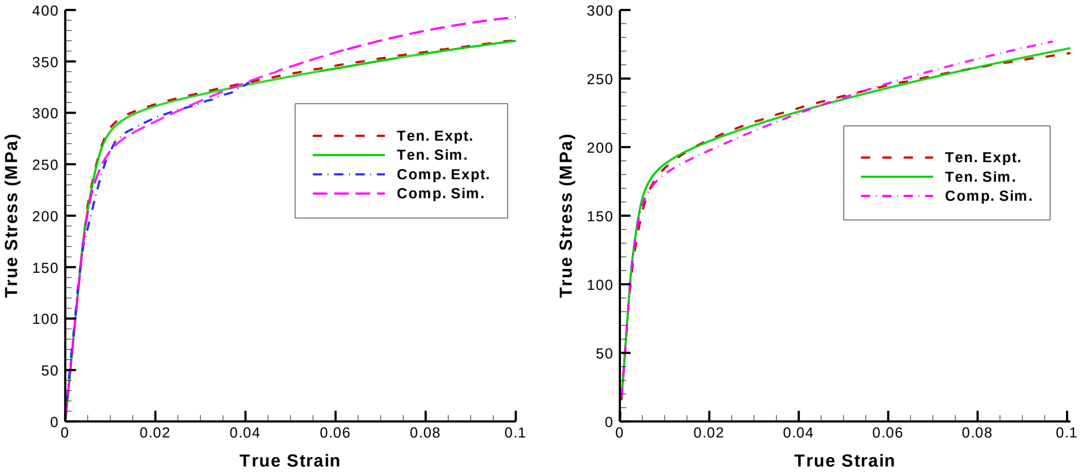

(a) (b)

Figure 3.8: Stress-strain curve of (a) WE43 T5 temper and (b) WE43 T6 temper in the RD direction.

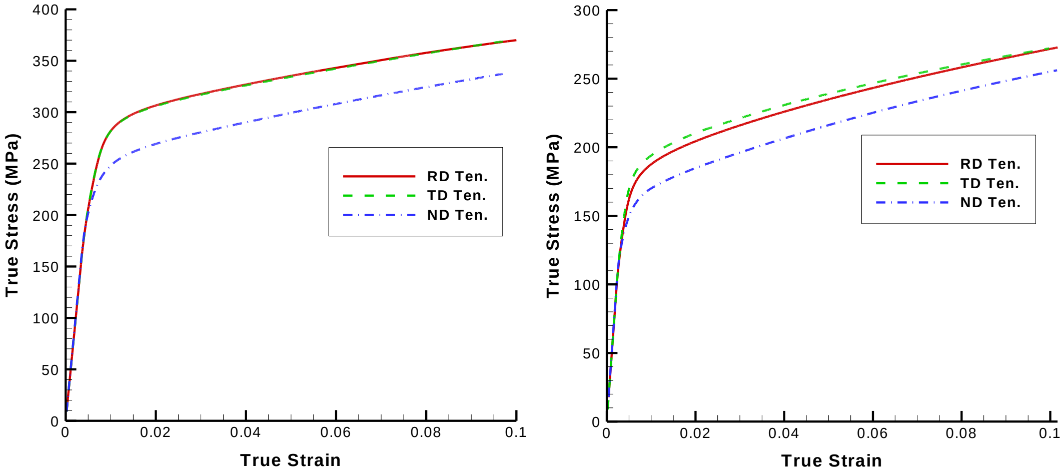

(a) (b)

Figure 3.9: Comparison of stress-strain curve of (a) WE43 T5 temper and (b) WE43 T6 temper in tension CPFE simulation across different loading directions.

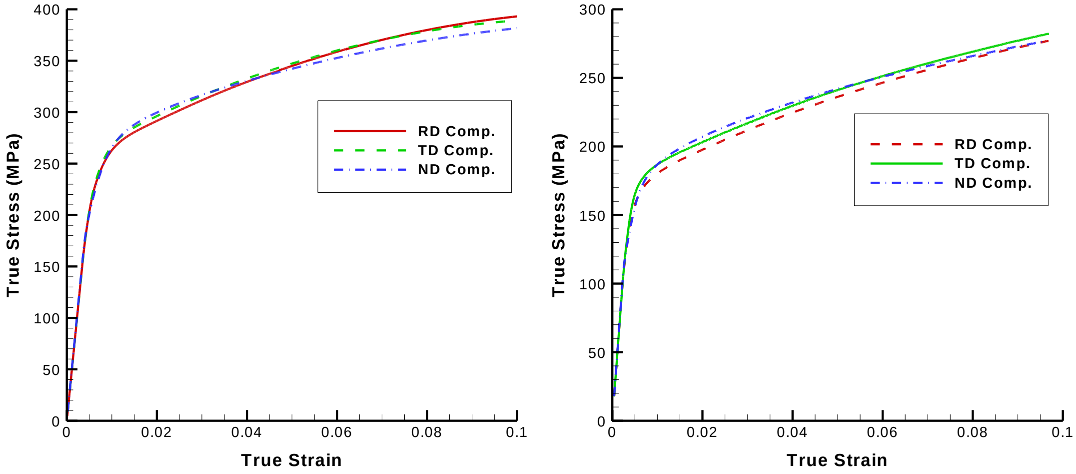

(a) (b)

Figure 3.10: Comparison of stress-strain curve of (a) WE43 T5 temper and (b) WE43 T6 temper in compression CPFE simulation across different loading directions.

Fig. 3.8 (a,b) shows the stress-strain response of T5 and T6 respectively under tension and compression. The CP parameters were calibrated by a gradient optimization approach starting from the parameters of WE43 T5 published in literature [23]. The goal was to minimize the L2 norm of the error between the experimental $\sigma - \epsilon$ curves and the CPFE homogenized curves. The critical resolved shear stresses are compared to those published in literature for this alloy and shown in Table 3.3. The basal slip resistance at 76.0 MPa is higher than in [23, 90], while the twin resistance is lower. The differences between the models are within the deviations expected due to differences in the initial grain sizes, heat treatment, cold work and texture of the alloy and the differences in the modeling approach. For example, [23, 90] did not employ pyramidal$_{<a>}$ mechanism, but it is included here since some of the slip traces observed were close to the pyramidal$_{<a>}$ plane. In general, multiple solutions can exist that leads to the same homogenized response. The effect of this parameter uncertainty can be studied either through sensitivity analysis or through methods of

Table 3.1: Value of elastic parameters for single crystal HCP Magnesium alloys [57]

C_{11}	C_{12}	C_{13}	C_{33}	C_{55}
$59.3 GPa$	$25.7 GPa$	$21.4 GPa$	$61.5 GPa$	$16.4 GPa$

uncertainty quantification [4]. In chapter 5, we demonstrate the effect of changing the slip resistance values on the predominantly activated slip systems within each grain and compare the active slip systems to experimental measurements. This gives a direct guidance to the user as to which parameters are most and least sensitive to the obtained microstructural response.

Table 3.2: Slip resistance and hardening parameters for simulating stress-strain curves in T5 temper

Mode	**s_0 (MPa)**	**h_0(MPa)**	**s_s(MPa)**	**a**
Basal<a>	76.0	225.6	248.7	1.0
Prism<a>	163.2	124.9	356.3	1.0
Pyram<a>	160.3	120.2	347.8	1.0
Pyram<c+a>	187.4	237.9	350.4	1.0
Twin<c+a>	116.4	105.6	238.3	1.0

Table 3.3: Comparison of CRSS of individual modes for T5 temper from [90] and [23]

Mode	**s_0-CPFE (MPa)**	**s_0-Stanford(MPa)**	**s_0- EPSC (MPa)**
Basal<a>	76.0	68	68
Prism<a>	163.2	179	145
Pyram<a>	160.3	-	-
Pyram<c+a>	187.4	273	210
Twin<c+a>	116.4	106	130

The overall parameters are given in Table 3.2 and 3.3. It is seen that the $\boldsymbol{s_0}$(CRSS) is higher in T5 reflecting the lower grain size and higher initial yield stress. However, the hardening rates in T6 are higher than T5 reflecting the steeper increase in stresses during loading owing to the increased rate of twinning in this alloy. The saturation stress is not critical to the model and is useful when higher strains reaching the point of Ultimate Tensile Strength (UTS) are modeled. Currently, the comparison is for 10% experimental strain.

Table 3.4: Slip resistance and hardening parameters for simulating stress-strain curves in T6 temper

Mode	**s_0 (MPa)**	**h_0(MPa)**	**s_s(MPa)**	**a**
Basal<a>	47.6	595.0	144.4	2.5
Prism<a>	92.2	412.1	289.0	2.5
Pyram<a>	104.5	373.2	347.5	2.5
Pyram<c+a>	117.3	321.1	304.9	2.5
Twin<c+a>	84.4	419.3	148.8	2.5

The material also has considerable tensile anisotropy as shown in Figs. 3.9 (a) and (b). Due to the weakly basal texture, the yield stress is higher in RD and TD loading compared to loading in the ND direction. RD and TD are equivalent due to basal texture symmetry (in plane). In compression Fig. 3.10 a), b), this symmetry exists but not as pronounced. The reasons behind this anisotropy in Figs. 3.9 and 3.10 can be explained by plotting the activity of different slip and twin systems under tension and compression in different loading directions.

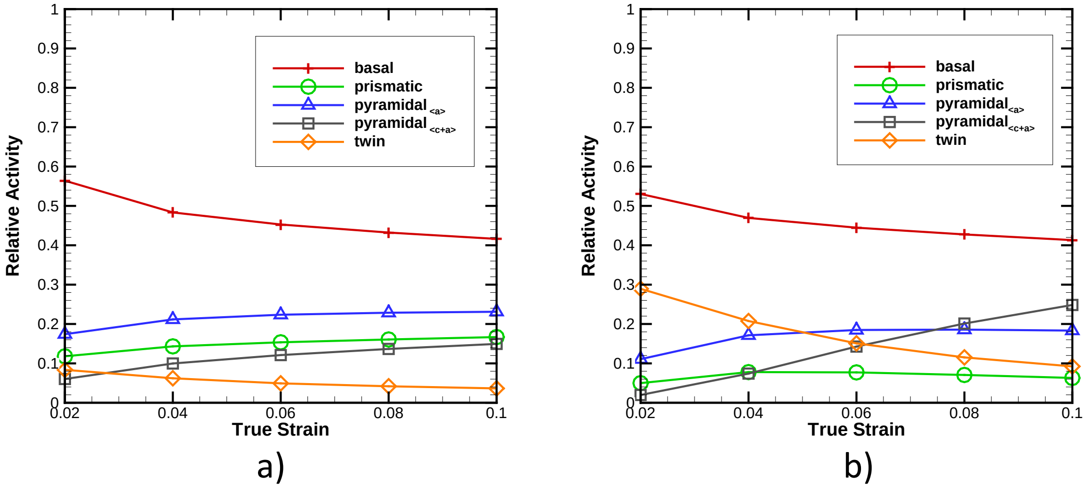

Figure 3.11: Relative activity of slip modes during a) Tension b) Compression along RD in T5 temper

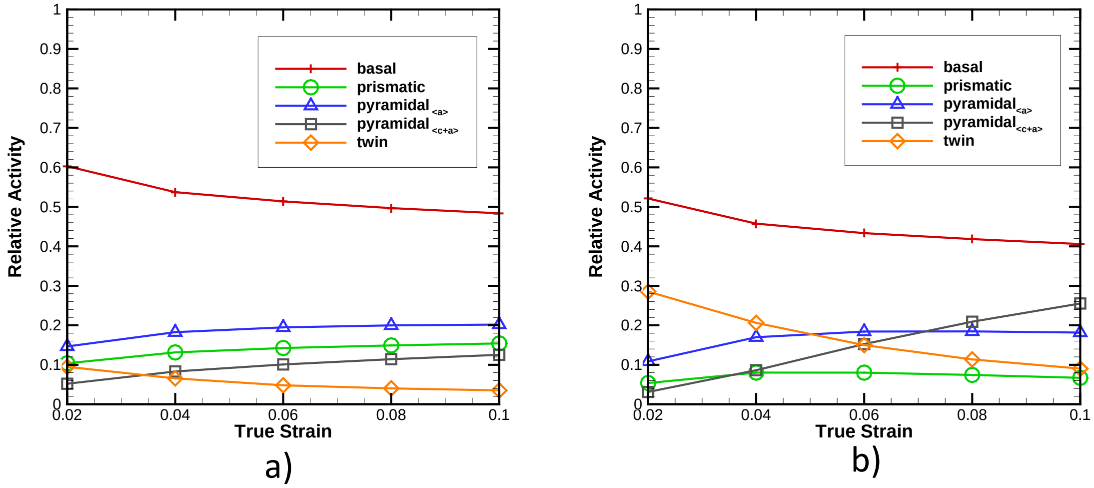

a) b)

Figure 3.12: Relative activity of slip modes during a) Tension b) Compression along TD in T5 temper

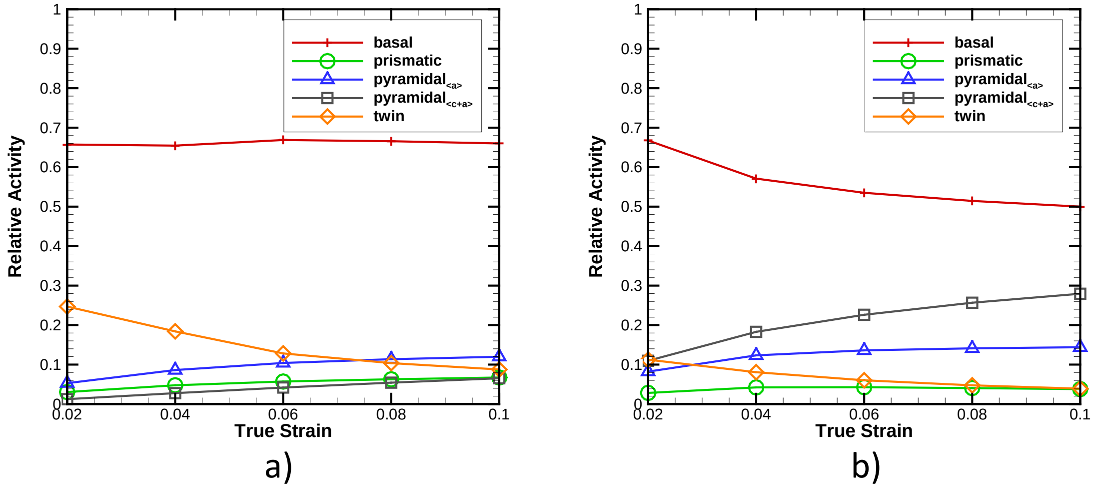

a) b)

Figure 3.13: Relative activity of slip modes during a) Tension b) Compression along ND in T5 temper

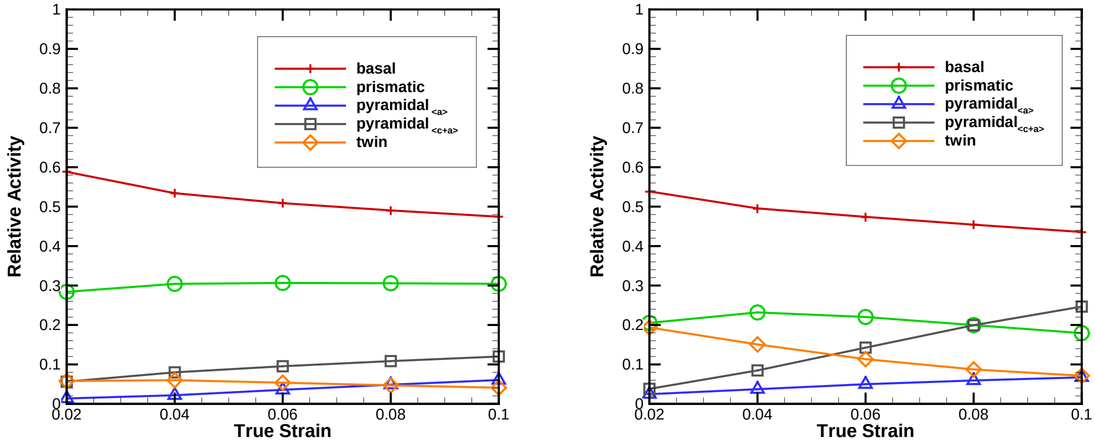

a) b)

Figure 3.14: Relative activity of slip modes during a) Tension b) Compression along RD in T6 temper

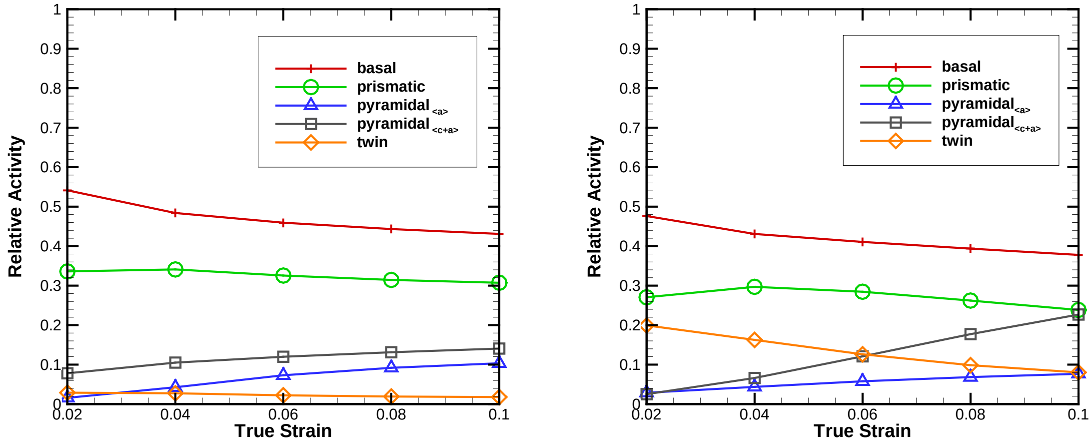

a) b)

Figure 3.15: Relative activity of slip modes during a) Tension b) Compression along TD in T6 temper

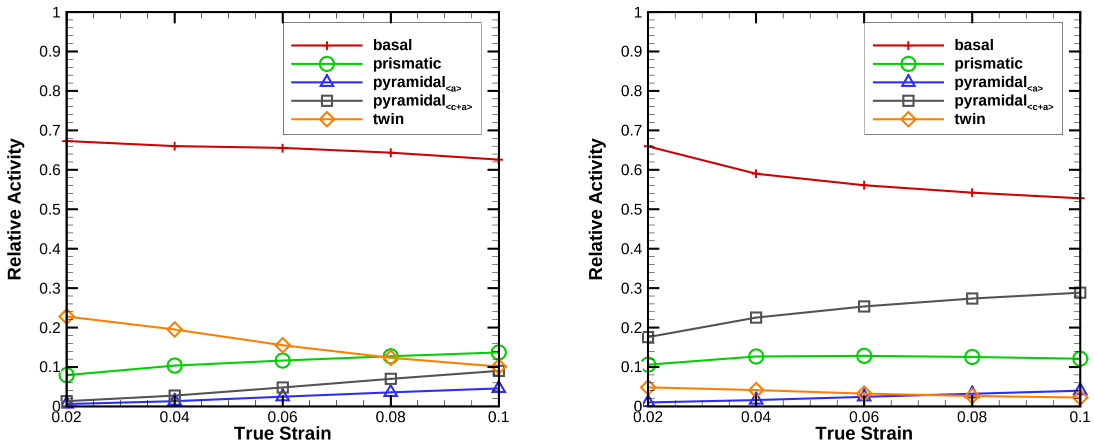

a) b)

Figure 3.16: Relative activity of slip modes during a) Tension b) Compression along ND in T6 temper

3.3.3 Relative activity of the slip systems

Relative activity of a slip deformation mode is defined as the ratio of the sum of shear strain due to that deformation mode over the total plastic shear accumulated in the microstructure. Fig. 3.11 shows the relative activity of the slip modes during tension and compression along RD direction (note the elastic region is not shown). In all cases, basal has the lowest CRSS and is most active at low strain levels. The difference between tension and compression is the twinning system which is active in compression. The $< c >$ direction deformation modes for a grain are either twinning or pyramidal$_{<c+a>}$. Both modes compete with each other in compression with twinning more active at low strains and pyramidal$_{<c+a>}$ more active at higher strains. Interestingly, in T5, pyramidal$_{<a>}$ is more active than the prismatic mode, as expected from the CRSS values calibrated. But this result is sensitive to the initial texture. Fig. 3.12 shows similar trend in TD direction. Pyramidal$_{<a>}$ has not been used in several previous studies on Mg alloy; as we see later for DIC slip trace analysis, this system is active in T5 alloy and competes with the prismatic system.

The trend for twinning is reversed when loaded in the ND direction as seen from the relative activity plot in Fig. 3.13. The activity of twinning system is high in ND-tension leading to the tension-compression anisotropy seen in Fig. 3.9 (a) for tension. Under ND-compression pyramidal$_{<c+a>}$ becomes the $< c >$ axis deformation mode and the anisotropy is less pronounced as seen in Fig. 3.10 (a).

Relative slip activity in the T6 alloy again shows high basal activity as expected in all loading directions and mode. In RD loading, prismatic is the predominant system and pyramidal$_{<c+a>}$ is significantly less active compared to T5. Interesting, this shows that differences in grain sizes affects different slip systems differently and could be a case of future study. Pyramidal$_{<a>}$ is the least active slip system in T6. Beyond the observation, the tensile anisotropy has a similar reason (effect of twinning) in T5 and T6 alloys. Comparing Figs. 3.13 a) and 3.16 a), the twinning system is more active in ND tension loading, leading to anisotropic response.

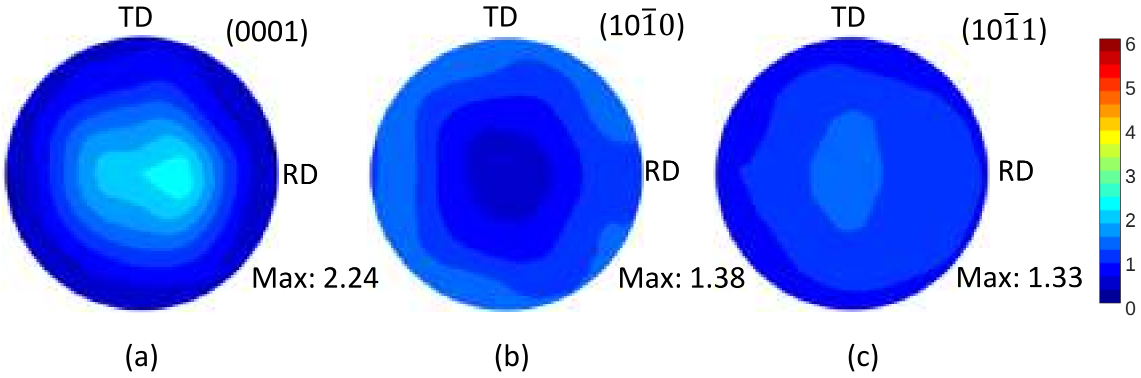

Figure 3.17: Initial texture of the WE-43 T5 plate before deformation a)(0001) b) (10$\bar{1}$0) c) (10$\bar{1}$1)

3.3.4 Pole figures

The pole figures in tension and compression for both alloys are as expected. Figs. 3.17 and Fig. 3.24 show the initial textures for T5 and T6 respectively. Under compression, both alloys realign the $< c >$ axis in the compression direction. Figs.

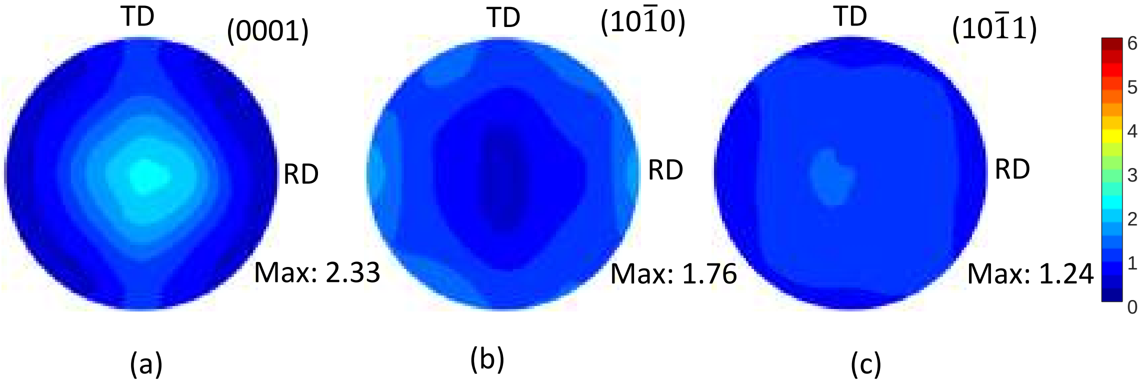

Figure 3.18: Simulated texture of WE-43 T5 after 10% tensile strain along RD a)(0001) b) (10$\bar{1}$0) c) (10$\bar{1}$1)

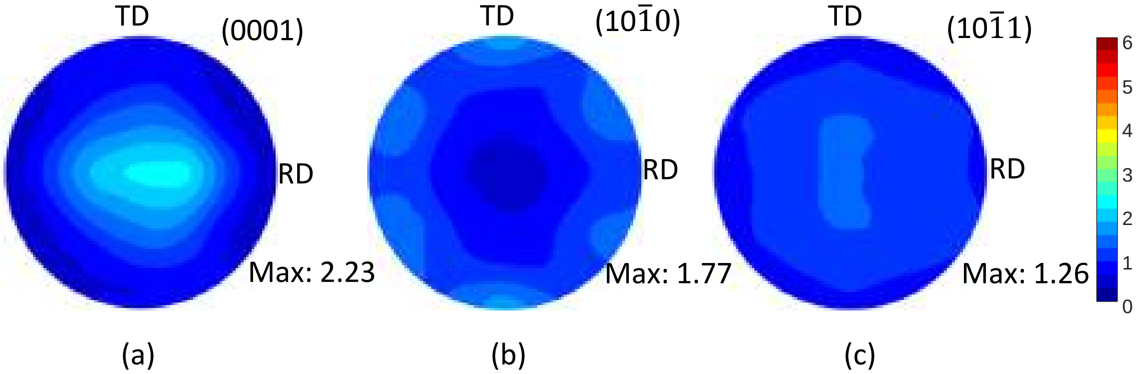

Figure 3.19: Simulated texture of WE-43 T5 after 10% tensile strain along TD a)(0001) b) (10$\bar{1}$0) c) (10$\bar{1}$1)

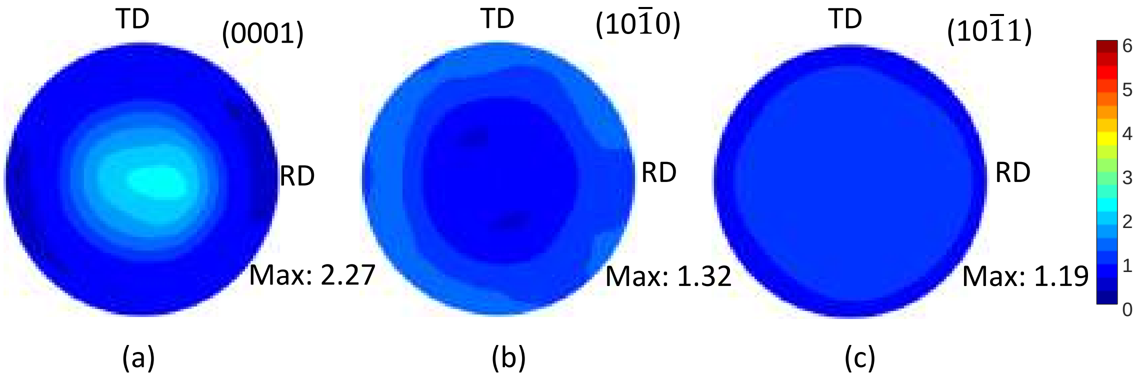

Figure 3.20: Simulated texture of WE-43 T5 after 10% tensile strain along ND a)(0001) b) (10$\bar{1}$0) c) (10$\bar{1}$1)

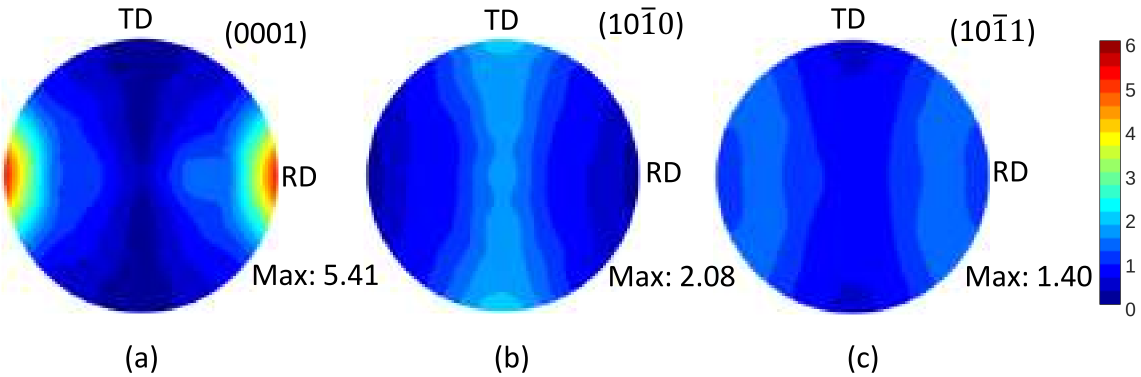

Figure 3.21: Simulated texture of WE-43 T5 after 10% compressive strain along RD a)(0001) b) (10$\bar{1}$0) c) (10$\bar{1}$1)

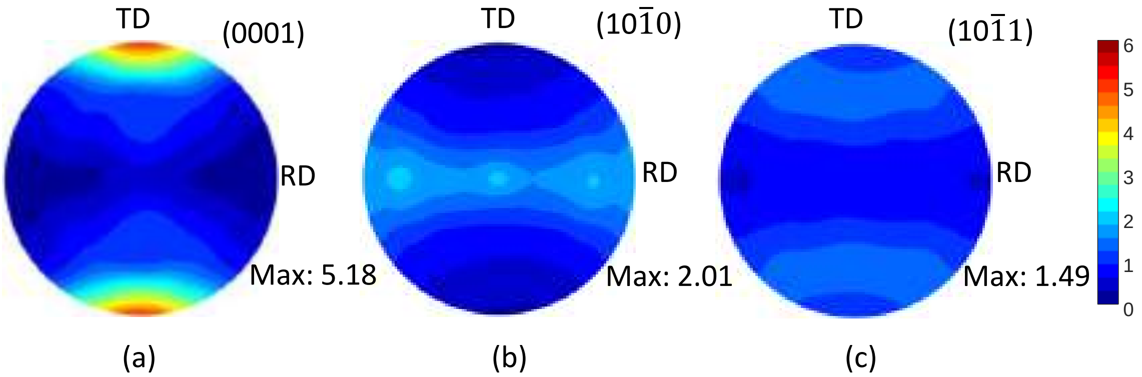

Figure 3.22: Simulated texture of WE-43 T5 after 10% compressive strain along TD a)(0001) b) (10$\bar{1}$0) c) (10$\bar{1}$1)

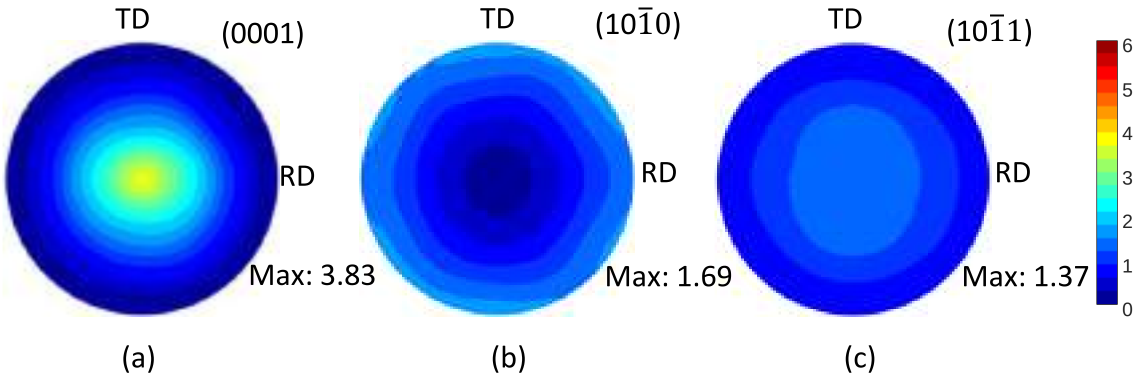

Figure 3.23: Simulated texture of WE-43 T5 after 10% compressive strain along ND a)(0001) b) (10$\bar{1}$0) c) (10$\bar{1}$1)

3.21-3.23 shows $< c >$ axis moving to the RD poles under compression along RD, TD poles under compression along TD and ND pole under compression along ND direction respectively. The primary mechanism here being twinning. Under tension the $< c >$ poles scatter minimally normal to the loading axis (along lateral direction) as expected due to low twinning and predominance of basal slip as seen in Figs. 3.18-3.20 for T5 and Figs. 3.25-3.27 for T6 state.

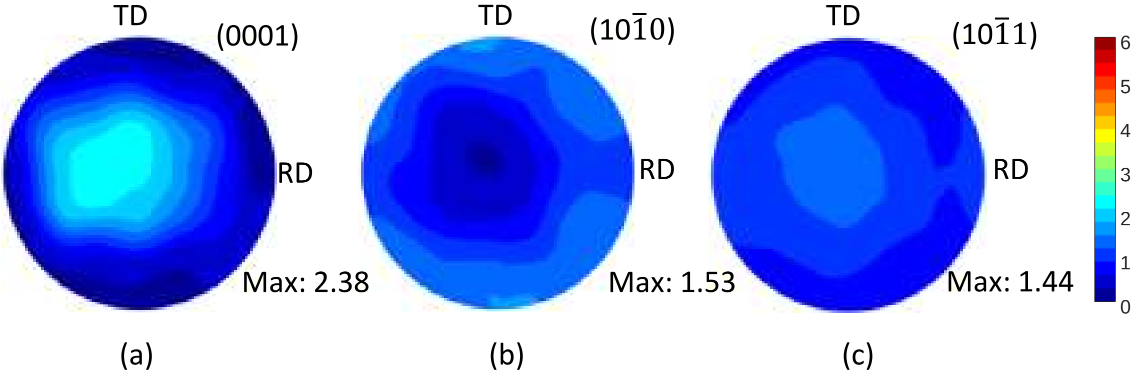

Figure 3.24: Initial texture of the WE-43 T6 plate before deformation a)(0001) b) (10$\bar{1}$0) c) (10$\bar{1}$1)

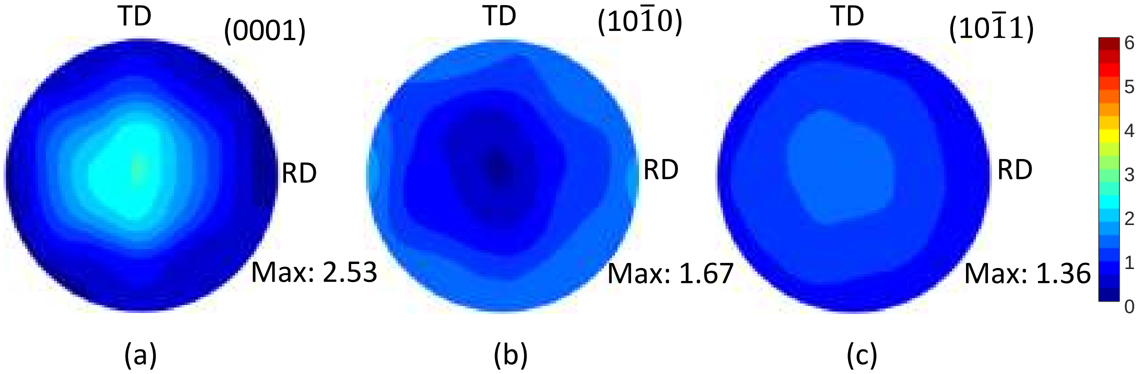

Figure 3.25: Simulated texture of WE-43 T6 after 10% tensile strain along RD a)(0001) b) (10$\bar{1}$0) c) (10$\bar{1}$1)

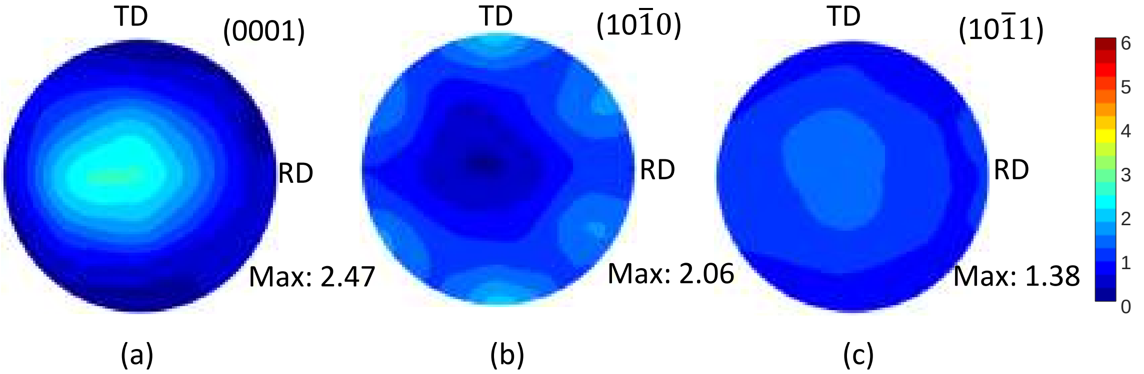

Figure 3.26: Simulated texture of WE-43 T6 after 10% tensile strain along TD a)(0001) b) (10$\bar{1}$0) c) (10$\bar{1}$1)

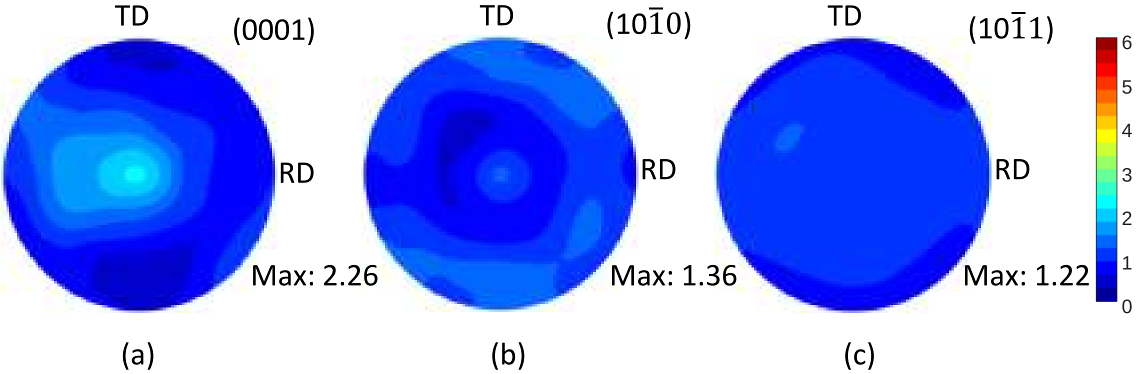

Figure 3.27: Simulated texture of WE-43 T6 after 10% tensile strain along ND a)(0001) b) (10$\bar{1}$0) c) (10$\bar{1}$1)

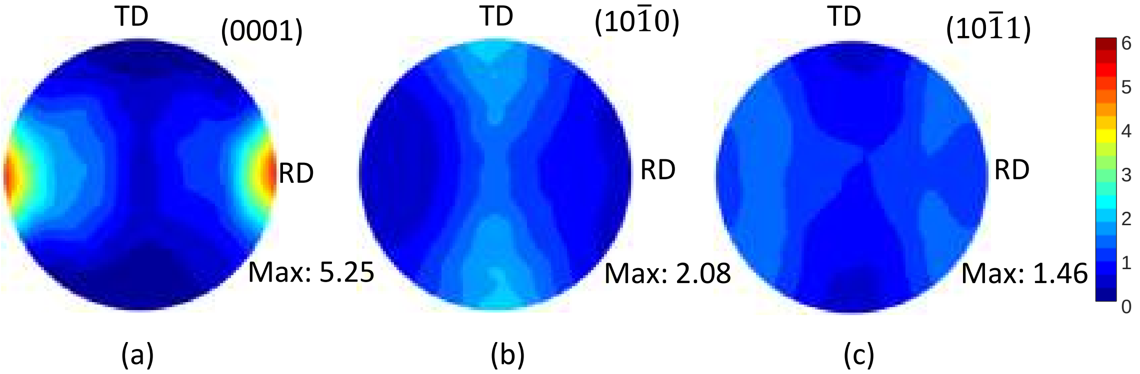

Figure 3.28: Simulated texture of WE-43 T6 after 10% compressive strain along RD a)(0001) b) (10$\bar{1}$0) c) (10$\bar{1}$1)

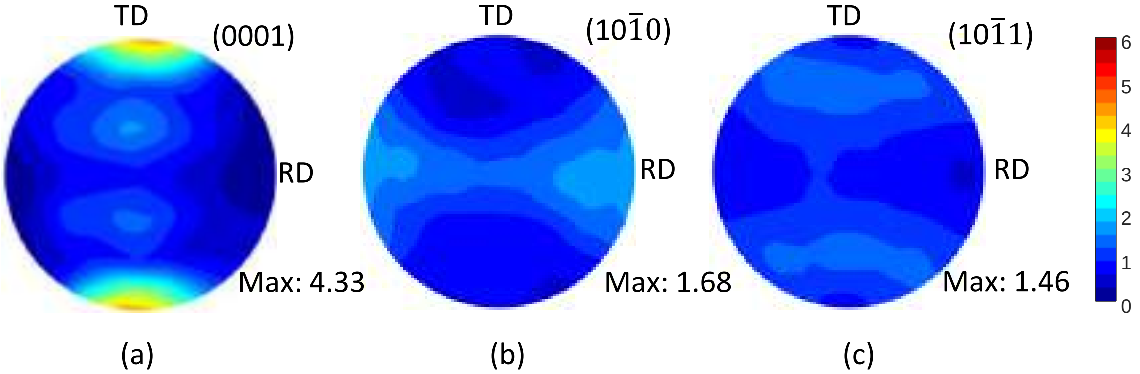

Figure 3.29: Simulated texture of WE-43 T6 after 10% compressive strain along TD a)(0001) b) (10$\bar{1}$0) c) (10$\bar{1}$1)

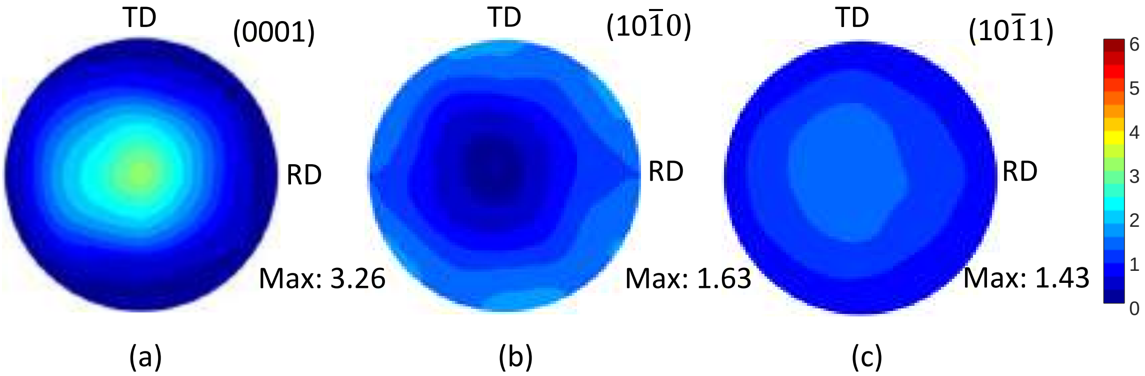

Figure 3.30: Simulated texture of WE-43 T6 after 10% compressive strain along ND a)(0001) b) (10$\bar{1}$0) c) (10$\bar{1}$1)

CHAPTER IV

Crystal plasticity simulations for WE43-T6 alloy and validation of strain maps using SEM-DIC Experiments

4.1 Introduction

Boundary Value Problems (BVP) are set up to compare the SEM-DIC experiments with the crystal plasticity finite element simulations. The methodology to compare the experiments with the simulations is explained and the problem is set-up for WE43-T6 temper. Comparisons are made between the SEM-DIC experiments and CPFE simulations for the displacement and strain fields and the effect of basal schmid factor, grain size , boundary conditions are studied. All the experimental SEM-DIC data were received from Prof. Daly's group [46].

4.2 Boundary Value Problem

The comparison with SEM-DIC experiments is performed by setting up a boundary value problem (BVP) using the EBSD image of the microstructure within the DIC window. The displacement fields in the x and y direction along the boundary of the microstructure are obtained from experiment. The measurements are made on the surface of the sample, which is traction-free, and therefore a plane-stress assumption is made while setting up the simulation. The slip and twin systems are three-dimensional and the algorithm to solve for the shear strains and stresses in the slip systems proceeds from a 3-D deformation gradient. Therefore, it is not possible to set up an explicit plane-stress problem similar to 2-D elasticity. Instead, the problem is set-up in 3-D with a plate of very small thickness. A thickness to length ratio (t/l) of 0.1 was used for all the simulations. Since no variation of variables u and v was expected in the z-direction, a single layer of elements was assumed in the z-direction along with a 200x 200 mesh.

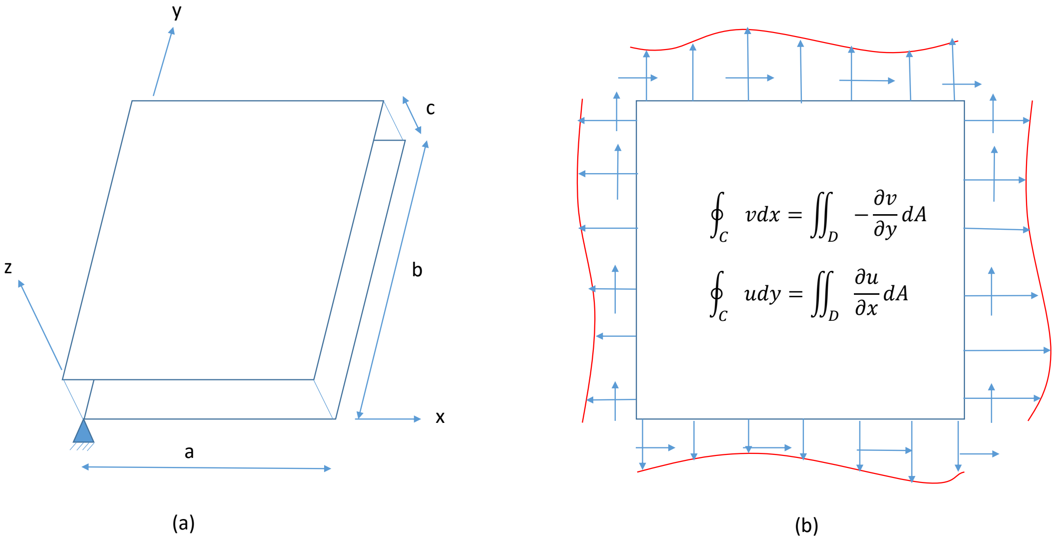

Figure 4.1: Boundary conditions for comparison of CPFE simulations with SEM-DIC experiments. (a) Both the top and bottom surfaces are made traction free with z-displacement set to zero at (x,y,z)=(0,0,0) (b) Application of 2D Stokes' theorem to the boundary value problem where u and v are the displacements in the x and y-direction respectively.

4.3 Results

Point–wise comparison of displacements in Fig. 4.2 reveals a scatter around the DIC displacement with low variance in the results for regions with larger absolute displacement and a tendency for larger variance in regions with low to zero displacement. No particular trend in errors was observed as a function of the basal schmid factor. In general, the range of displacements are controlled by the applied DIC boundary conditions and these constrain the CPFE model from significantly over– or under–predicting the displacements. Given the same surface displacement exists for both the DIC data and CPFE model, the 2D Stokes theorem as shown in Fig. 4.1 (b) gives the averaged strain over the microstructure directly from the surface displacements (assuming no cracks in the microstructure). In general, by taking derivatives of displacements, the existing error in the displacements are amplified. However, the 2D Stokes theorem dictates that if strains are over–predicted in some regions, they should be compensated by under–prediction of strains in some other regions. In DIC data, the strain localizations lead to large displacement jumps and these are ‘smoothed’ by the CPFE model as it does not model localizations and discontinuities finer than the element size used.

Fig. 4.3 shows the larger scatter in strains, and there is a tendency to significantly underpredict the tensile as well as compressive strains due to the lack of sharp localizations in the CPFE model. Strains are also overpredicted in other regions as expected from Stokes theorem. A better comparison would be to use the averaged strain over a grain, in which case the localizations are smoothed out in the DIC data. Fig. 4.4 compared the average error in strain over entire grains for the CPFE and DIC data. The results are plotted in (a) as a function of basal schmid factor. It is seen that large outliers occur for grains with low basal schmid factor. Grains that have low basal schmid factor are unable to accommodate applied strains due to lack of available slip systems and thus, activate localization modes. The localizations lead

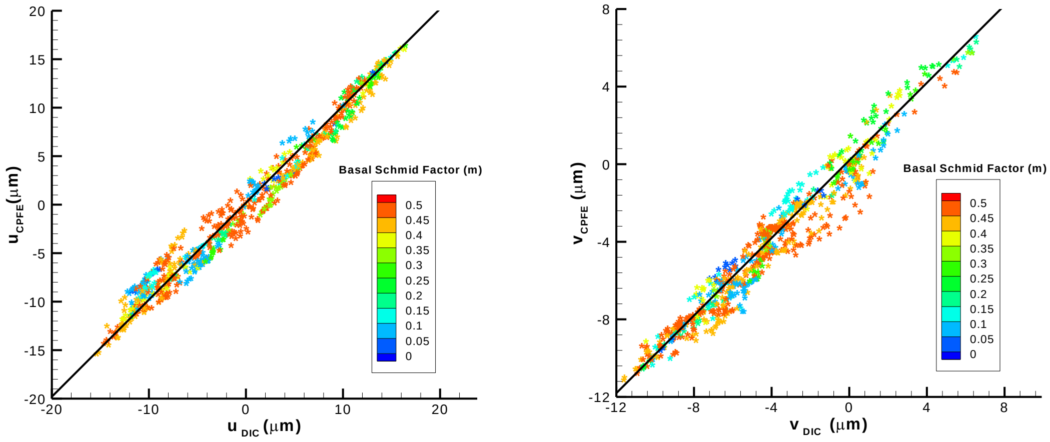

a) b)

Figure 4.2: Comparison of displacement maps for random collection of 800 interior points between CPFE and DIC a) x-displacement b) y-displacement

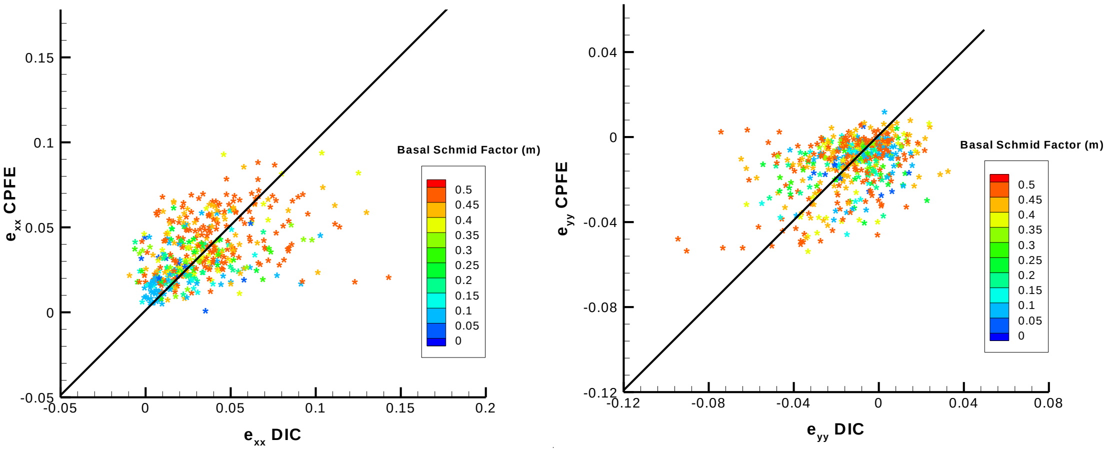

a) b)

Figure 4.3: Comparison of strain maps for random collection of 800 interior points between CPFE and DIC a) E_{xx} b)E_{yy}

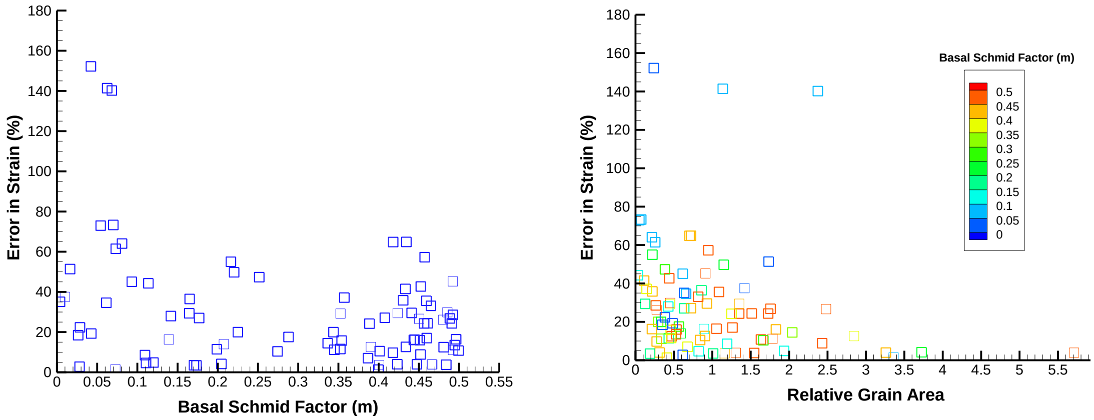

a) b)

Figure 4.4: Error in strain E_{xx} averaged over the entire grain between CPFE and DIC as a function of a) basal schmid factor (m) b) relative grain area

to a tendency for larger errors in the CPFE results. The results are plotted as a function of relative grain size (ie. grain size as compared to the average grain size in the alloy) in Fig. (b). There is a clear tendency for errors to be higher for smaller grains while very large grains (relative grain area greater than 3) have low error (typically less than 5%) in strains. This is due to the fact that these grains can accommodate slip better, and localizations tend to get averaged out over large areas.

Two measured microstructural field of views (FOVs) used for the DIC/CPFE comparison are shown in Fig. 4.5. The basal schmid factor distribution and the orientation distribution (through an inverse pole figure) is shown. To go with our previous analysis of errors in Figs 4.2–4.4, we also indicate the errors in FOV1 for various grains marked A–J in Fig. 4.5(c) in Table. 4.1. The errors in strains are larger for low schmid factor grains (A,C,J, with schmid factor $m < 0.1$) as explained before. However, the error is high in a high schmid factor grain D ($m = 0.4$) due to its small grain size. Table 4.2 shows a similar result for FOV2. Here, the largest errors correspond to the low schmid factor/small grain 'L' and the small grain marked 'O'. These results are summarized in a histogram plot in Fig. 4.6. This shows that

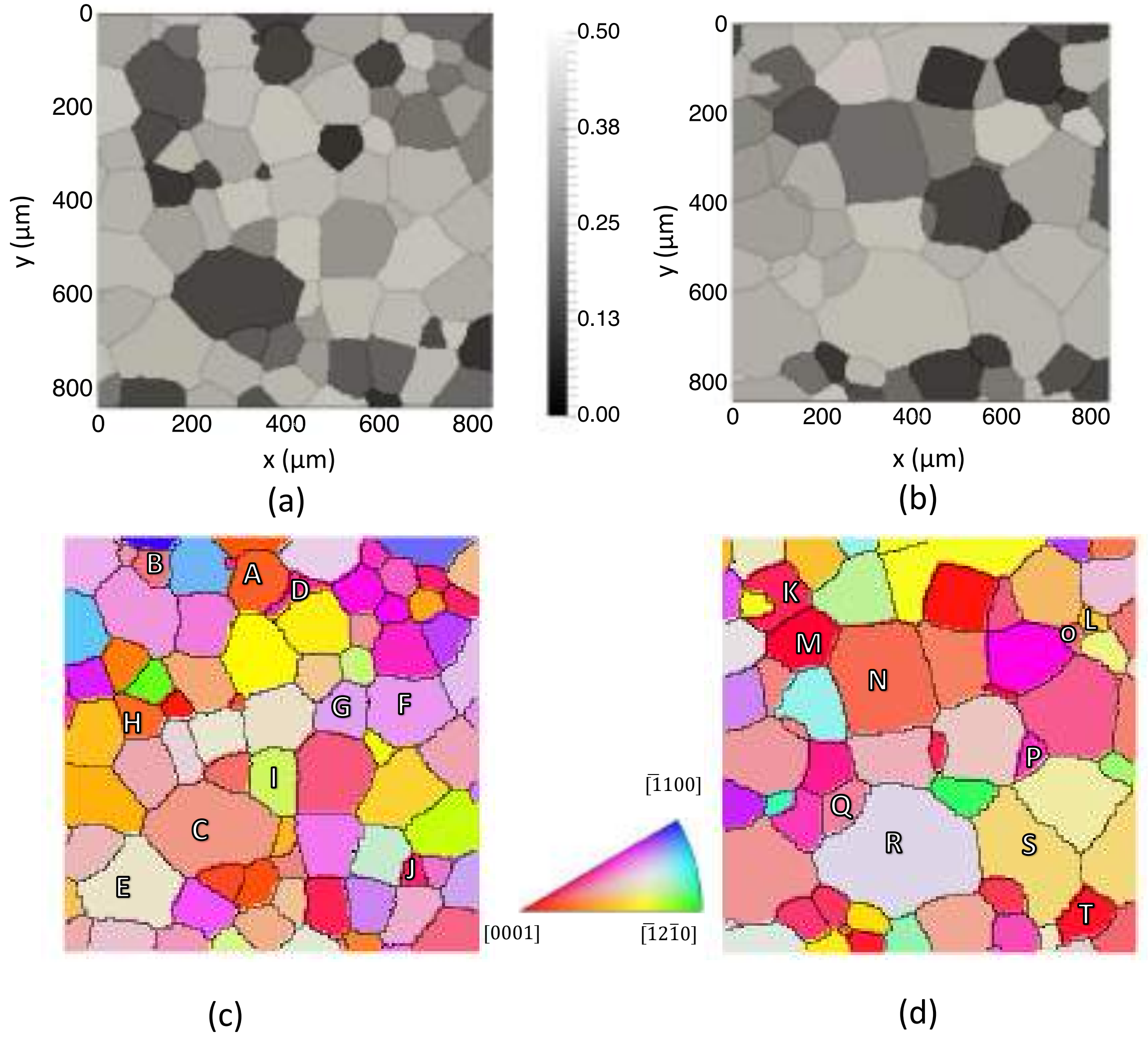

Figure 4.5: Basal schmid factor (m) map for (a) microstructure 1 b) microstructure 2. Corresponding Inverse Pole figure (IPF) maps for (a) microstructure 1 (b) microstructure 2. The individual grains which are studied for both the microstructures are marked.

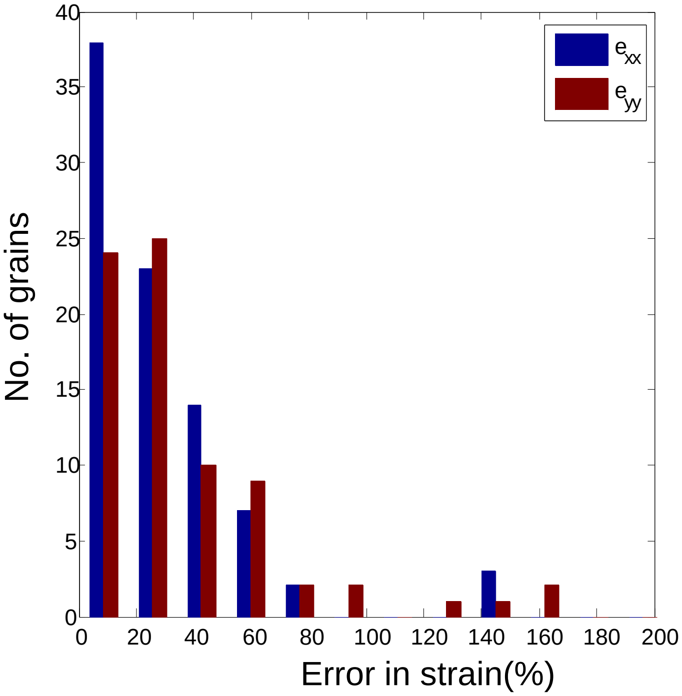

Figure 4.6: Histogram of error in strains averaged over the entire grain between CPFE and DIC

for both x and y strains, the errors are low to moderate (0–30%) for most grains and only a few outliers that correspond to small area or low basal schmid factor grains have high errors.

Compared to T5 results that will be presented in the next chapter, the measurements in T6 alloy were made in a FOV of a larger length scale (800 × 800 micrometer window) and the DIC data is also of a lower resolution. While fine slip traces are not seen at this resolution, the large scale localizations are clearly seen in Fig. 4.7(a,c,e). A direct comparison of these strain maps with the CPFE results are shown in Fig. 4.7(b,d,f) for FOV1. These results are a strain level of 3.23%. Although the localizations are not reproduced, CPFE does indeed give good reproduction of average strains in several grains with best matches seen in large grains. A similar comparison for FOV2 is shown in Fig. 4.8.

For a closer comparison of strains, we extract small windows around the large grain in the FOV to identify how the displacements and strains of CPFE and DIC are correlated. One such window from FOV1 is shown in Fig. 4.9(a,d). The displacement contours have several plasticity–related features that can be observed by comparing against a model where plasticity is switched off (ie. a crystal elasticity model). The crystal elasticity model is obtained by switching off the active slip search. In this model, the displacements are fully elastic and no slip systems are active. As seen from the Fig. 4.9(c,f) the results do not reproduce the complexities of the displacement distribution in the DIC maps of Fig. 4.9(a,d). Such features include non–accommodation of strains in low-Schmid factor grains and heterogeneity of slip in large grains. These features are better captured when plasticity is taken into account in Fig. 4.9(b,e). Fig. 4.10 shows a similar observation for FOV2. Here, the shear localization pattern in Fig. 4.10(a,b) to the right of the large grain in the center can only be captured if plasticity is included.

Finally, we also show the strain comparisons over different strain levels in FOV1

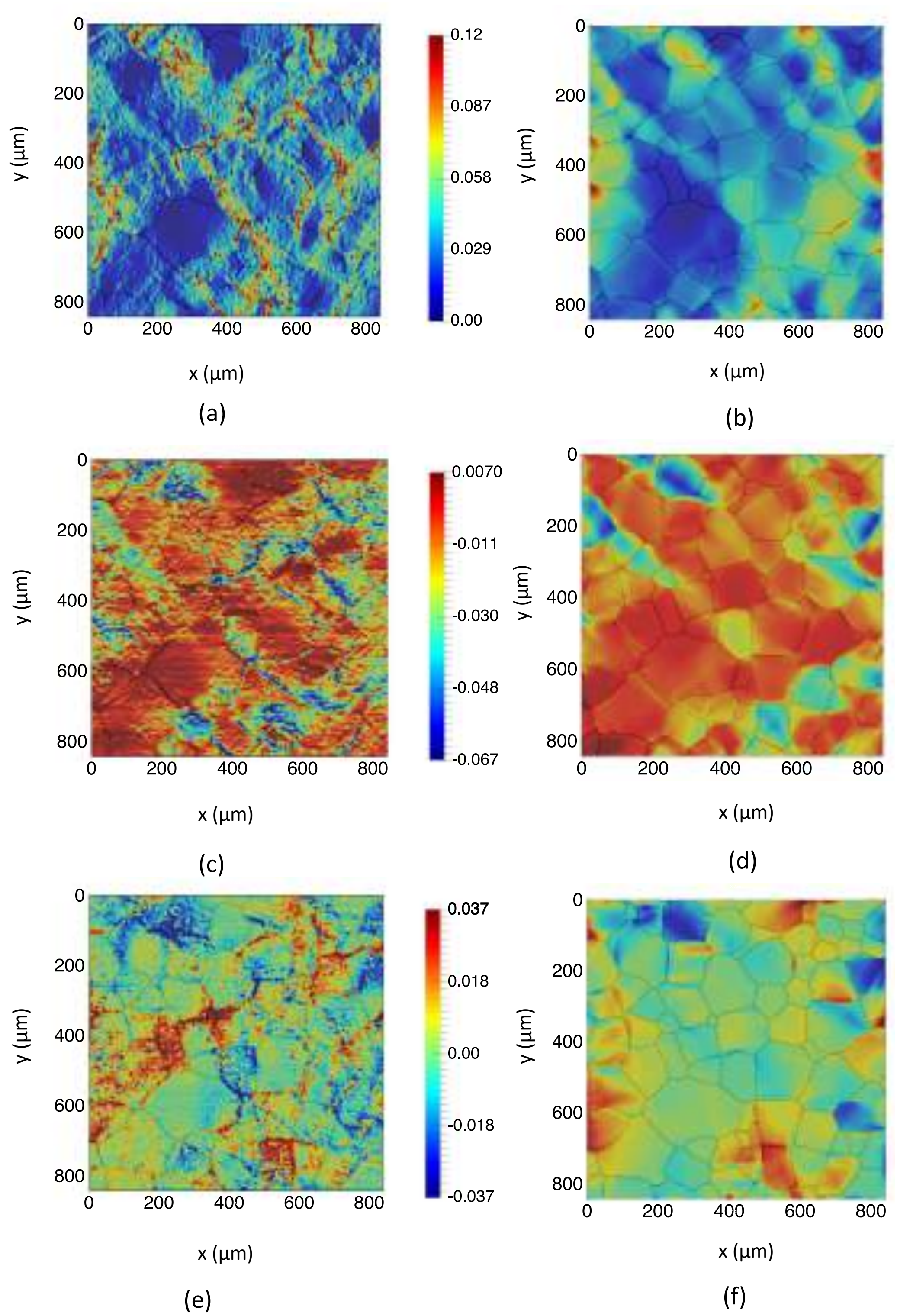

Figure 4.7: Comparison of strain maps between SEM-DIC experiments and CPFE simulations at 3.23% strain in x-direction for microstructure 1(a) E$_{xx}$ DIC (b) E$_{xx}$ CPFE (c) E$_{yy}$ DIC (d) E$_{yy}$ CPFE (e) E$_{xy}$ DIC (f) E$_{xy}$ CPFE

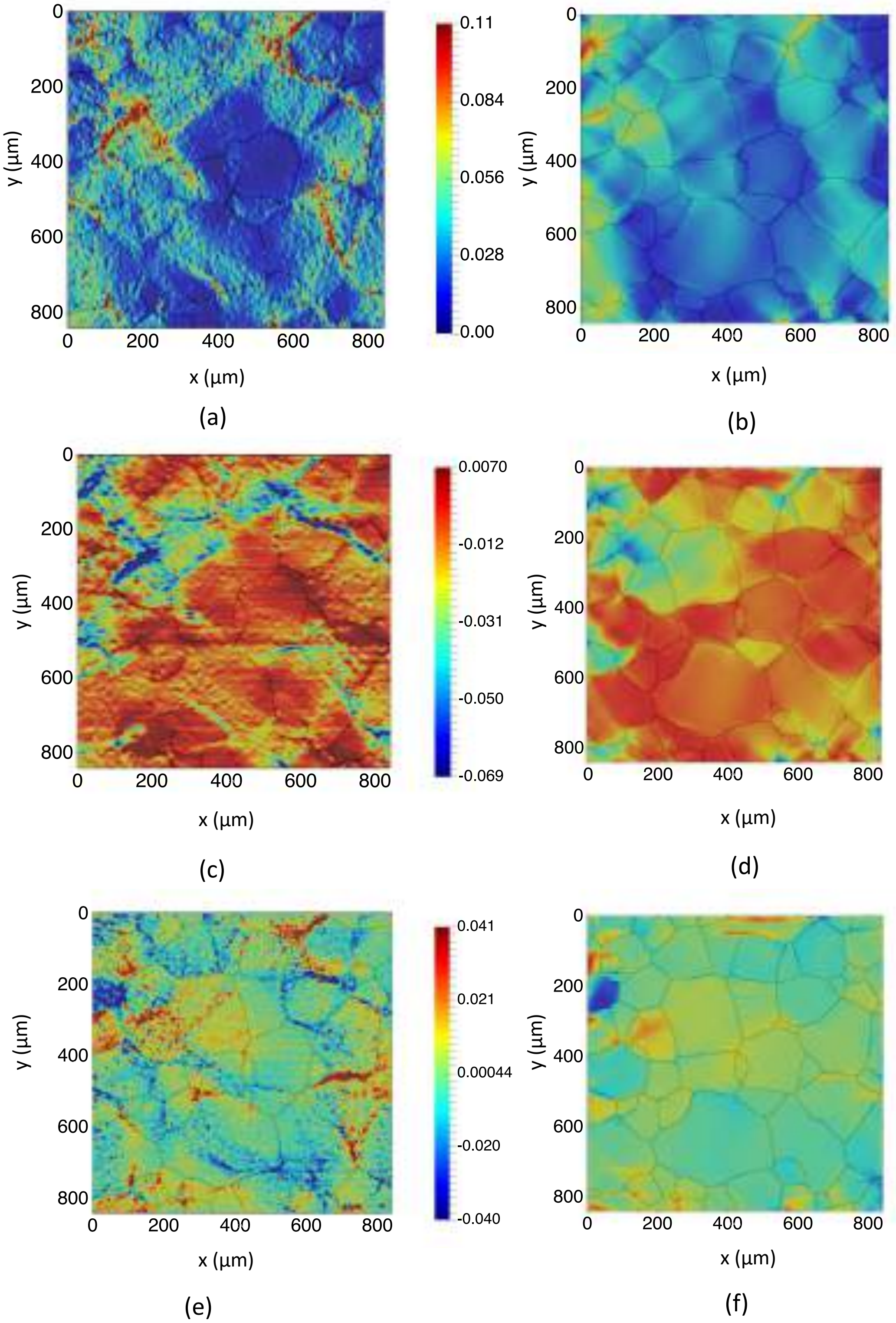

(a)

(b)

(c)

(d)

(e)

(f)

Figure 4.8: Comparison of strain maps between SEM-DIC experiments and CPFE simulations at 3.23% strain in x-direction for microstructure 2(a) E$_{xx}$ DIC (b) E$_{xx}$ CPFE (c) E$_{yy}$ DIC (d) E$_{yy}$ CPFE (e) E$_{xy}$ DIC (f) E$_{xy}$ CPFE

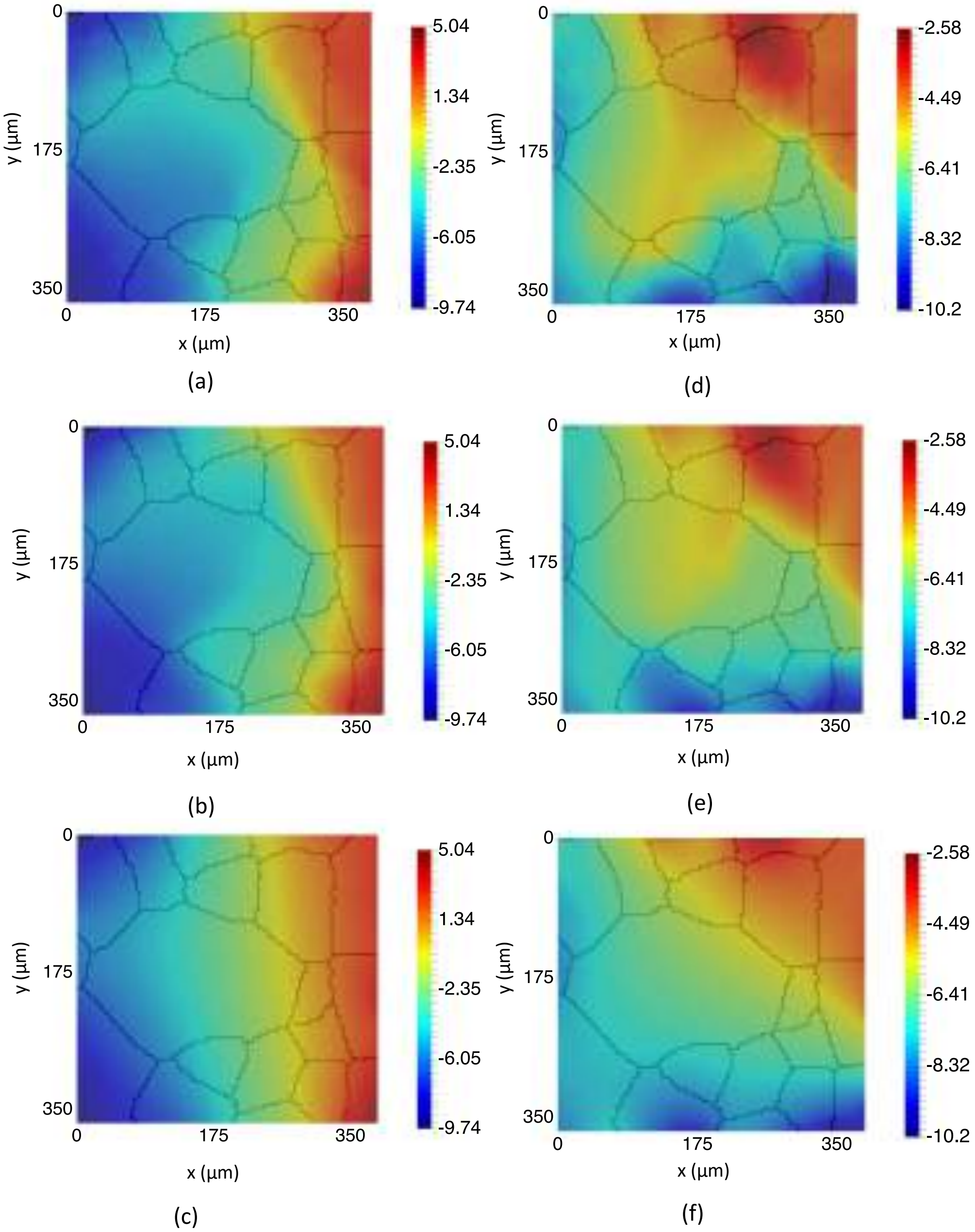

Figure 4.9: Comparison of displacement maps between SEM-DIC experiments , CPFE and crystal elasticity simulations at 3.23% strain in x-direction (a) x-displacement DIC (b) x-displacement CPFE (c) x-displacement crystal elasticity (d) y-displacement DIC (e) y-displacement CPFE (f) y-displacement crystal elasticity

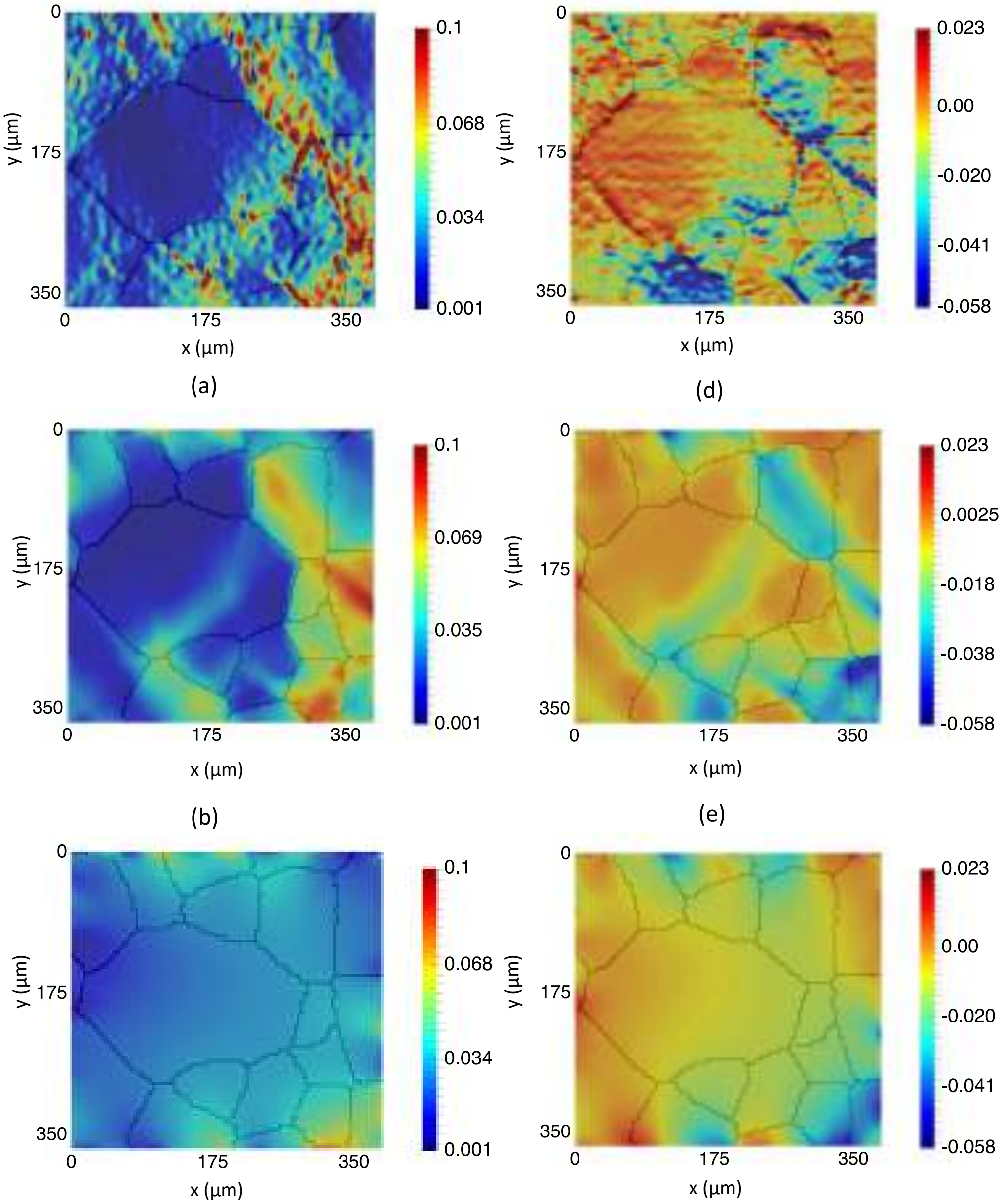

(a) (d)

(b) (e)

(c) (f)

Figure 4.10: Comparison of strain maps between SEM-DIC experiments , CPFE and crystal elasticity simulations at 3.23% strain in x-direction (a) E_{xx} DIC (b) E_{xx} CPFE (c) E_{xx} crystal elasticity (d) E_{yy} DIC (e) E_{yy} CPFE (f) E_{yy} crystal elasticity

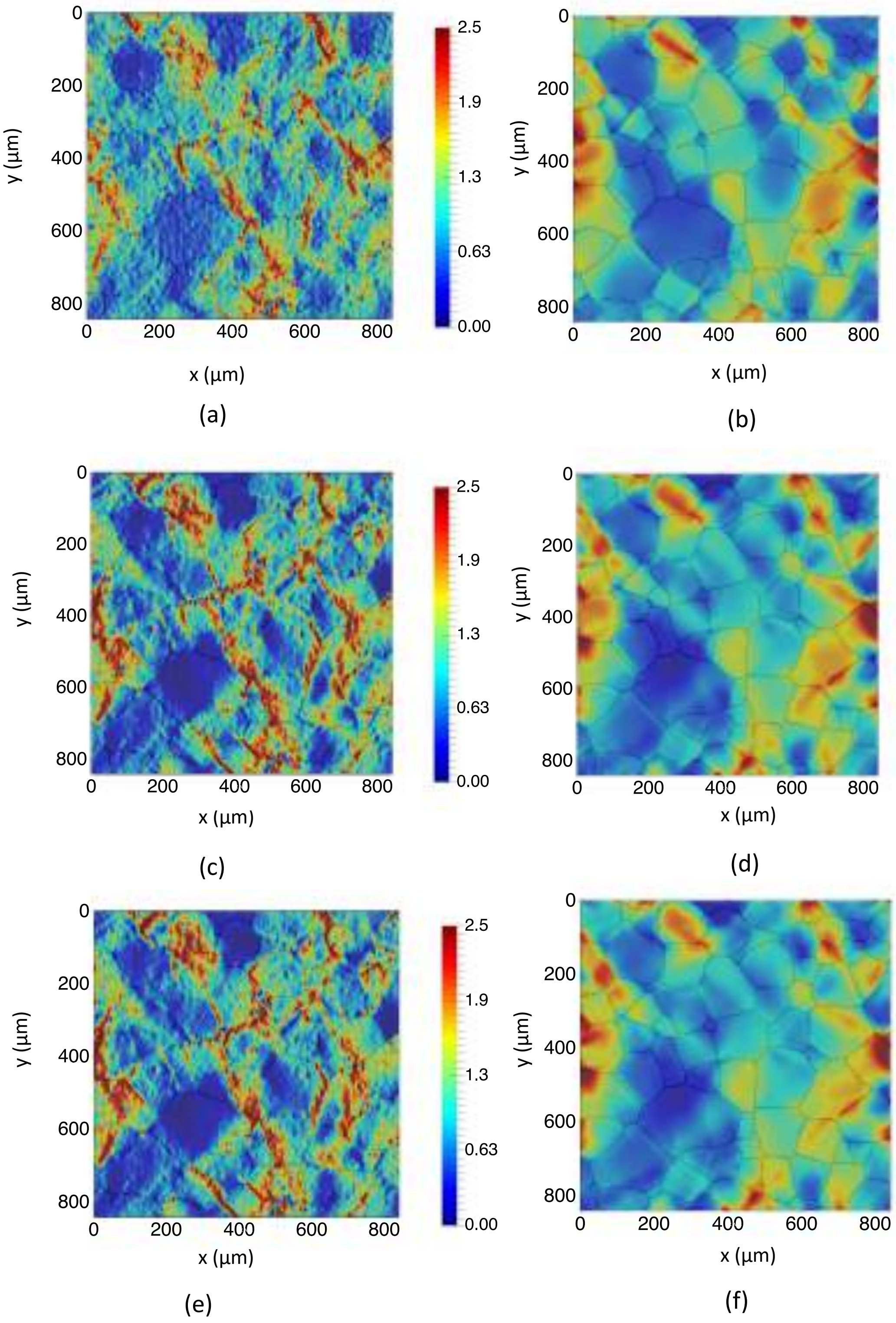

Figure 4.11: Comparison of relative strain maps between SEM-DIC experiments and CPFE simulations for E_{xx} at different strains (a) 0.76% strain DIC (b)0.76% strain CPFE (c) 4.83% strain DIC (d) 4.83% strainCPFE (e) 8.15% strain DIC (f) 8.15% strain CPFE

Table 4.1: Strain comparisons of individual grains in WE43 T6 FOV1

ID	**m**	$\mathbf{E_{xx}}$**(DIC)**	$\mathbf{E_{xx}}$**(CPFE)**	$\mathbf{E_{yy}}$**(DIC)**	$\mathbf{E_{yy}}$**(CPFE)**	$\mathbf{e_{E_{xx}}}$%	$\mathbf{e_{E_{yy}}}$%
A	0.06	0.009	0.022	-0.001	-0.016	141.4	1363.9
B	0.20	0.041	0.036	-0.023	-0.023	11.5	1.2
C	0.07	0.014	0.015	-0.002	-0.008	1.5	236.2
D	0.40	0.030	0.030	0.005	-0.006	1.4	223.0
E	0.45	0.018	0.019	-0.003	-0.004	8.9	27.1
F	0.44	0.040	0.047	-0.025	-0.025	16.1	2.8
G	0.44	0.037	0.026	-0.009	-0.009	29.5	0.6
H	0.03	0.022	0.023	-0.014	-0.016	2.8	12.9
I	0.50	0.051	0.042	-0.018	-0.018	16.4	1.4
J	0.08	0.022	0.036	-0.027	-0.027	64.1	0.1

in Fig. 4.11. The strain levels are 0.76% in (a), 4.83% in (c), and 8.15% in (e). The observation is that the localization pattern only intensifies as strain increases and does not change grain–wise (at least up to a strain of 8.15%). A similar trend is seen with the CPFE results in Fig. 4.11(b,d,f) corresponding to these increasing strain levels.

Table 4.2: Strain comparisons of individual grains in WE43 T6 FOV2

ID	**m**	$\mathbf{E_{xx}}$**(DIC)**	$\mathbf{E_{xx}}$**(CPFE)**	$\mathbf{E_{yy}}$**(DIC)**	$\mathbf{E_{yy}}$**(CPFE)**	$\mathbf{e_{E_{xx}}}$%	$\mathbf{e_{E_{yy}}}$%
K	0.17	0.043	0.041	-0.024	-0.034	3.5	39.6
L	0.04	0.008	0.020	-0.009	-0.010	152.2	9.4
M	0.11	0.044	0.040	-0.032	-0.035	8.6	9.0
N	0.20	0.033	0.032	-0.023	-0.025	4.2	6.4
O	0.17	0.028	0.027	-0.034	-0.013	3.5	61.2
P	0.03	0.017	0.020	-0.008	-0.008	18.5	0.4
Q	0.41	0.037	0.027	-0.006	-0.006	27.1	1.2
R	0.47	0.024	0.025	-0.008	-0.010	4.0	12.5
S	0.45	0.028	0.029	-0.010	-0.014	4.0	34.2
T	0.44	0.038	0.039	-0.018	-0.018	3.8	1.1

CHAPTER V

Crystal plasticity simulations for WE43-T5 alloy and validation of slip and twin activity using SEM-DIC Experiments

5.1 Introduction

In this chapter, the SEM-DIC results [46] for WE43 T5 temper are compared against crystal plasticity finite element (CPFE) simulations in order to test the CPFE model against DIC data, identify Schmid factor variations due to the effects of neighbor grains, and to computationally differentiate the slip traces observed in the DIC data into various slip and twin systems. All the experimental SEM-DIC data was received from Prof. Daly's group [46]. The results are discussed in the following section.

5.2 Results

The BVP is set up for WE43 T5 temper similar to WE43 T6 temper as described in the previous chapter. A single layer of elements was assumed in the z-direction with a 150x150 mesh. The CPFE predictions of the x-strains in a tension test are plotted alongside the DIC strain map in Fig 5.1. A direct comparison reveals that overall strain distribution was captured reasonably well in the CPFE simulations, with grains with low strains (A,B,E,J) correctly predicted. Strains in grains with moderate strain (C,F,I,D) were also well predicted. There are a few discrepancies. A region in the DIC image has high strains (G) and corresponds to a cluster of small grains. This could arise due to Hall-Petch or grain boundary accommodation, neither of which are included in the FEM simulation. The strains in that region are lower in the CPFE simulation, and the grains surrounding that region take up more strains (K,H) to achieve overall equilibrium. There are a small number of grains where strains are not well predicted, such as M and L. Note that we have made no attempt to calibrate the CPFE model based on the DIC strain maps, but rather the CPFE model parameters were calibrated based on the macroscopic stress-strain response. In this light, the DIC strain maps predicted by CPFE are encouraging. Also, CPFE does not predict the shear localizations that are seen in the DIC maps. These fine slip bands occur naturally in experiments while special techniques (bifurcation analysis [41]) are needed in CPFE to capture such phenomena.

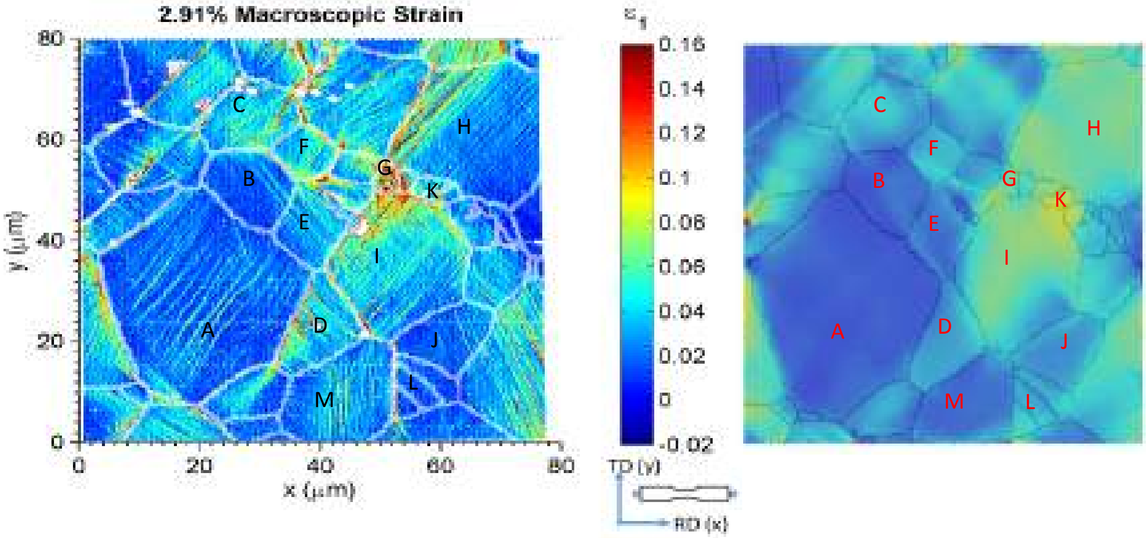

Figure 5.1: Comparison of x-strain from SEM-DIC (left) and CPFE (right) model during tension test at 2.91% strain

A comparison for the case of compression, where significantly more twinning is observed, is shown in Fig 5.2. A direct comparison of the strain map is shown in Figure 5.2 (a,b) at an applied strain of 4.2%. As is the case of tension test, the overall strain prediction is satisfactory, while fine strain localizations are not captured. We primarily focus on the twinning process during compression. Fig 5.2(c) shows the twin activity in various grains. During compression, we observe that the deformation is accommodated by recovering pre-existing twins (in the form of detwinning) as seen from the inverse pole figures in (d,e). Due to this effect, compressive deformation yields at lower stress as compared to the tensile deformation (as seen from stress-strain curve in Fig. 3.8 and early twin activity in Fig. 3.11 during compression).

In the following, we compare the slip systems predicted by CPFE against the DIC traces to further validate the model. We primarily focus on the tension test results in Fig 5.1.

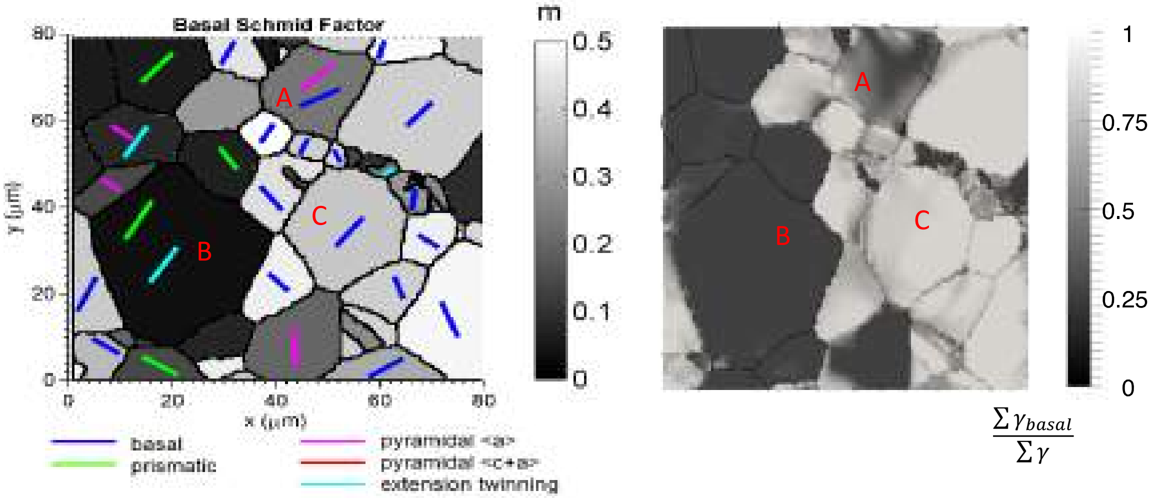

Figure 5.3: (left) DIC traces that are identified are shown superposed on the basal Schmid factor. (right) the CPFE prediction of the relative activity of basal slip is shown.

The CPFE model can be used to identify non-Schmid effects that arise due to the strain accommodation by neighboring grains to maintain overall equilibrium. In Fig 5.3a, the DIC traces that are identified are shown superposed on the basal Schmid factor. In Fig 5.3b, the CPFE prediction of the relative activity of basal slip is shown.

The relative activity shows the fraction of the total plastic shear carried by the three basal slip systems. In all the grains with high basal activity predicted by the CPFE model (eg. grain marked C), basal traces are observed in experiment. The darker regions correspond to regions of relatively low basal activity. These regions in Fig 5.3b (eg. grain marked B) correspond well to regions with low Schmid factor in Fig 5.3a. In such grains, other slip systems (mainly prismatic and pyramidal$_{<a>}$ slip) are active as seen from the traces shown in Fig 5.3a. Non-Schmid effects arise in some grains that show regions of both high and low basal activity. One example is grain marked A in the images. In this grain, some parts of the grain deform predominantly by basal slip while others by pyramidal$_{<a>}$ as indicated in the DIC trace analysis.

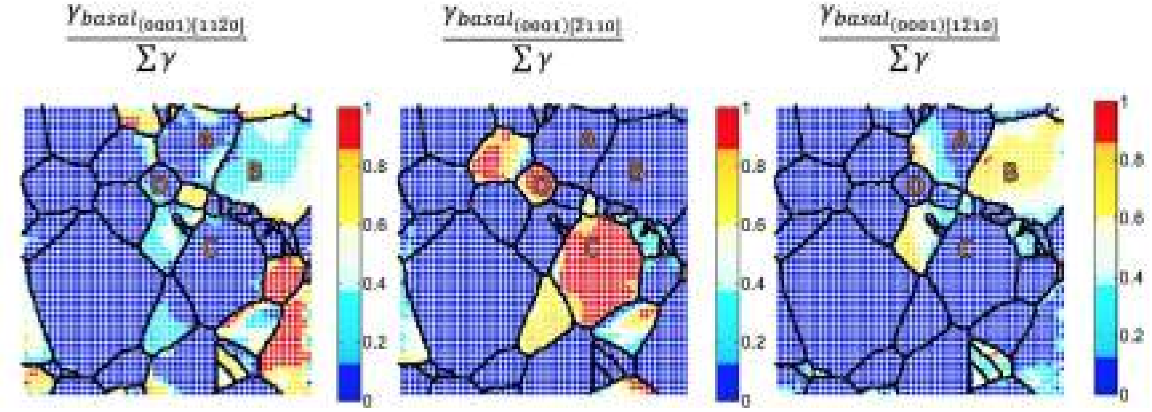

Figure 5.4: The relative activity of the three basal slip systems are compared using quadrature point data from CPFE model.

CPFE simulations can be used to differentiate between the three types of basal slip systems that correspond to the same basal slip trace. In Figure 5.4, the relative activity of the three basal slip systems are compared using quadrature point data. In some grains, two basal slip systems are simultaneously active (grain marked B). In the grain marked A, some parts of the grain have slip system 1 active, while others have slip system 3 active. Most other grains have only one basal system active (eg. grains marked C,D) during early deformation.

In Fig 5.5, grains with non basal slip traces from the SEM-DIC data are compared

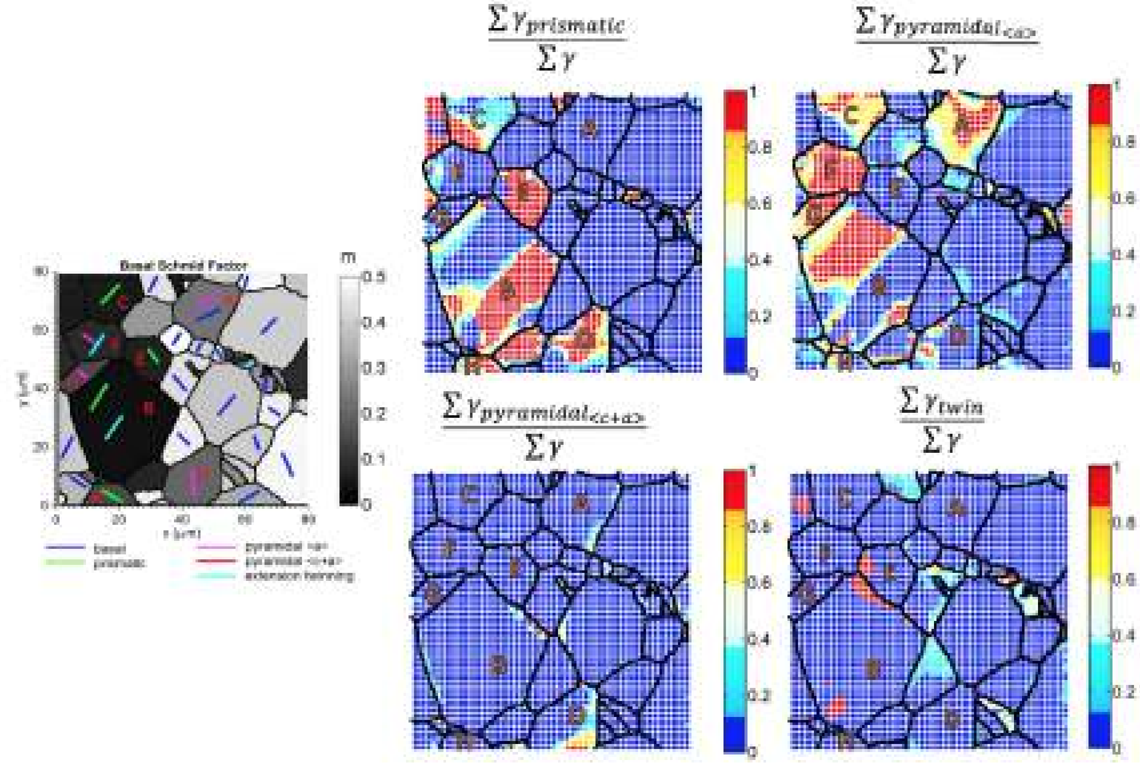
$\frac{\sum \gamma_{prismatic}}{\sum \gamma}$

$\frac{\sum \gamma_{pyramidal_{<a>}}}{\sum \gamma}$

$\frac{\sum \gamma_{pyramidal_{<c+a>}}}{\sum \gamma}$

$\frac{\sum \gamma_{twin}}{\sum \gamma}$

Figure 5.5: Slip traces from the SEM-DIC data are compared against the slip activity for grains that deform through a non-basal mechanism as predicted from CPFE

against the slip activity predicted from CPFE. Grains with prismatic activity as predicted from CPFE include all grains except grains A and G. In the CPFE result, grain B, C, D and H show both prismatic and pyramidal$_{<a>}$ activity, some twin activity is seen in grain E. Grains F, G and A show pyramidal$_{<a>}$ activity in the CPFE model and is confirmed with the DIC slip traces. Note that pyramidal$_{<a>}$ has often not been used in Mg alloy models [23, 90], but from the simulations as well as experiments, these slip systems play a role in deformation. Some grains have multiple slip systems active as seen from CPFE. For example, grain A has both basal (as seen in Fig 5.4) and pyramidal$_{<a>}$ active and is confirmed with the slip trace analysis.

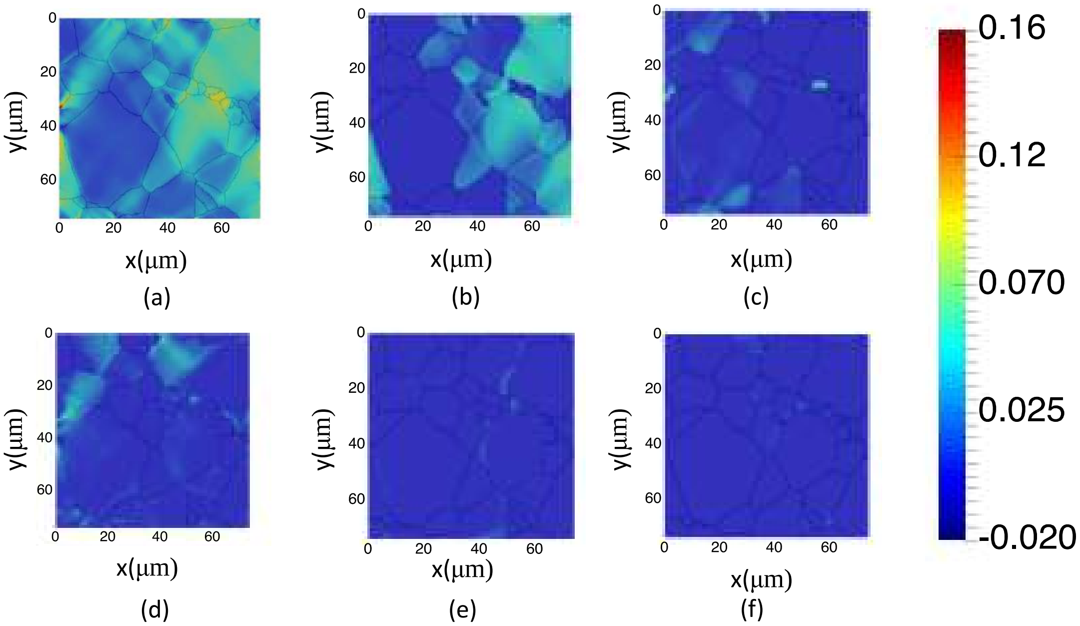

Figure 5.6: Axial Strain E$_{xx}$ in (a) is decomposed into sum of contributions from the individual slip systems (b) basal (c) prismatic (d) pyramidal$_{<a>}$ (e) pyramidal$_{<c+a>}$ and (f) twin

Some discrepancies are seen in the CPFE model. Grain B and F shows traces that correspond to extension twinning. However, grain F shows no twinning in CPFE (rather prismatic slip additionally is seen). Likewise, grain B shows pyramidal$_{<a>}$ slip activity instead of extension twinning predicted by DIC. The angle difference be-

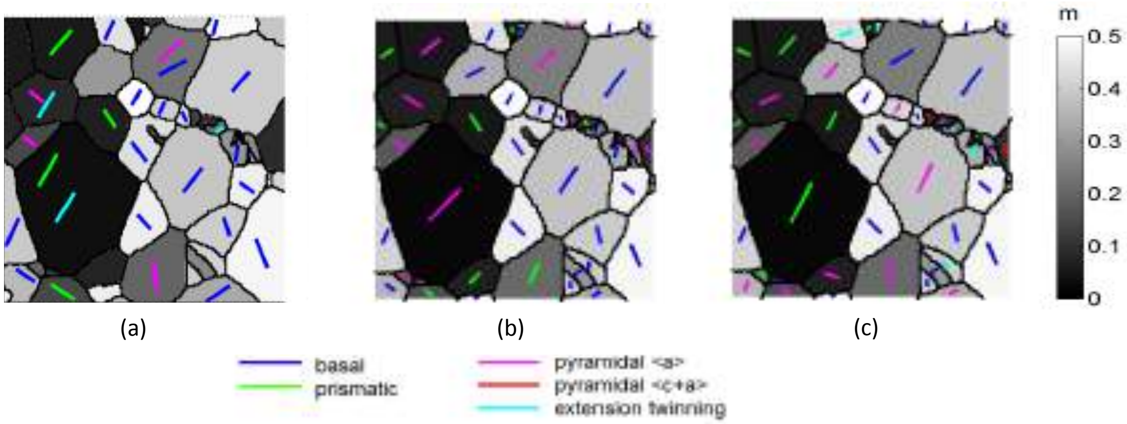

(a) (b) (c)

Figure 5.7: Slip traces from the SEM-DIC data (a) are compared with the first predominant slip trace (b) and second predominant slip trace (c) in the CPFE-DIC simulations

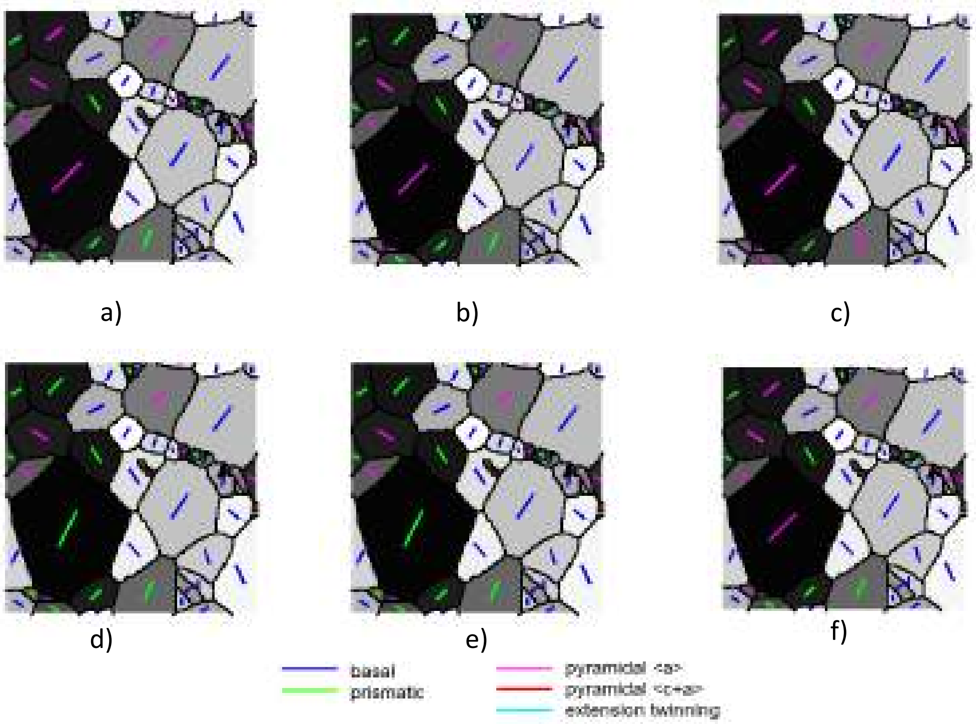

a) b) c)

d) e) f)

Figure 5.8: Predominant slip trace from CPFE simulations for sensitivity analysis a) Baseline b) Case 1 c) Case 2 d) Case 3 e) Case 4 f) Case 5

tween the trace for extension twinning in grains B predicted by DIC and pyramidal$_{<a>}$ system predicted by CPFE is only 5.9 degrees. This small difference is nearly indistinguishable in experimental measurements. CPFE could thus be used to correctly classify the traces observed in the DIC data. If a grain deforms via basal slip, strain accommodation in the neighboring grains may necessitate the activation of non-basal systems. The fact that multiple slip systems can be active within a grain (eg. grain B) and slip activity of a system can be localized within a grain to one side (Fig 4C of DIC, or prismatic slip in grain E in Fig. 5.5 demonstrated that significant deviations can occur in grain to grain strains. It was found in [68] that strain accommodation in neighboring grains played a key role in twinning variant selection and justified deviations from Schmid behavior during compressive loading of AM30 and AZ31 alloys. It may also be a reason that the macroscopic loading may dictate the activation of basal slip, and the deforming basal slip systems subsequently dictate the activation of non-basal and other basal systems. Fig. 5.6 shows the absolute strain due to the combination of slip systems. It can be used along with Fig. 5.5 to measure the intensity of strains due to slip systems in case of grains with multiple slip activity. Fig. 5.7 a) shows the slip traces from SEM-DIC data and they can be compared with the first predominant trace obtained from the CPFE simulations in Fig. 5.7 b) and second predominant trace in Fig. 5.6 c). They confirm the deviations observed from Fig. 5.5. A sensitivity study was conducted by varying the CRSS values of the slip systems by 5 %. The CRSS values of individual cases which were studied are tabulated in Table 5.1. The predominant traces are compared with the baseline CRSS values in Fig. 5.8. Trace error, which is defined as the percentage difference between the predominant traces obtained from SEM-DIC and predominant traces obtained from CPFE simulations are tabulated in Table 5.1. Case 3, which has pyramidal$_{<a>}$ CRSS greater than prismatic CRSS shows the closest match to the DIC data. This shows that pyramidal$_{<a>}$ slip systems are sensitive to the computation of slip activity in this particular alloy.

Table 5.1: Sensitivity study of slip activity with respect to CRSS values

	Baseline	**Case 1**	**Case 2**	**Case 3**	**Case 4**	**Case 5**
Basal<a> CRSS (MPa)	76.0	79.8	76.0	76.0	76.0	76.0
Prism<a> CRSS (MPa)	163.2	163.2	171.4	163.2	163.2	163.2
Pyram<a> CRSS (MPa)	160.3	160.3	160.3	168.3	160.3	160.3
Pyram<c+a> CRSS (MPa)	187.4	187.4	187.4	187.4	196.8	187.4
Twin<c+a> CRSS (MPa)	116.4	116.4	116.4	116.4	116.4	122.2
Trace error(%)	84.6	84.6	84.6	92.3	84.6	84.6

5.3 Conclusions

Full-field plastic strains were characterized for the magnesium alloy WE43 in a hot rolled plate in the T5 heat treatment condition. Due to the high resolution possible with in-situ SEM imaging combined with digital image correlation, the quantified strain from individual slip traces was measured for the first time in magnesium. This data can serve as powerful verification for crystal plasticity modeling. The quantification of strain allowed for the following insights on the deformation mechanisms responsible during plastic deformation. The DIC results were compared against crystal plasticity finite element (CPFE) simulations and the strain distribution is captured reasonably well by the model. The CPFE model is able to identify Schmid factor variations due to the effect of neighbor grains in the form of relative slip activity, and thus computationally differentiate the slip traces observed in the DIC data into various slip and twin systems. Therefore, the DIC experiments validate the crystal plasticity model that in turn helps in identifying the slip traces. This combined framework provides a powerful tool to accelerate alloy development and process design and optimization.

CHAPTER VI

Generalized inverse voronoi approach for reconstructing 3D convex microstructures from surface EBSD map

3D reconstruction of microstructures is growing to be an important topic of interest in the field of materials modeling and simulation. In the case of surface experimental measurements such as digital image correlation, it is important to know the subsurface effects to interpret the surface observations better. However, subsurface data is expensive to obtain (ex. through 3D tomography [42, 74, 121] or serial sectioning [38]). It is of interest to generate these computationally. There are methods available to reconstruct microstructures based on feature matching using correlation functions or using Markov Random Fields [99, 118, 95, 62, 3]. However, a method to reconstruct the 3D structure while retaining the measured 2D surface image has not yet been developed. In this work, we use a generalized inverse voronoi problem approach to construct an approximate voronoi representation of the 3D microstructure given the 2D surface image. We use sections of a large Electron Back Scatter Diffraction (EBSD) observation and use their centroids as voronoi generators and stack up layers below the top layer to construct a 3D microstructure. Recrystallized microstructures are regular shaped and are almost convex in their topology. The microstructures may be non-convex when using surface grains as generator points. In this chapter, we develop an algorithm to convexify the stack to recover the 3D topology. Comparisons are made with surface DIC measurements for random samples of 3D microstructures as compared to columnar 2D microstructures. Extension of this theory to non-convex microstructures is discussed.

6.1 Introduction

Voronoi diagram is a popular tool used to construct virtual microstructures [82, 118]. Voronoi tessellation and its dual, delaunay triangulation are commonly used to describe observed structures in crystallography. Voronoi tessellation is also called as the Dirichlet tessellation or Thiessen tessellation [110, 116]. A historical perspective of the development of Voronoi diagrams and delaunay triangulation, including applications in crystallography and recent applications in a wide variety of fields is provided in [76].

Given the generator points, the voronoi polygons can be constructed using the algorithms in [25, 40]. In 2D, Voronoi diagram is a case of a Planar Straight Line Graph (PSLG) where each polygon belongs to a generator point and consists of all points in the plane that are closer to the generator point as compared to any other generator point in the plane.

The problem of obtaining the generator points from the Voronoi tessellation, called the Inverse Voronoi Problem (IVP) has been well studied in [13, 14, 40, 56, 85]. Inverse voronoi problem is limited to finding one generator point for a polygon, a generalized version of the problem, called Generalized Inverse Voronoi Problem (GIVP) was defined in [113] and [10]. Here, each voronoi polygon can be represented by multiple generator points. The properties of a GIVP for a rectangular tessellation is studied in [16] and an algorithm to find the minimal number of generator points is described.

A measure for concavity or convexity of the grain, PARIS factor was introduced in [78]. The area difference ratio between the original shape and its convex envelope has been captured by a descriptor deltA [58] for analyzing faults in rocks.

Kinematic measurements at the microstructural scale have been performed using an Atomic Force Microscopy (AFM) [88] or Scanning Electron Microscope (SEM) [107, 106]. These imaging methods allow for the mapping of strain fields at the surface of polycrystals with high spatial resolutions [107, 106]. For more accurate comparison with such experimental results, 3D finite element modeling has been employed by using columnar grains [22, 80] or by interpolating the grain shape from intersection with other free surfaces[37, 109].

A framework for simulating 3D microstructural models was developed using an integrated experimental-computational approach using a process called statistically induced realistic instantiations [48, 49] . In [26], the grains were approximated as a set of optimally packed ellipsoids and the 3D microstructure is obtained by transferring the grain structure to a voronoi tessellation. Morphological models were developed for 3D concrete microstructures using multiscale Poisson polyhedra in [39].

A computational and statistical approach was applied in [119, 120] to predict the surface stress-strain for a given 2D grain morphology when the underlying 3D microstructure is changed. In this approach, the first layer of 3D grains beginning from the constrained surface is obtained by expanding or eroding each grain by a random process. It is followed by generating random seeds for producing a Voronoi tessellation for the remaining image. However, these methods do not generate realistic 3D structures, often concave grains are obtained.

In this work, the microstructures were constructed from a surface map by convexification followed by a unique approach to construct inverse voronoi diagram using sentinel points. Then, a large surface EBSD map of the same microstructure is used to create voronoi generators in the normal direction to generate the 3D microstructure. Convexification of the 3D microstructure is carried out to obtain back the surface microstructure. To the knowledge of the authors, no such equivalent algorithm is available in literature.

The chapter is organized as follows : In section 6.2, we describe the theory of voronoi diagrams followed by the methodology to construct 3-D microstructures in sections 6.2.1 -6.2.4. In section 6.3, we discuss the implementation of the algorithm for a real microstructure and also give an overview of the Digital Image Correlation experiment and comparison with crystal plasticity finite element method. In section 6.4, we present the results of comparison between simulations of 3-d microstructures as compared to columnar microstructures. In section 6.5, we present the conclusions of the study and discuss some possible extensions of the study.

6.2 Theory

We begin with formally defining Voronoi tessellation and the generator points following the notation used in [108].

Let P(x) denote a point in the N-dimensional Euclidean space R^N , where x is an N-dimensional vector $(x^1, x^2, ..., x^N)$. For n distinct points $P_1(x_1), P_2(x_2), ..., P_n(x_n)$ given in R^N.

$$Q_i = \bigcap_{j:j\neq i} \{x \in R^N \mid \|x - x_i\| < \|x - x_j\|\} \tag{6.1}$$

is the set of points in R^N which are closer to $P_i(x_i)$ than to any other $P_j(x_j)$ $j \neq i$ where $\|.\|$ denotes the Euclidean distance. This partition as shown in Fig. 6.1 is called as the Voronoi diagram for the given n points $P_i(x_i)'s$.

Each polygon in the tessellation contains points that are closer to its center as compared to the center of any other polygon. The problem of detecting Voronoi polygons is equivalent to finding Voronoi centers if they exist. If Voronoi centers do not exist (i.e., the polygons are not Voronoi polygons), the points that best approximate Voronoi centers will be useful to find[40].

Two corollaries follow from (6.1):

Corollary 1. Voronoi polygons are convex

Corollary 2. The line segment joining centers of adjacent polygons is perpendicularly bisected by the edge common to both polygons [47].

The generators can be obtained from the Voronoi diagram in the 2-dimensional case by a purely geomterical method. This is based on the property of the Voronoi diagram. In Fig. 6.1 P_1, P_2, and P_3 are generators, V_1 is a Voronoi point which is the circumcenter of the triangle $\Delta P_1 P_2 P_3, V_2, V_3$ and V_4 are the neighboring Voronoi points. Let

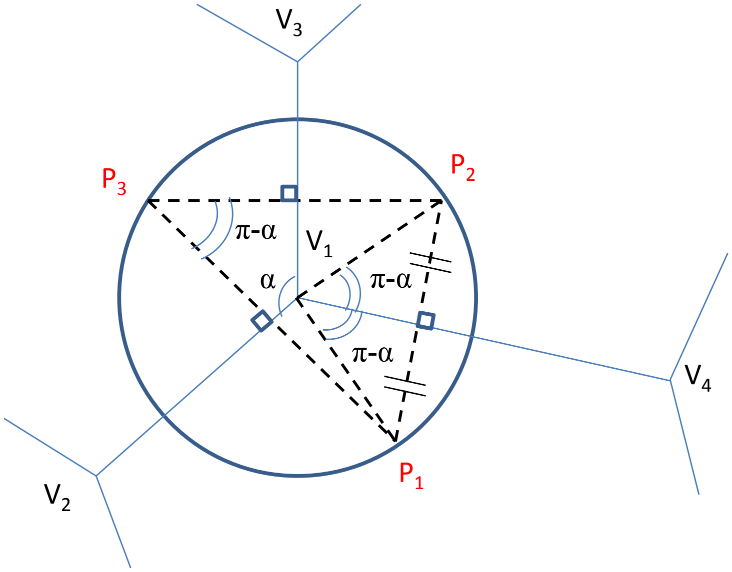

Figure 6.1: Voronoi Diagram with the generators and voronoi points

$$\angle V_2V_1V_3 = \alpha \tag{6.2}$$

$$\Rightarrow \angle P_1P_3P_2 = \pi - \alpha \tag{6.3}$$

From the inscribed angle theorem, the angle formed at the centre of the circle by lines originating from two points on the circle's circumference is double the angle formed on the circumference of the circle by lines originating from the same points. Therefore,

$$\angle P_1V_1P_2 = 2(\pi - \alpha) \tag{6.4}$$

$$\Rightarrow \angle P_1V_1V_4 = \angle P_2V_1V_4 = \pi - \alpha \tag{6.5}$$

Therefore, if we are given an exact Voronoi diagram, a generator can be determined as the intersection of rays such as r_1 and r_2 in Fig. 6.2 emanating from the endpoints of a Voronoi edge, for example, V_1 and V_4. Once the generator P_1 of a Voronoi region G_1 is obtained, we can get the generators of the Voronoi regions which share a Voronoi edge in common with G_1 as the mirror images of P_1 with respect to the Voronoi edges bounding V_1. Furthermore, it is proved in [14] that a proper convex plane tessellation, all of whose vertices have degree 3, is a Voronoi diagram if and only if all such rays as r_1, r_2 and r_3 shown in Fig. 6.2 have a point in common for each region.

6.2.1 2-D Convex Microstructure

During recrystallization process, the cells grow in space leading to near-convex microstructures. The microstructures that were used in this study underwent dynamic recrystallization due to hot rolling resulting in fairly equiaxed microstructures [46]. Recrystallized microstructures grow from a nuclei and result in almost convex

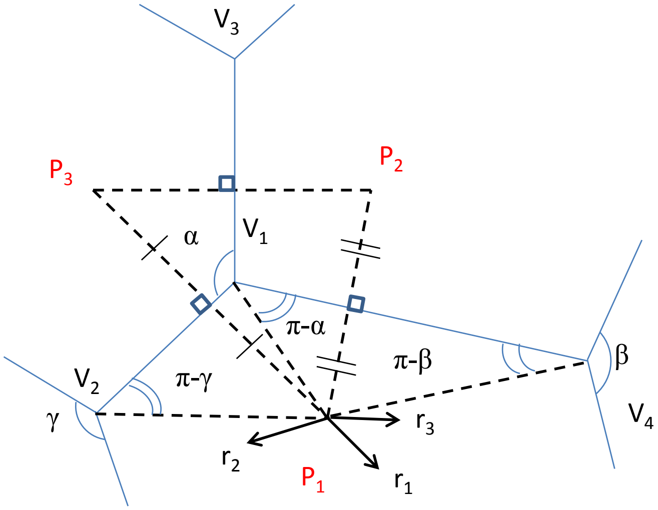

Figure 6.2: The geometrical method to obtain the generators from voronoi diagram

microstructures. In the current study, an age hardenable Mg-rare earth alloy WE43 T5 provided in the hot-rolled and aged condition with no intermediate solution treatment was used [46].

Since the microstructures are almost convex, it would be suitable to construct the equivalent convex microstructure before finding the voronoi generators. It is to be noted that every voronoi diagram produces convex polygons, but the converse doesn't hold true.

Fig. 6.3 outlines the process of obtaining the convex microstructure from the original microstructure. Fig. 6.3 a) shows the orginal microstructure which was obtained in a rasterized format. Convex hulls of individual grains are constructed from the original microstructure using the $\mathcal{MATLAB}$ function convhulln, which uses the popular Qhull method [18]. Figs 6.3 a) and b) show an internal facet A, which is probably a twinned region. It can be observed from Fig. 6.3 b) that there are many intersecting regions shared by 2 or 3 grains and they need to be assigned to a unique grain to obtain a convex microstructure. The procedure to sort the overlapping region is as follows :

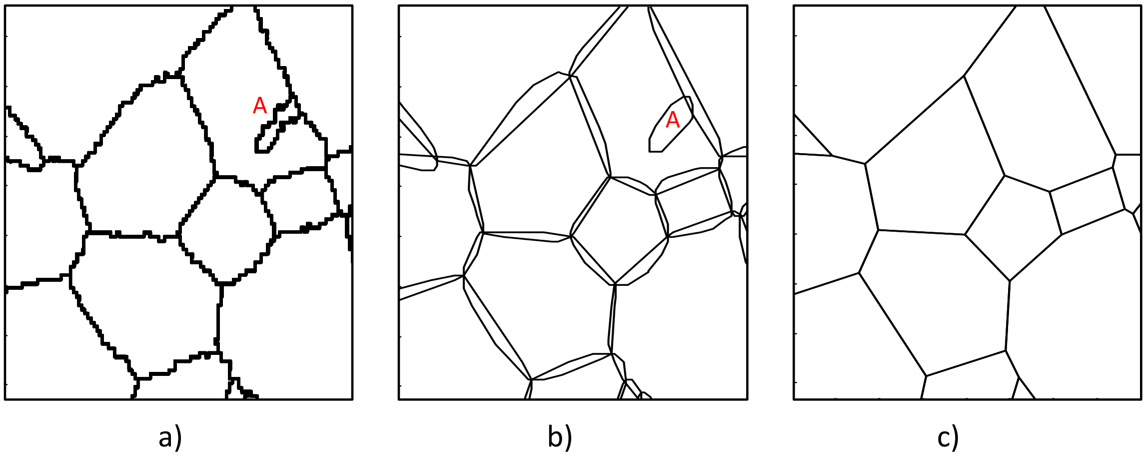

Figure 6.3: Method to obtain the 2-D convex microstructure. a)The original experimental microstructure (Grain A represents a twinned region, which is an internal facet of the parent grain). b) The convex hulls of individual grains. c) The resulting convex microstructure after dividing the intersecting regions among the individual grains.

1) In 2-dimensional space, convex hull is represented by a sequence of boundary points as indicated in Fig. 6.4 a). Connecting the points gives the convex polygon. By removing a particular point, the remaining points would still connect to give convex polygons.

2) The points of a polygon which are in other polygons are removed and the intersection points of the two polygons are included in both the polygons to form convex polygons again. This procedure can be followed for any two intersecting polygons and would give the same unique convex microstructure irrespective of the sequence followed.

Fig. 6.4 shows the procedure mentioned applied to Grains 1,2 and 3. Fig. 6.4 a) shows the grains with their original convex hulls and the corresponding points. Step 2 is applied to Grain 1 resulting in Fig. 6.4 b). It is again applied to Grain 2 resulting in Fig. 6.4 c). It is to be seen that after the procedure every 2 neighboring grains share an edge with two common points and every 3 neighboring grains share a triple

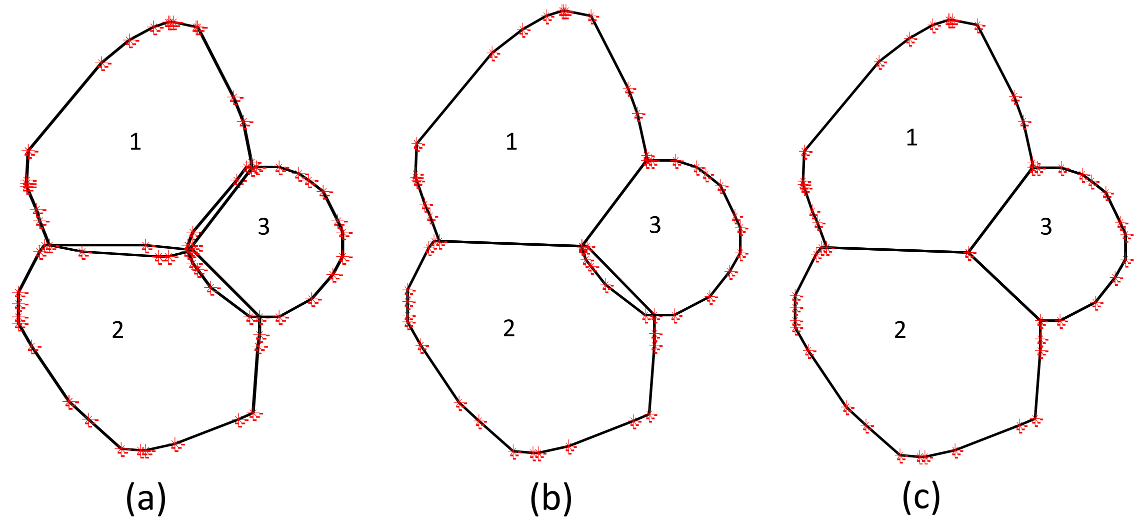

Figure 6.4: Method to remove the intersecting regions of the convex hulls a) Grains 1,2 and 3 with their overlapping convex hulls b) Step 2 is followed for Grain 1 c) Step 2 is followed for Grain 2

point. It can be shown that Step 2 followed in any sequence among the 3 Grains will give the same resulting microstructure.

Fig. 6.3 c) shows the procedure applied to the entire microstructure resulting in a fully convexified microstructure. It is to be noted that since the Region A is an internal facet, it will not be represented in the final microstructure. Methods to incorporate twinned regions are discussed in the chapter on conclusions.

6.2.2 Voronoi generators for a convex microstructure

Once the convex microstructure is generated, Eq. (6.4) is used to check if a unique generator point can be found for each grain. Fig. 6.5 a) shows Grain A with 6 edges and 6 vertices respectively, surrounded by the neighboring grains B, C, D, E, F and G. The procedure mentioned earlier in Fig. 6.2 is employed to construct the voronoi generator points A_1,A_2,A_3,A_4,A_5 and A_6 for grain A and the corresponding generator points for the neighboring grains.

Rays r_1, r_2, r_3, r_4, r_5 and r_6 are constructed by connecting the generator points A_1,A_2,A_3,A_4,A_5 and A_6 with their respective vertices. It can be seen from Fig. 6.5 (a) that the rays do not converge to a single point as in case for a voronoi diagram.

Since the aim is to represent the convex microstructure with voronoi generators, multiple generators are used to represent a single grain as compared to a single generator. Each grain is represented by voronoi generators equal to number of vertices of the grains. Fig. 6.5 (b) shows the voronoi polygons corresponding to each grain represented by dashed lines.

Therefore, for regular shaped convex grains, the microstructure can be represented by placing voronoi generators along the vertices or triple-points of the microstructure. In this study, we use the same radius of circumcircle r for obtaining generator points at all the vertices of the grains.

The method does show anomaly for long slender grains as shown in Fig. 6.6. Fig. 6.6 a) shows the inverse voronoi representation for grains A, B and C. It can be seen that the voronoi regions of grain A corresponding to the vertices P and Q cut into grain B as shown in the box. Similarly, voronoi region of grain B corresponding to vertex R cuts into grain C. This is due to fact that the grains A and B are slender with edges $\overline{RS}$ and $\overline{TU}$ much longer compared to the edges $\overline{PR}$, $\overline{QS}$ and $\overline{RT}$.

The issue can be addressed by using additional generator points at midpoint of the edges $\overline{RS}$ and $\overline{TU}$ as shown in Fig. 6.6 b). In this case, the voronoi regions of the generator points are bounded within the convex envelope of grains A and B.

In this study, we do not add additional generator points to the slender grains as we regenerate the 2-D convex surface-microstructure by convexifying the 3D microstructure as shall be explained in section 2.4.

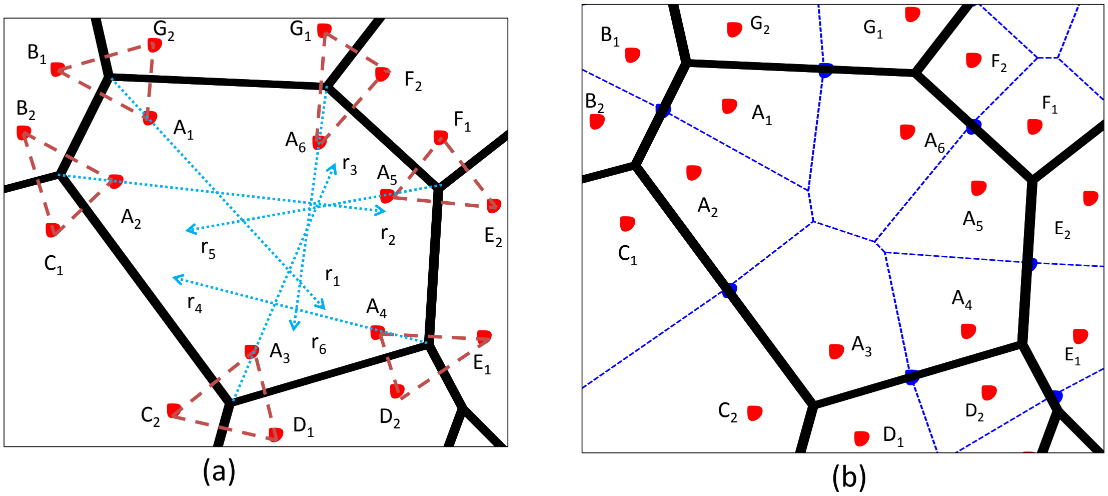

Figure 6.5: Method to obtain the generators from a convex microstructure. a) Rays $r_1, r_2, ..., r_6$ do not converge to a single point, therefore the grain A is represented by six voronoi generators $A_1, A_2, ...A_6$. b) The voronoi regions of the grain is indicated by dashed lines.

6.2.3 Construction of 3-D microstructure using Voronoi generators

Once the voronoi generator points are identified for the 2-D microstructure, a 3-D microstructure can be created by adding voronoi generator points in the z-direction. Here, we introduce an approach of using a large surface observation such as the EBSD map to find the generator points and their representative orientations in the z-direction by stacking sections of the surface EBSD maps in the z-direction.

The following assumptions are made while generating the 3-D microstructure,

1) The surface EBSD map is representative of the microstructure in the x-y plane across the depth of the sample, i.e., the sample is not textured along the z-direction. This is true in the case of rolled textures where ND direction represents the z-direction and for random textures arising out of a casting process

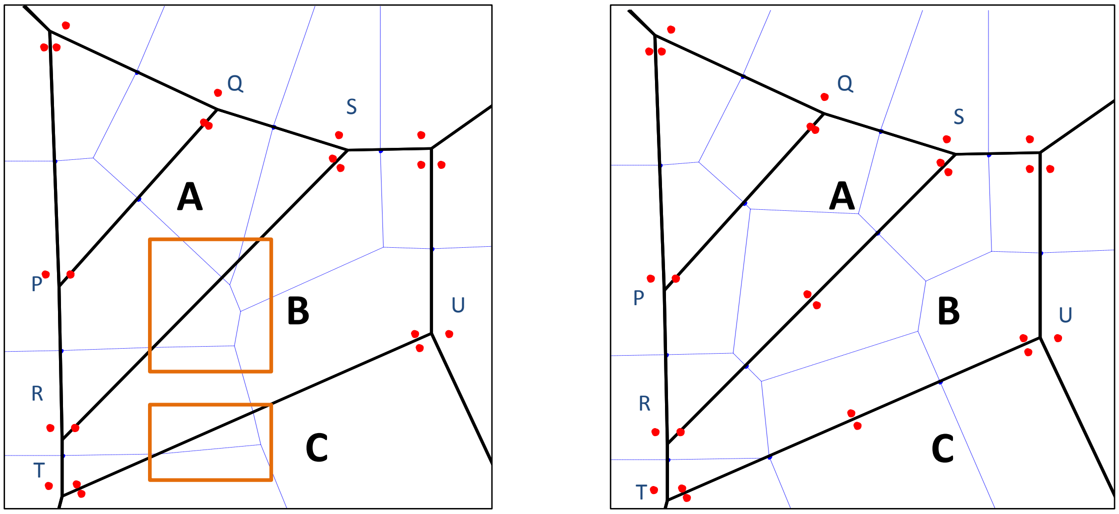

(a) (b)

Figure 6.6: In slender grains voronoi regions of generator points can extrude into the neighboring grains across the long edges. a) Voronoi Regions of slender grains A and B extrude into grains B and C as indicated by the boxed regions. b) Additional generator points are placed along the midpoint of edges $\overline{RS}$ and $\overline{TU}$ to bound the voronoi regions within the grain.

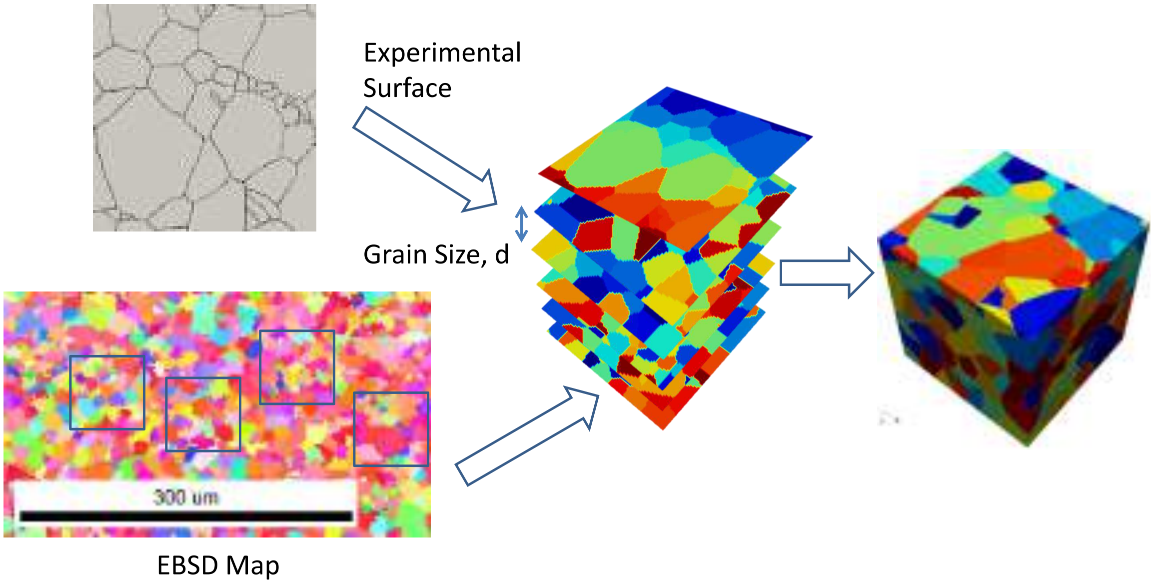

Figure 6.7: Schematic diagram showing the construction of 3-d microstructure from the given surface observation and EBSD map. Sections of the EBSD map are stacked below the microstructure using their centroid as voronoi generators.

2) The grains are equiaxed. With no information about the grain shape in the z-direction, it would be useful to assume equiaxed nature of the grains. Therefore, we stack the grains in layers with a gap-width of grain size 'd' (known from 2D).

3) The grains in the sections of EBSD map are represented by their centroid as Voronoi generators. It is assumed that the overall texture of the 3-d microstructure wouldn't change considerably by this assumption. Alternatively, we could convexify the sections and represent it by Voronoi points as shown is section 6.2.1-6.2.2.

To represent the distribution of Voronoi points in the z-direction, the generator points of the sections are perturbed in the z-direction by a normal distribution with a standard deviation of $\sigma = \frac{d}{2}$. Similarly, to account for the tilt and twist of the grain boundaries, the voronoi generator points of the top most layer are perturbed in the z-direction by a normal distribution with standard deviation equal radius of the circumcircle $\sigma = r$.

The voronoi diagram is recreated in 3D with the resultant voronoi points. Fig. 6.7 shows a schematic representation of the construction, resulting in the 3D microstructure.

6.2.4 3D Convex Microstruture

It can be observed from Fig. 6.7 and Fig. 6.9 a) that the grains in the surface are penetrated by the Voronoi generator points beneath the surface. We use the approach of convexification again to recover the surface microstructure. We use a property of convex hulls that every section of a 3D convex polygon gives a 2D convex polygon. Since we obtain 2D convex diagrams with the surface image, we can recover the surface convex microstructure when convexifying the entire 3D microstructure.

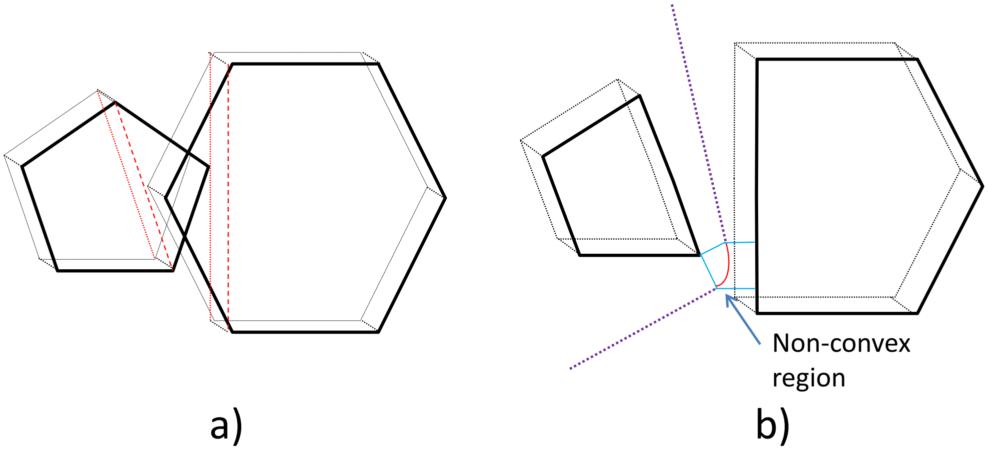

Figure 6.8: Method to convexify the 3D microstructure a) The intersecting points of the convex hulls of the grain are removed and the convex hulls are recreated b) The voxels in the gaps between the grains are assigned to the nearest grain by a linear least squares solver, the non-convex region of the partition is indicated.

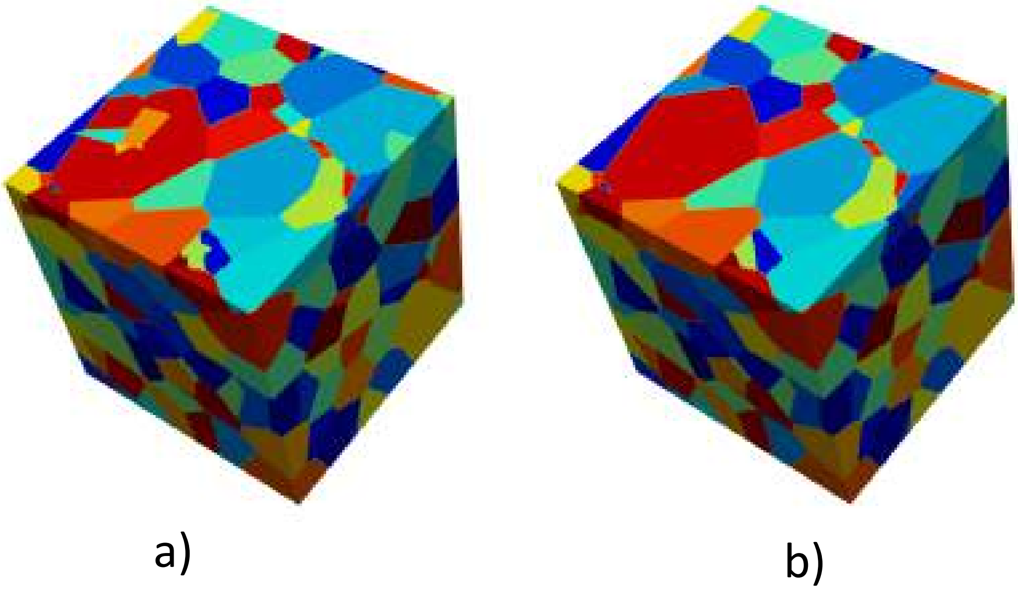

Figure 6.9: Convexification of 3-D microstructure a) Microstructure generated by the voronoi generators b) Convexified 3-D microstructure.

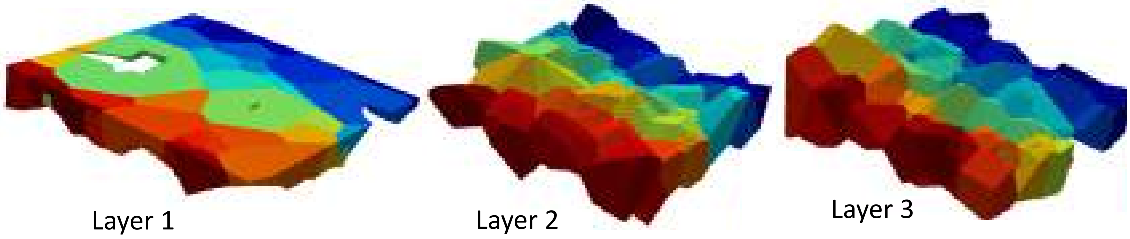

Figure 6.10: Top three layers of the microstructure before convexification

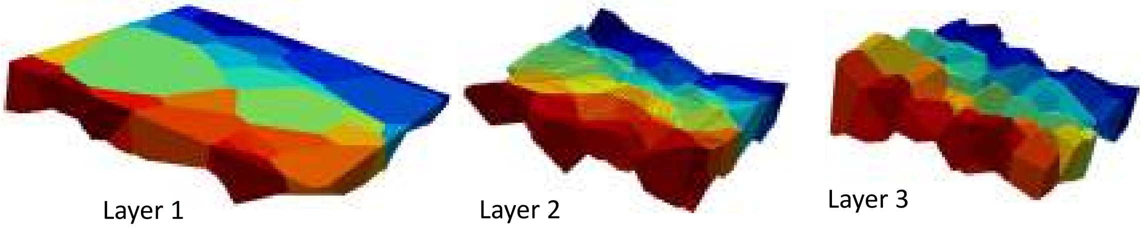

Figure 6.11: Top three layers of the microstructure after convexification

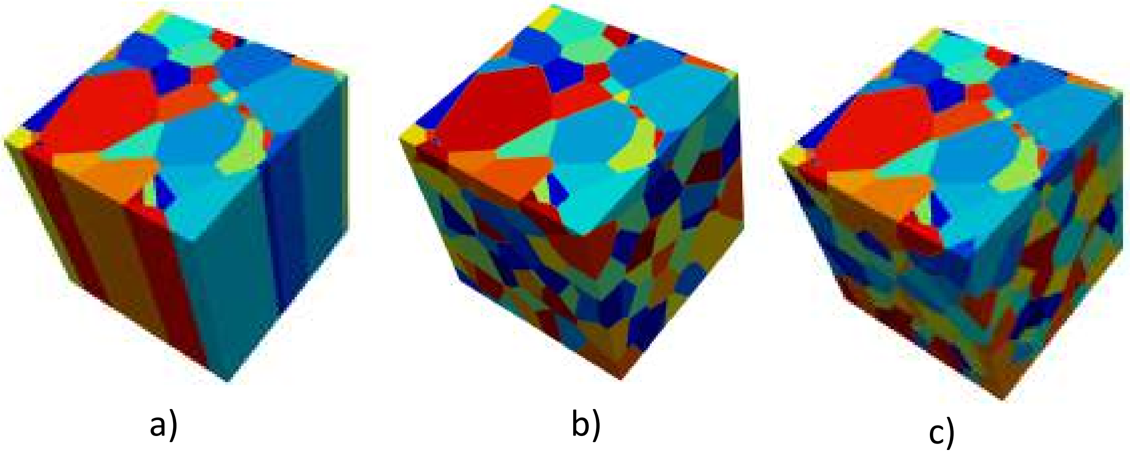

Figure 6.12: Microstructures considered in this study (a) Convexified columnar microstructure (b) variant 1 of 3d microstructure (c) variant 2 of 3d microstructure .

The problem of slender grains mentioned in section 2.2 is also addressed by convexifying the 3D microstructure.

The procedure for convexification in 3D is similar to the process of convexification followed in 2D, however a modified approach is described below is to create a voxelated 3D microstructure

1) Convex hulls of individual grains are recreated using the$\mathcal{MATLAB}$ function convhulln.

2) The points of a polygon which are in other polygons are removed as shown in Fig. 6.8 a). Instead of finding the intersection planes of the convex hulls, the convex hulls of the grains are reconstructed using the remaining vertices as shown in Fig. 6.8 b).

3) The gaps between the grains are assigned as voxels to the nearest grain using a linear least-squares solver. The problem of finding the smallest distance to a given voxel to a grain can be described as

$$\min_x \frac{1}{2}\|x-d\|_2^2 \qquad \boldsymbol{A}x \leq b \tag{6.6}$$

with d corresponding to the voxel to be assigned and $\boldsymbol{A}$x=b representing the planes enclosing the grain. The voxel is assigned to the grain corresponding to the smallest distance. Fig. 6.8 b) shows the partition between the grains by assigning the voxels to the nearest grain as described. The regions near the edges of the grain are assigned in a non-planar way as indicated in Fig. 6.8 b). This results in some non-convex regions in the 3D-microstructure. Exact 3D convex microstructures can be obtained by following the procedure in section 6.2.1.

Fig. 6.9 shows the initial microstructure and the resulting convexified microstructure. Fig. 6.10 shows the first 3 layers of the grains before convexification and Fig. 6.11 shows the same 3 layers after convexification. It can be observed that convexification affects only the top two layers , whereas the layers below are already convex due to nature of the voronoi diagram.

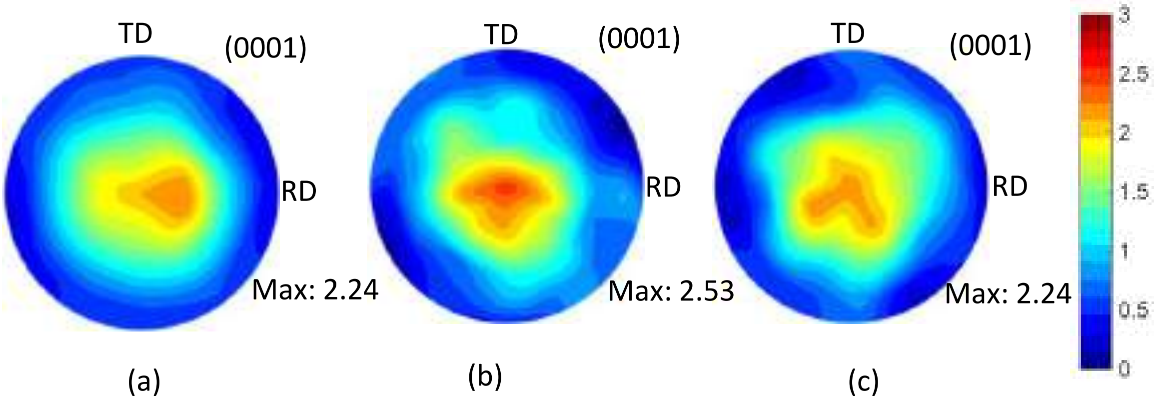

Figure 6.13: The (0001) recalculated pole figures for (a) EBSD data (b) 3d variant 1 (c) 3d variant 2.

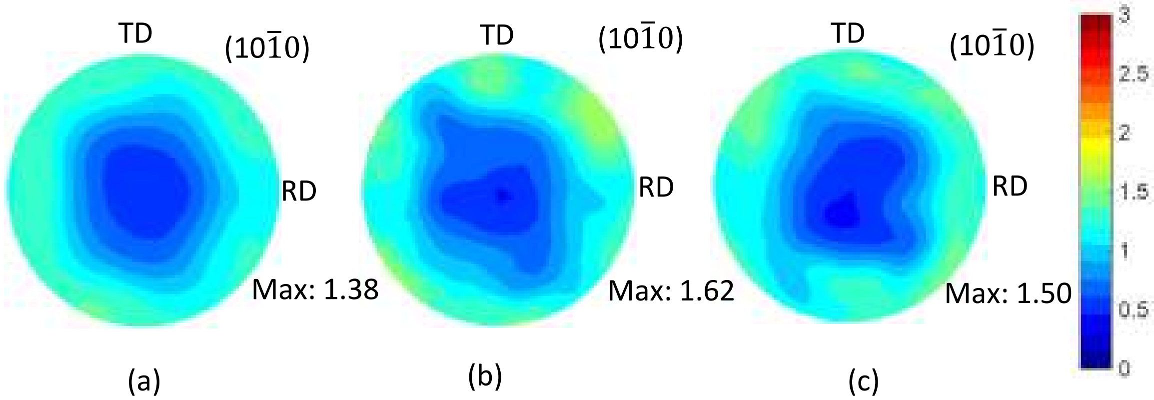

Figure 6.14: The $(10\bar{1}0)$ recalculated pole figures for (a) EBSD data (b) 3d variant 1 (c) 3d variant 2.

6.3 Implementation of the Algorithm

The above algorithm is implemented on an experimental microstructure obtained from SEM-DIC experiments for WE-43 T5 temper similar to the comparison in chapter 5 . The microstructure is of dimensions $75\mu m$*$75\mu m$. The microstructure com-

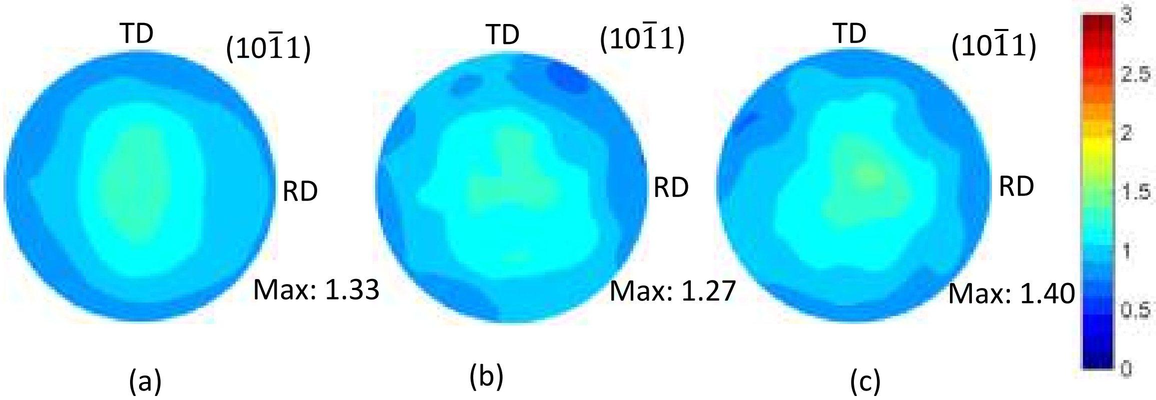

(a) (b) (c)

Figure 6.15: The $(10\bar{1}1)$ recalculated pole figures for (a) EBSD data (b) 3d variant 1 (c) 3d variant 2.

prises of 49 grains initially and after the process of convexification, the number of grains shrinks to 46. The twinned region such as one shown in Fig. 6.3 (a) is removed during the 2D convexification process. The surface EBSD map as obtained from experiments (courtesy Daly lab [46]) is of dimensions $600\mu m$*$700\mu m$ and comprises of 6000 grains. The average grain size of the 2D EBSD map is found to be 13 μm [46]. The procedure mentioned in section 6.2.3 is followed by selecting 5 random sections of grains of the dimensions $75\mu m$*$75\mu m$ from the surface EBSD map and finding their centroids. These collection of grains are stacked below the original experimental microstructure by a spacing of grain size 'd' and perturbed in the z-direction by a normal distribution with a standard deviation of $\sigma = \frac{d}{2}$. The resulting microstructure is then again convexified to obtain the 3D microstructural realizations as shown in Fig. 6.12, which are referred to as the variant 1 and variant 2 of 3D microstructure. Variant 1 comprises of 340 grains and variant 2 comprises of 367 grains. The displacement boundary conditions used in Chapter 4 are applied to the resultant microstructure and extended along the z-axis. The results of the simulations are discussed in the following section.

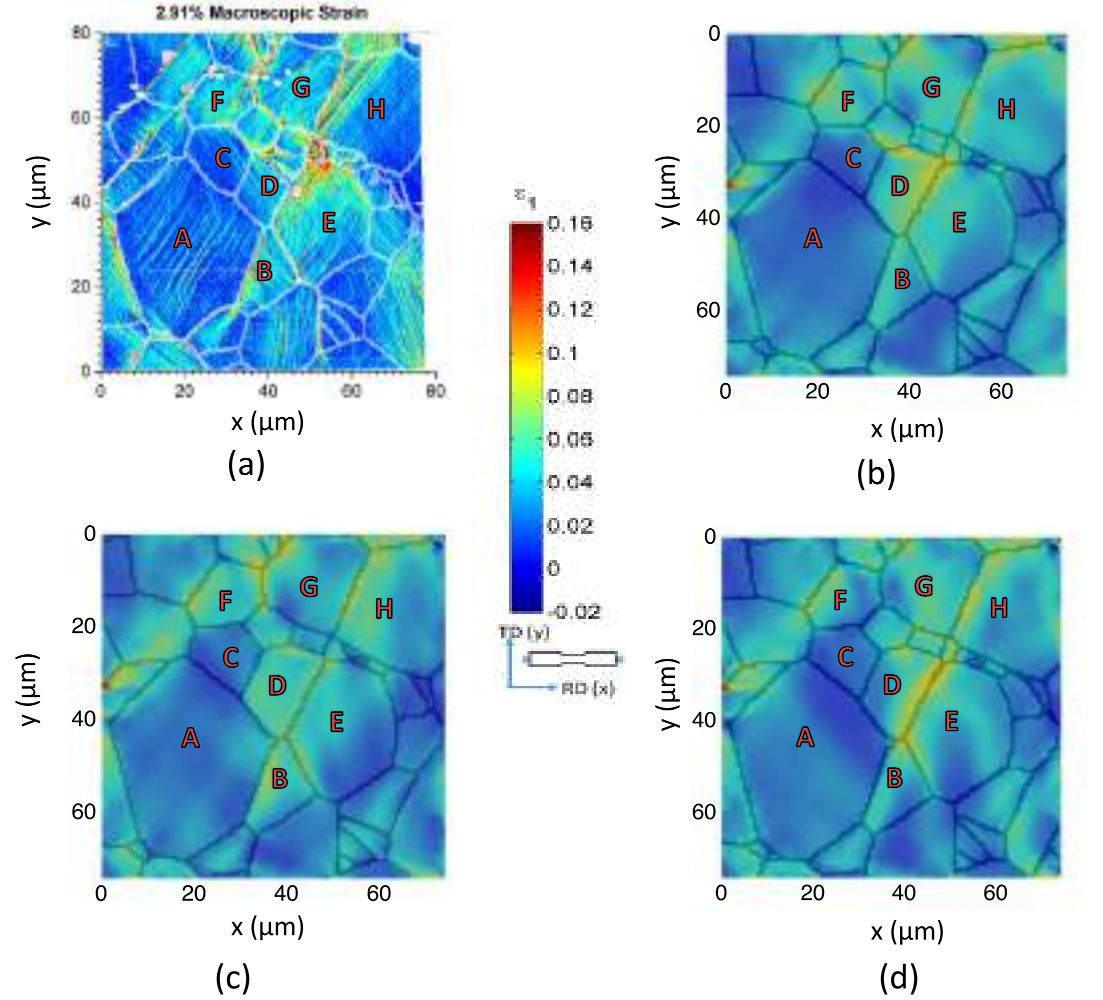

Figure 6.16: Comparison of principal strain ϵ_1 from (a) SEM-DIC experiments [46] (b) Convexified columnar microstructure (b) 3d variant 1 (c) 3d variant 2 .

6.4 Results and Discussion

The pole figures of the resultant microstructures are plotted in Figs. 6.13-6.15. It can be inferred from the plots that the texture of the microstructure variant 2 is more comparable to the EBSD texture from the experiments. The map of the principal strain E_1 is given in Fig. 6.16 for the SEM-DIC experiments. Individual grains A-H are marked to study the variation in strain between columnar microstructures and the 3D variants of the microstructures. Predominantly, we see that the surface strain maps are similar across the samples for all the observed grains and compare well with the experiments. To compare the observations better, we plot the relative activity of the individual slip systems, basal, prismatic, pyramidal$_{<a>}$, pyramidal$_{<c+a>}$ and twin systems as shown in Figs. 6.17 -6.21 . It can be seen that the grain 'A' shows predominantly prismatic activity in columnar microstructure and variant 1, whereas it shows both prismatic and pyramidal$_{<a>}$ activity in variant 2 of the microstructure from Figs. 6.18 and Fig. 6.19. Grain 'B' shows twinning activity in all the microstructures as seen in Fig. 6.21. Grain 'C' shows pyramidal$_{<c+a>}$ activity for columnar microstructure and variant 1, whereas it shows predominantly prismatic slip activity in variant 3 as seen in Figs. 6.18 and Fig. 6.20. Grain 'D' shows both basal slip and twin activity for all the microstructures as seen in Fig. 6.17 and Fig. 6.21. It is to be observed that grain 'D' shows strain concentrations accumulating at grain boundaries for the columnar microstructure and variant 2, whereas no such strain concentration is to be observed in 3D variant 1. Grain 'E' shows basal slip activity in all the microstructures as seen in Fig. 6.17, it shows some pyramidal$_{<a>}$ activity for variant 2 as seen in Fig. 6.19. The pyramidal$_{<a>}$ activity of variant 2 can be also distinctly observed in Fig. 6.16 (d). Grains 'F' and 'G' show basal and pyramidal$_{<a>}$ slip activity for all the three microstructures as can be seen in Figs. 6.17 and 6.19. Grain 'H' shows basal slip activity for the columnar variant in Fig. 6.17 whereas it shows both basal and twin activity for microstructure variants 1 and

2 as seen in Figs. 6.17 and Fig. 6.21. We see that the slip activity in grains A,C,E and H of microstructure variant 2 varies significantly from the columnar microstructure and grains A,C and E show differences in slip activity between 3D variant 1 and 3D variant 2. To observe the effect of underlying microstructure, we study the slip activity at different depths of the material for the 3D variant2 and examine the effect of underlying microstructure on the surface slip activity of the marked grains.

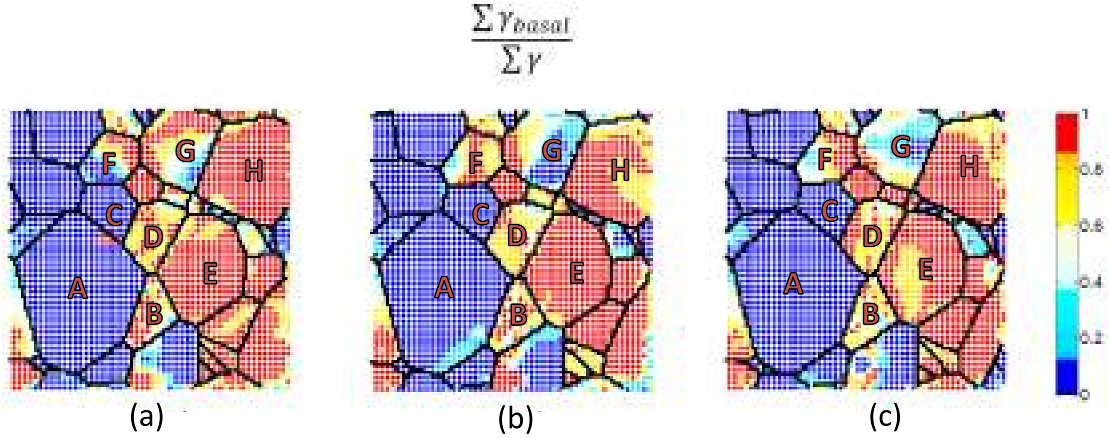

Figure 6.17: Comparison of relative activity of the combined basal slip using quadrature point data from CPFE model (a) columnar microstructure (b) 3d variant 1 (c) 3d variant 2

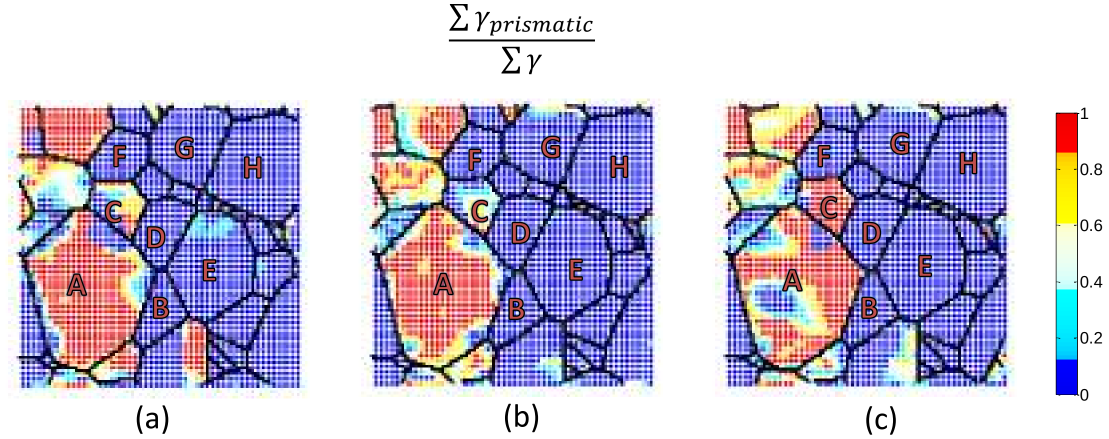

Figure 6.18: Comparison of relative activity of the combined prismatic slip using quadrature point data from CPFE model (a) columnar microstructure (b) 3d variant 1 (c) 3d variant 2

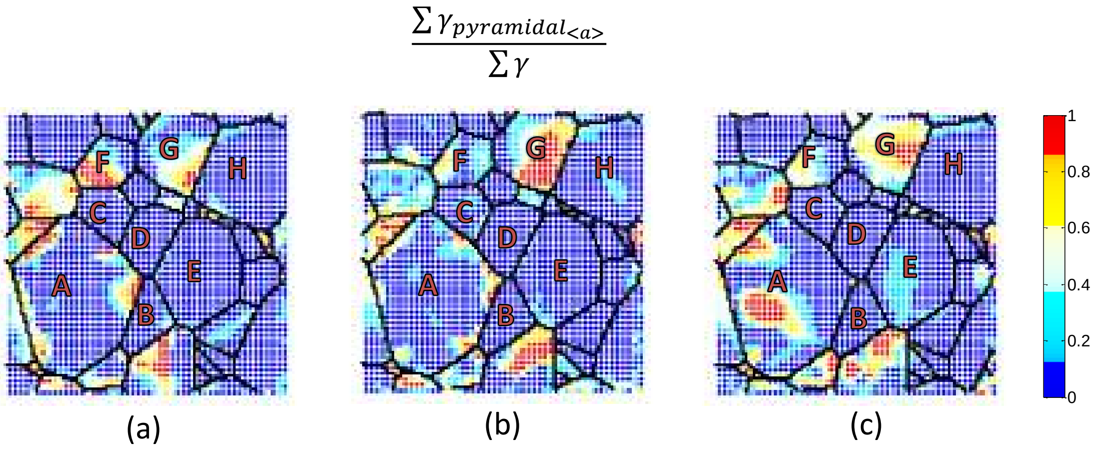

$$\frac{\sum \gamma_{pyramidal_{<a>}}}{\sum \gamma}$$

(a) (b) (c)

Figure 6.19: Comparison of relative activity of the combined pyramidal$_{<a>}$ slip using quadrature point data from CPFE model (a) columnar microstructure (b) 3d variant 1 (c) 3d variant 2

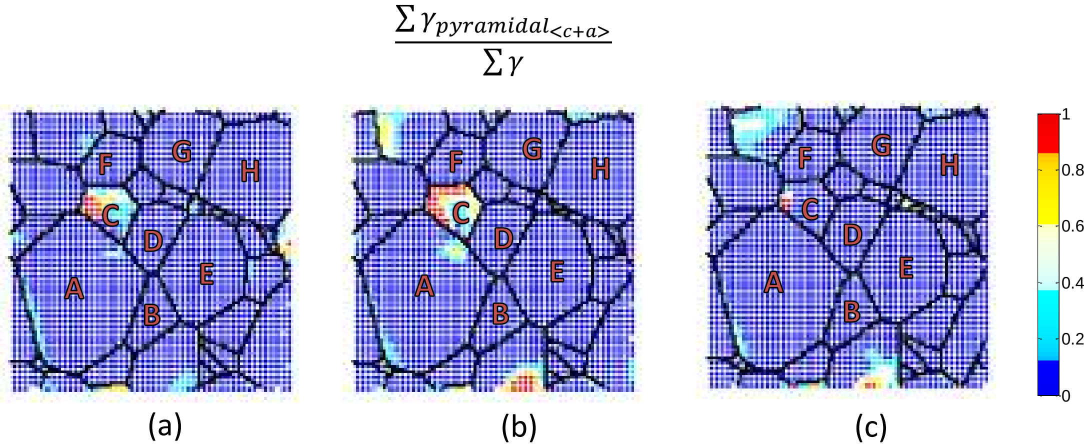

$$\frac{\sum \gamma_{pyramidal_{<c+a>}}}{\sum \gamma}$$

(a) (b) (c)

Figure 6.20: Comparison of relative activity of the combined pyramidal$_{<c+a>}$ slip using quadrature point data from CPFE model (a) columnar microstructure (b) 3d variant 1 (c) 3d variant 2

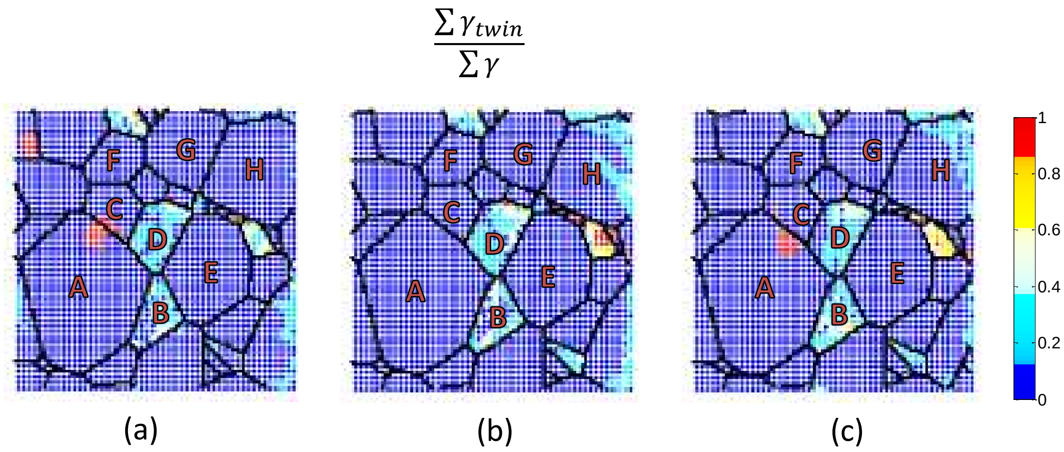

Figure 6.21: Comparison of relative activity of the combined twin slip using quadrature point data from CPFE model (a) columnar microstructure (b) 3d variant 1 (c) 3d variant 2

The relative slip activity of the 3D microstructure variant 3 at various depths are plotted in Figs. 6.22-6.26. It can be observed in case of grain 'A' where we see both prismatic and pyramidal$_{<a>}$ activity that the region of pyramidal$_{<a>}$ activity is probably due to the grains underneath the surface such as M and L which show strong basal slip activity. Grain 'C' which shows predominantly prismatic surface slip activity also has grains underneath such as N and K which show basal slip activity. The region of grain 'E' which shows pyramidal$_{<a>}$ activity arises possibly from the underneath grain 'J' which also shows pyramidal$_{<a>}$ activity. Grain 'H' which shows some twin activity has grain 'P' underneath which shows pyramidal$_{<c+a>}$ slip activity. It is also to be observed that grains 'A' and 'D' are not exactly convex due to the nature of the algorithm for 3D convexification. Also, it is observed that grains 'D' and 'G' extend far deeper into the microstructure and hence possibly show no differences in slip activity as compared to columnar microstructures.

The stress-strain curves of the 2 variants of 3D microstructures are generated for both simple tension and simple compression boundary conditions with a mesh of 100*100*100 elements using PRISMS-Plasticity code. A sample run of the code with the time required to run the code is provided in Appendix E. The results of

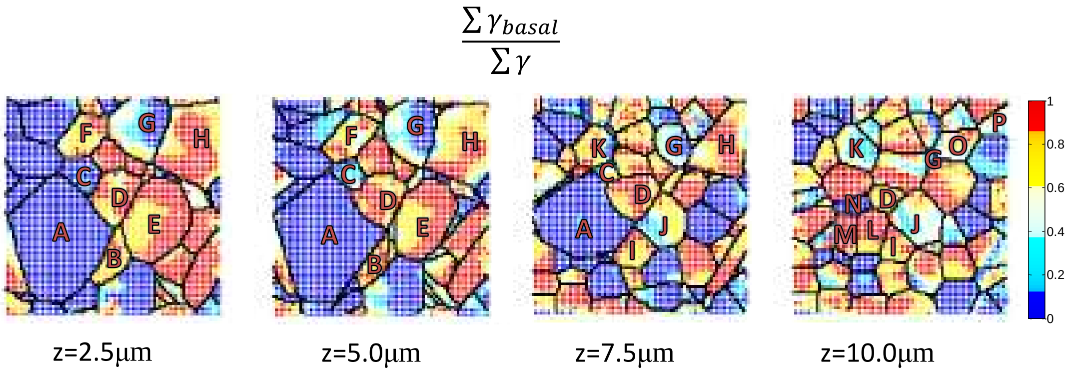

$$\frac{\sum \gamma_{basal}}{\sum \gamma}$$

Figure 6.22: Comparison of relative activity of the combined basal slip using quadrature point data from CPFE model for 3d variant 1 along the depth of the sample

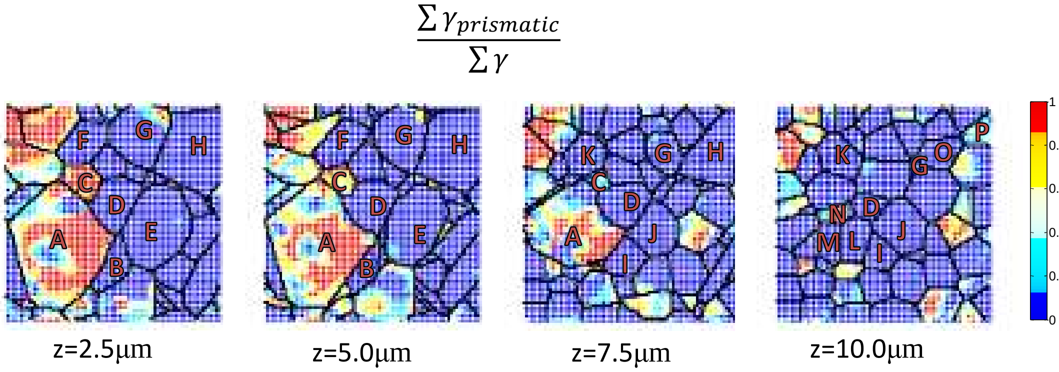

$$\frac{\sum \gamma_{prismatic}}{\sum \gamma}$$

Figure 6.23: Comparison of relative activity of the combined prismatic slip using quadrature point data from CPFE model for 3d variant 1 along the depth of the sample

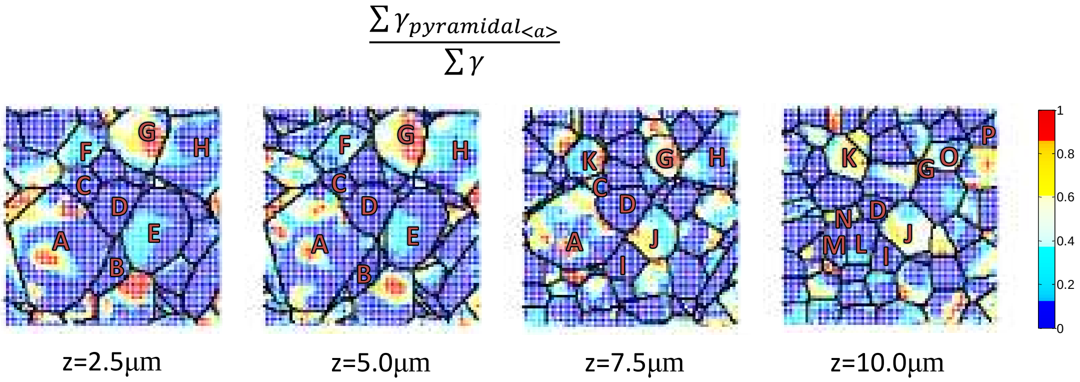

$$\frac{\sum \gamma_{pyramidal_{<a>}}}{\sum \gamma}$$

Figure 6.24: Comparison of relative activity of the combined pyramidal$_{<a>}$ slip using quadrature point data from CPFE model for 3d variant 1 along the depth of the sample

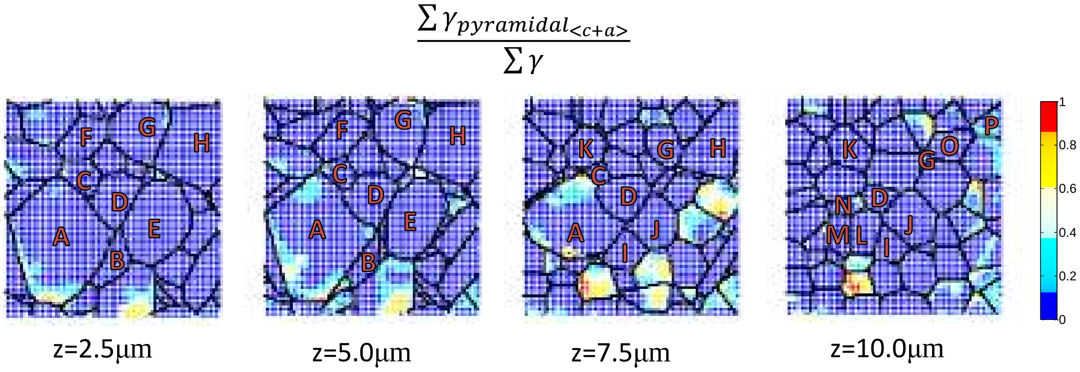

$$\frac{\sum \gamma_{pyramidal_{<c+a>}}}{\sum \gamma}$$

Figure 6.25: Comparison of relative activity of the combined pyramidal$_{<c+a>}$ slip using quadrature point data from CPFE model for 3d variant 1 along the depth of the sample

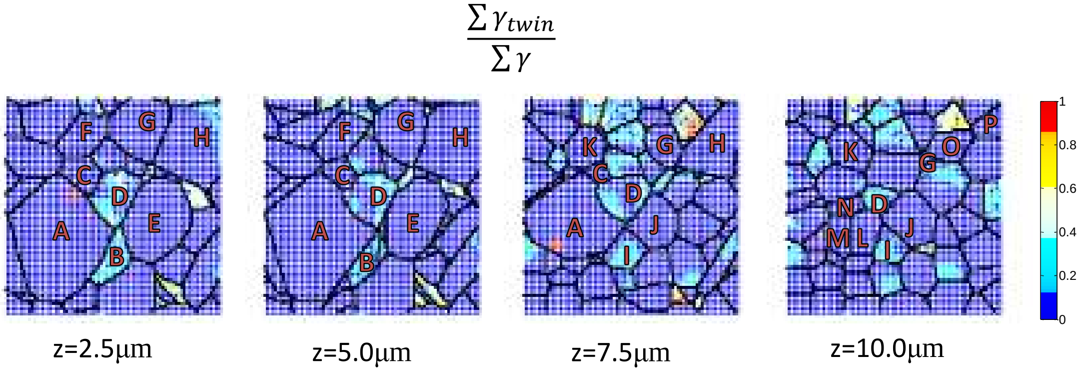

$$\frac{\sum \gamma_{twin}}{\sum \gamma}$$

Figure 6.26: Comparison of relative activity of the combined twin slip using quadrature point data from CPFE model for 3d variant 1 along the depth of the sample

the stress-strain curve are plotted in Fig. 6.27 and compared with the experimental stress strain curves provided in Fig. 3.8 (a). The results show a good match between the experiments and the simulations. It is to be observed that the simulations underpredict the stress-strain response for both tension and compression simulations. Since the average number of elements in these simulations are far greater than that required for convergence Fig. 3.6 , one possible explanation could be the effect of less no. of grains in the RVE (340 and 367) as compared to 500 grains required for convergence, as seen in Fig. 3.7 (b).

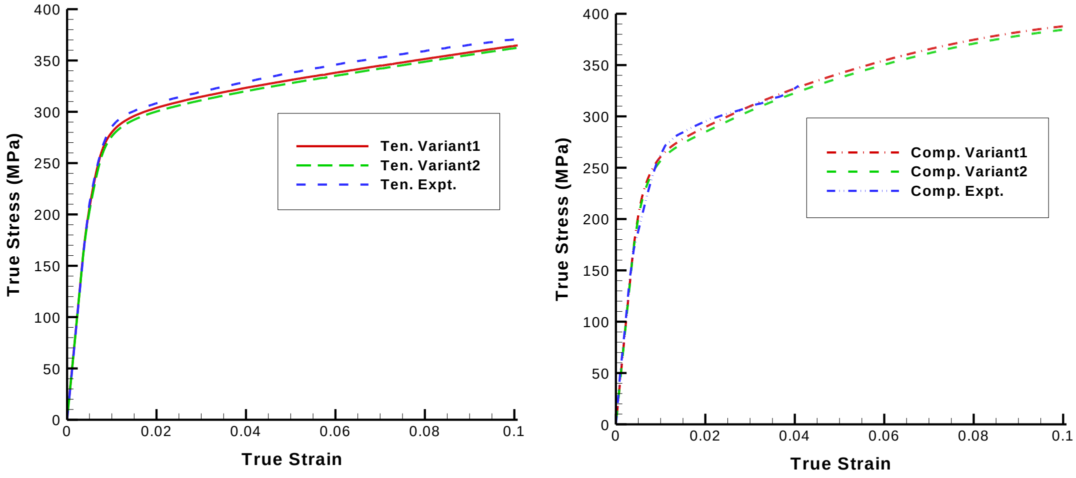

(a)

(b)

Figure 6.27: Experimental and simulated stress-strain curves for (a) tension (b) compression

6.5 Conclusions

In this chapter, we developed an approach for the construction of 3D microstructures from 2D surface microstructures. The use of a generalized inverse voronoi approach makes this technique much more elegant as compared to growing microstructures from expanding or eroding the grains below the 2D microstructure [119, 120].

The resultant microstructures showed similarities with the surface EBSD map in terms of texture. The plastic deformation band developing at the surface shows dependency on the 3D morphology of the grains beneath the surface. Thus, the results presented in this work show the implications of performing a full 3D finite element analysis of the problem as compared to the 2D approach. The extensions of this approach to consider non-convex microstructures and twinned regions are discussed in the chapter on conclusions.

CHAPTER VII

Conclusions

7.1 Summary

The key contributions of this dissertation are summarized as follows :

1) In chapter 2, we developed a modification to the active-set search scheme of the rate-independent model as part of PRISMS-Plasticity to ensure that all the slip systems lie on or inside the yield surface and also developed a consistent tangent moduli to enable convergence of the model for small loading increments. This is a new iterative approach that gives good convergence Appendix E.

2) In chapter 3, we developed a methodology to match the texture of the EBSD data to the RVE generated to fit the crystal plasticity slip resistance and hardening parameters to the experimental data. Studies were also conducted for mesh convergence, number of grains required for matching texture to the RVE and the equivalence of multiple RVEs for numerical simulations. Textures and relative activity of the slip systems were generated for the provided experimental data and were predicted for possible experiments along other loading directions.

3) In chapter 4, we developed a method to compare DIC experiments which were conducted on WE43-T6 temper [46] to CPFE simulations by setting up a boundary value problem. To the knowledge of the author, this is the first time that exact strains were compared with DIC experiments and the first time SEM-DIC experiments have

been compared with CPFE models for magnesium alloys. Studies were made on the effect of basal schmid factor, grain size on the error in strains between DIC experiments and CPFE simulations.

4) In chapter 5, similar CPFE-DIC comparisons were set up for the WE43-T5 temper, where fine-scale experiments predicted the slip-traces in different grains. The CPFE model is able to identify Schmid factor variations due to the effect of neighbor grains in the form of relative slip activity, and thus computationally differentiate the slip traces observed in the DIC data into various slip and twin systems. Such simulations provide an avenue for physically interpreting the various slip traces observed in the dense DIC data.

5) In chapter 6, we developed a generalized inverse voronoi problem approach to model 3D microstructures from the surface EBSD maps and thus enable comparison of SEM-DIC experiments with a 3D microstructure. The simulations results showed both similarities and some variations as compared to a columnar microstructure which was studied in chapter 3 and chapter 4. Thus, these comparisons serve as a useful step for the ultimate validation of the continuum crystal plasticity theory.

A combination of these developed tools and methods in an Integrated Computational Materials Engineering (ICME) framework provides a powerful tool to accelerate alloy development and process design and optimization.

7.2 Future Work

This work can lead towards further development in the possible directions as listed below,

7.2.1 Modeling grain size effects and grain boundary behavior

The modeling of grain boundary behavior (migration and interaction with dislocation) mainly relies on atomistic simulations and identification of mechanisms for interface models to be included in continuum crystal plasticity [120, 63, 43]. The comparisons with DIC experiments showed the effect of grain size on the errors between the CPFE and DIC comparisons. Addition of a grain size effect term for the computation of slip deformation resistance would be a simple way to incorporate the effect of grain size in the CPFE model. The grain size effect can be incorporated in terms of a micro-Hall Petch term [92] or using non–local theories that explicitly incorporate a length scale dependence [97, 44, 45].

7.2.2 Capturing Geometrically Necessary Dislocations (GNDs)

One of the objectives of this work has been to capture the mechanical response and texture evolution due to slip and deformation twinning. A shortcoming in this work is that the effect of geometrically necessary dislocations (GNDs) is ignored. Dislocation density based CPFE models involving the evolution of GNDs and SSDs have been proposed and implemented in [31, 67] . Strain gradient crystal plasticity theories, incorporating the storage of GNDs due to strain gradients, have been proposed in [29, 51, 52, 53] . These strain gradient crystal plasticity theories require the implementation of higher order boundary conditions corresponding to the primary solution fields of plastic strain. Although more accurate, the higher order theories have increased complexity of modeling and reduced efficiency due to additional degrees of freedom compared to displacement based CPFE formulations.

7.2.3 Modeling non-convex grains and twinned regions in 3D microstructures

In Chapter 6, we developed a methodology to model 3D convex microstructures. However, many realistic microstructures are non-convex, especially the microstructures developed from 3D printing and casting process. A simple extension of the same algorithm can be used to model non-convex microstructures by partitioning the non-convex grains to convex grains using some of the already available popular algorithms such as triangulation [77], the Hertel-Mehlhorn algorithm [71] and Chazelle's complex cubic algorithm [30]. Since twinned region is an internal facet of the grain, the twin can either propagate across the grain thus splitting the grain into multiple regions or it might not propagate the length of the grain as seen in chapter 6. In either cases, the twinned region can be considered as a separate grain and the remaining grain can be split into multiple convex regions using the above mentioned algorithm.

Other additions to the code anticipated in the future include microstructural fracture, rate and temperature dependence, kinematic hardening and recrystallization. These are being added [94, 79] due to the open-source nature of the code.

APPENDICES

APPENDIX A

Computation of elastic stored energy

The stress power per unit volume $\dot{\omega}$ of the isoclinic relaxed configuration is given as [11]

$$\dot{\omega} = \det(\boldsymbol{F})\boldsymbol{\sigma} \cdot \boldsymbol{L} \tag{A.1}$$

where $\boldsymbol{F}$ is the deformation gradient, $\boldsymbol{\sigma}$ is the Cauchy stress and $\boldsymbol{L}$ is the velocity gradient. Decomposing the velocity gradient into elastic and plastic components, Eq. (A.1) becomes

$$\begin{aligned} \dot{\omega} &= \dot{\omega}^e + \dot{\omega}^p \\ &= \det(\boldsymbol{F})\boldsymbol{\sigma} \cdot (\dot{\boldsymbol{F}}^e(\boldsymbol{F}^e)^{-1}) + \det(\boldsymbol{F})\boldsymbol{\sigma} \cdot (\boldsymbol{F}^e\dot{\boldsymbol{F}}^p(\boldsymbol{F}^p)^{-1}(\boldsymbol{F}^e)^{-1}) \end{aligned} \tag{A.2}$$

The elastic stored energy is given by integrating the elastic component of stress power

$$\phi_{stored} = \int_0^t \int_{\bar{\mathcal{B}}} \dot{\omega}^e dV dt \tag{A.3}$$

The elastic component of stress power can be rearranged as

$$\begin{aligned}
\dot{\omega}^e &= \det(\boldsymbol{F})\boldsymbol{\sigma} \cdot (\dot{\boldsymbol{F}}^e(\boldsymbol{F}^e)^{-1}) \\
&= tr(\dot{\boldsymbol{F}}^e(\boldsymbol{F}^e)^{-1}(\det(\boldsymbol{F})\boldsymbol{\sigma})^T) \\
&= tr((\dot{\boldsymbol{F}}^e(\boldsymbol{F}^e)^{-1}\det(\boldsymbol{F})\boldsymbol{\sigma}) \\
&= tr((((\boldsymbol{F}^e)^{-1})^T(\boldsymbol{F}^e)^T\dot{\boldsymbol{F}}^e(\boldsymbol{F}^e)^{-1}\det(\boldsymbol{F})\boldsymbol{\sigma}) \\
&= tr(((\boldsymbol{F}^e)^T\dot{\boldsymbol{F}}^e(\boldsymbol{F}^e)^{-1}\det(\boldsymbol{F})\boldsymbol{\sigma}((\boldsymbol{F}^e)^{-1})^T) \\
&= (\boldsymbol{F}^e)^{-1}\det(\boldsymbol{F})\boldsymbol{\sigma}((\boldsymbol{F}^e)^{-1})^T \cdot ((\boldsymbol{F}^e)^T\dot{\boldsymbol{F}}^e) \\
&= (\boldsymbol{F}^e)^{-1}\det(\boldsymbol{F}^e)\boldsymbol{\sigma}((\boldsymbol{F}^e)^{-1})^T \cdot \dot{\bar{\boldsymbol{E}}}^e \\
&= \bar{\boldsymbol{T}} \cdot \dot{\bar{\boldsymbol{E}}}^e
\end{aligned} \tag{A.4}$$

This gives the conjugate stress measure which is defined as $\bar{\boldsymbol{T}} = \det(\boldsymbol{F}^e)(\boldsymbol{F}^e)^{-1}\boldsymbol{\sigma}(\boldsymbol{F}^e)^{-T}$. The plastic component of the stress power can be rearranged as

$$\begin{aligned}
\dot{\omega}^p &= \det(\boldsymbol{F})\boldsymbol{\sigma} \cdot (\boldsymbol{F}^e\dot{\boldsymbol{F}}^p(\boldsymbol{F}^p)^{-1}(\boldsymbol{F}^e)^{-1}) \\
&= tr(\boldsymbol{F}^e\dot{\boldsymbol{F}}^p(\boldsymbol{F}^p)^{-1}(\boldsymbol{F}^e)^{-1}(\det(\boldsymbol{F})\boldsymbol{\sigma})^T) \\
&= tr(\boldsymbol{F}^e\dot{\boldsymbol{F}}^p(\boldsymbol{F}^p)^{-1}(\boldsymbol{F}^e)^{-1}\det(\boldsymbol{F})\boldsymbol{\sigma}) \\
&= tr(\det(\boldsymbol{F})\boldsymbol{\sigma}\boldsymbol{F}^e\dot{\boldsymbol{F}}^p(\boldsymbol{F}^p)^{-1}(\boldsymbol{F}^e)^{-1}) \\
&= tr((\boldsymbol{F}^e)^{-1}\det(\boldsymbol{F})\boldsymbol{\sigma}\boldsymbol{F}^e\dot{\boldsymbol{F}}^p(\boldsymbol{F}^p)^{-1}) \\
&= tr((\boldsymbol{F}^e)^{-1}\det(\boldsymbol{F})\boldsymbol{\sigma}((\boldsymbol{F}^e)^{-1})^T(\boldsymbol{F}^e)^T\boldsymbol{F}^e\dot{\boldsymbol{F}}^p(\boldsymbol{F}^p)^{-1}) \\
&= tr(\bar{\boldsymbol{T}}\boldsymbol{C}^e\dot{\boldsymbol{F}}^p(\boldsymbol{F}^p)^{-1}) \\
&= (\boldsymbol{C}^e\bar{\boldsymbol{T}}) \cdot \boldsymbol{F}^p(\boldsymbol{F}^p)^{-1}
\end{aligned} \tag{A.5}$$

The resolved stress on the α^{th} slip system is thus defined by $\tau^\alpha = (\boldsymbol{C}^e\ \bar{\boldsymbol{T}}) \cdot \boldsymbol{S}_0^\alpha$.

Using the relation $\bar{\boldsymbol{T}} = \boldsymbol{\mathcal{L}}^e\left[\bar{\boldsymbol{E}}^e\right]$, the elastic stored energy becomes

$$\begin{aligned}
\phi_{stored} &= \int_0^t \int_{\bar{\mathcal{B}}} \bar{\boldsymbol{T}} \cdot \dot{\bar{\boldsymbol{E}}}^e dV dt \\
&= \int_0^t \int_{\bar{\mathcal{B}}} \boldsymbol{\mathcal{L}}^e\left[\bar{\boldsymbol{E}}^e\right] \cdot \dot{\bar{\boldsymbol{E}}}^e dV dt \qquad \text{(A.6)}
\end{aligned}$$

APPENDIX B

PRISMS-Plasticity: Simple tension example -FCC Copper

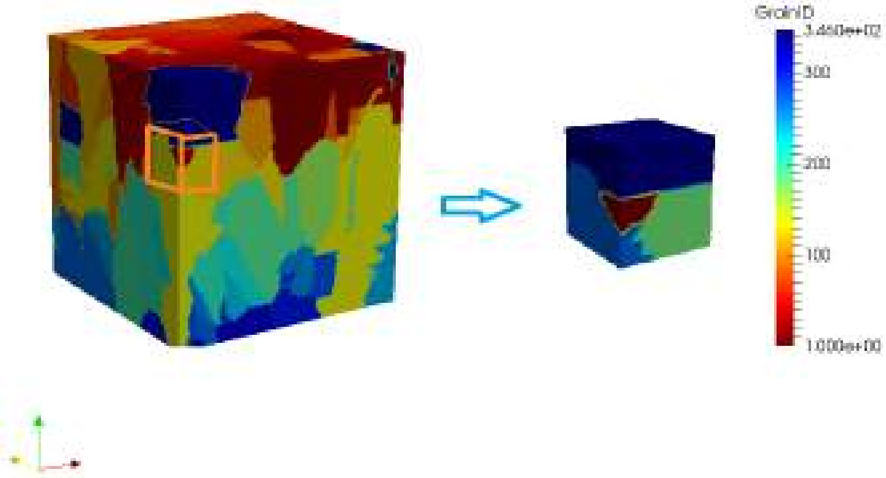

Figure B.1: Input microstructure (3D Materials Atlas

This is an illustrative example of a simple tension deformation problem. A real microstructure was tested with the material parameters of fcc Copper which were obtained from [12]

Input Parameters

```
/*FE parameters*/
#define feOrder   1 // Basis function interpolation order (1-linear)
#define quadOrder 2 // Quadrature point order n^3 (2->8 quadrature points)

/*Mesh parameters*/
//Set the length of the domain in all three dimensions
//Each axes spans from zero to the specified length
#define spanX 1.0
#define spanY 1.0
#define spanZ 1.0
// The number of elements in each direction is 2^(refineFactor) *
  subdivisions
// For optimal performance, use meshRefineFactor primarily to determine
  the element size
#define subdivisionsX 1
#define subdivisionsY 1
#define subdivisionsZ 1
#define meshRefineFactor 3 // 2^n*2^n*2^n elements(3->8*8*8 =512 elements)
#define writeMeshToEPS  true //Only written for serial runs and if number
  of elements < 10000

/*Solution output parameters*/
#define writeOutput true // flag to write output vtu and pvtu files
#define outputDirectory "."
#define skipOutputSteps 0
#define output_Eqv_strain true
```

```
#define output_Eqv_stress true
#define output_Grain_ID   true

/*Solver parameters*/
#define linearSolverType PETScWrappers::SolverCG // Type of linear solver
#define totalNumIncrements 100 // No. of increments
#define maxLinearSolverIterations 50000 // Maximum iterations for linear
   solver
#define relLinearSolverTolerance  1.0e-10 // Relative linear solver
   tolerance
#define maxNonLinearIterations 4 // Maximum no. of non-linear iterations
#define absNonLinearTolerance 1.0e-18 // Non-linear solver tolerance
#define relNonLinearTolerance 1.0e-3 // Relative non-linear solver
   tolerance
#define stopOnConvergenceFailure false // Flag to stop problem if
   convergence fails

/*Adaptive time-stepping parameters*/
#define enableAdaptiveTimeStepping false //Flag to enable adaptive time
   steps
#define adaptiveLoadStepFactor 0.5 // Load step factor
#define adaptiveLoadIncreaseFactor 1.25
#define succesiveIncForIncreasingTimeStep 10

//Elastic Parameters
double elasticStiffness[6][6]={{170.0e3, 124.0e3, 124.0e3, 0, 0, 0},
           {124.0e3, 170.0e3, 124.0e3, 0, 0, 0},
           {124.0e3, 124.0e3, 170.0e3, 0, 0, 0},
           {0, 0, 0, 75.0e3, 0, 0},
```

```
          {0, 0, 0, 0, 75.0e3, 0},
          {0, 0, 0, 0, 0, 75.0e3}}; //   Elastic Stiffness Matrix -Voigt
   Notation (MPa)



//Crystal Plasticity parameters
#define numSlipSystems 12 // generally 12 for FCC
#define latentHardeningRatio 1.4  //q1

double initialSlipResistance[numSlipSystems]= {16.0, 16.0, 16.0, 16.0,
   16.0, 16.0, 16.0, 16.0, 16.0, 16.0, 16.0, 16.0}; //CRSS of the slip
   sytems
double initialHardeningModulus[numSlipSystems]= {180.0, 180.0, 180.0,
   180.0, 180.0, 180.0, 180.0, 180.0, 180.0, 180.0, 180.0, 180.0};
   //Hardening moduli of slip systems
double powerLawExponent[numSlipSystems]= {2.25, 2.25, 2.25, 2.25, 2.25,
   2.25, 2.25, 2.25, 2.25, 2.25, 2.25, 2.25}; // Power law coefficient
double saturationStress[numSlipSystems]= {148.0, 148.0, 148.0, 148.0,
   148.0, 148.0, 148.0, 148.0, 148.0, 148.0, 148.0, 148.0}; // Saturation
   stress

//Slip systems files
#define slipDirectionsFile "slipDirections.txt" // Slip Directions File
#define slipNormalsFile "slipNormals.txt" // Slip Normals File


// Crystal Plasticity Constitutive model tolerances (for advanced users)
```

```
#define modelStressTolerance 1.0e-6 // Stress tolerance for the yield
   surface (MPa)
#define modelMaxSlipSearchIterations 20 // Maximum no. of active slip
   search iterations
#define modelMaxSolverIterations 10 // Maximum no. of iterations to
   achieve non-linear convergence
#define modelMaxPlasticSlipL2Norm 0.8 // L2-Norm of plastic slip
   strain-used for load-step adaptivity



//Read Input Microstructure
unsigned int numPts[3]={20, 20, 22}; // No. of voxels in x,y and z
   directions
#define grainIDFile "grainID.txt" // Grain ID File
#define headerLinesGrainIDFile 5 // No. of header Lines
#define grainOrientationsFile "orientations.txt" // Slip Normals File
```

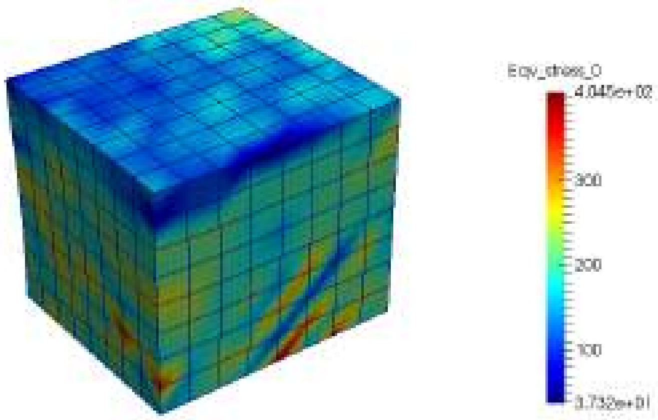

Figure B.2: Equivalent Von-Mises Stress shown on a deformation field

Table B.1: FCC Copper Slip Systems

System Number	Slip Direction	Slip Plane
1	[1 1 0]	(1 1 1)
2	[-1 0 1]	(1 1 1)
3	[0 1 -1]	(1 1 1)
4	[1 0 1]	(-1 1 1)
5	[-1 -1 0]	(-1 1 1)
6	[0 1 -1]	(-1 1 1)
7	[-1 0 1]	(1 -1 1)
8	[0 -1 -1]	(1 -1 1)
9	[1 1 0]	(1 -1 1)
10	[-1 1 0]	(-1 -1 1)
11	[1 0 1]	(-1 -1 1)
12	[0 -1 -1]	(-1 -1 1)

APPENDIX C

PRISMS-Plasticity: Simple tension example -BCC Titanium

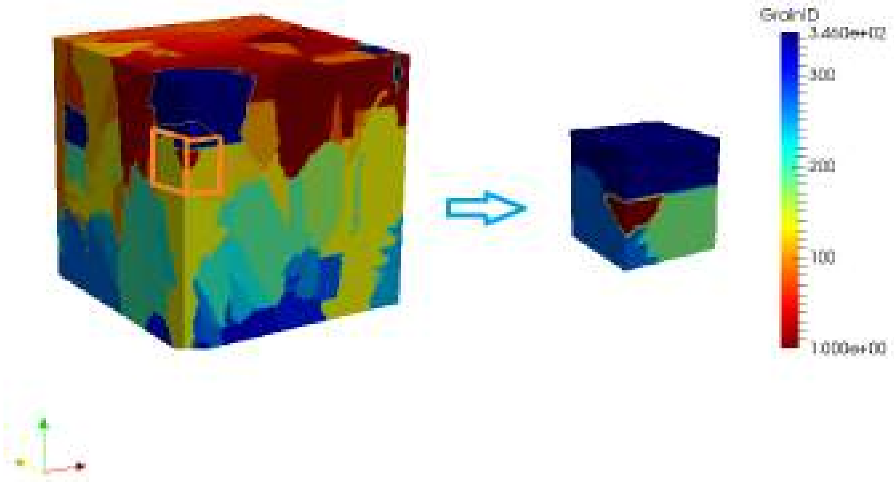

Figure C.1: Input microstructure

This is an illustrative example of a simple tension deformation problem. A real microstructure was tested with the material parameters of bcc β Ttitanium which were obtained from [64]

Input Parameters

```
/*FE parameters*/
#define feOrder   1 // Basis function interpolation order (1-linear)
#define quadOrder 2 // Quadrature point order n^3 (2->8 quadrature points)

/*Mesh parameters*/
//Set the length of the domain in all three dimensions
//Each axes spans from zero to the specified length
#define spanX 1.0
#define spanY 1.0
#define spanZ 1.0
// The number of elements in each direction is 2^(refineFactor) *
   subdivisions
// For optimal performance, use meshRefineFactor primarily to determine
   the element size
#define subdivisionsX 1
#define subdivisionsY 1
#define subdivisionsZ 1
#define meshRefineFactor 3 // 2^n*2^n*2^n elements(3->8*8*8 =512 elements)
#define writeMeshToEPS  true //Only written for serial runs and if number
   of elements < 10000

/*Solution output parameters*/
#define writeOutput true // flag to write output vtu and pvtu files
#define outputDirectory "."
#define skipOutputSteps 0
#define output_Eqv_strain true
```

```
#define output_Eqv_stress true
#define output_Grain_ID   true


/*Solver parameters*/
#define linearSolverType PETScWrappers::SolverCG // Type of linear solver
#define totalNumIncrements 100 // No. of increments
#define maxLinearSolverIterations 50000 // Maximum iterations for linear
   solver
#define relLinearSolverTolerance  1.0e-10 // Relative linear solver
   tolerance
#define maxNonLinearIterations 4 // Maximum no. of non-linear iterations
#define absNonLinearTolerance 1.0e-18 // Non-linear solver tolerance
#define relNonLinearTolerance 1.0e-3 // Relative non-linear solver
   tolerance
#define stopOnConvergenceFailure false // Flag to stop problem if
   convergence fails

/*Adaptive time-stepping parameters*/
#define enableAdaptiveTimeStepping false //Flag to enable adaptive time
   steps
#define adaptiveLoadStepFactor 0.5 // Load step factor
#define adaptiveLoadIncreaseFactor 1.25
#define succesiveIncForIncreasingTimeStep 10

//Elastic Parameters

double elasticStiffness[6][6]={{97.7e3, 82.7e3, 82.7e3, 0, 0, 0},
          {82.7e3, 97.7e3, 82.7e3, 0, 0, 0},
```

```
        {82.7e3, 82.7e3, 97.7e3, 0, 0, 0},
        {0, 0, 0, 37.5e3, 0, 0},
        {0, 0, 0, 0, 37.5e3, 0},
        {0, 0, 0, 0, 0, 37.5e3}}; //   Elastic Stiffness Matrix -Voigt
   Notation (MPa)


//Crystal Plasticity parameters

#define numSlipSystems 12 //
#define latentHardeningRatio 1.4  //q1

double initialSlipResistance[numSlipSystems]= {200.0, 200.0, 200.0, 200.0,
   200.0, 200.0, 200.0, 200.0, 200.0, 200.0, 200.0, 200.0};  //CRSS of
   slip sytems
double initialHardeningModulus[numSlipSystems]= {1500.0, 1500.0, 1500.0,
   1500.0, 1500.0, 1500.0, 1500.0, 1500.0, 1500.0, 1500.0, 1500.0,
   1500.0}; //Hardening moduli of slip systems
double powerLawExponent[numSlipSystems]= {1.0, 1.0, 1.0, 1.0, 1.0, 1.0,
   1.0, 1.0, 1.0, 1.0, 1.0, 1.0}; // Power law coefficient
double saturationStress[numSlipSystems]= {500.0, 500.0, 500.0, 500.0,
   500.0, 500.0, 500.0, 500.0, 500.0, 500.0, 500.0, 500.0}; // Saturation
   stress


//Slip systems files
#define slipDirectionsFile "slipDirections.txt" // Slip Directions File
#define slipNormalsFile "slipNormals.txt" // Slip Normals File
```

```
// Crystal Plasticity Constitutive model parameters

#define modelStressTolerance 1.0e-6 // Stress tolerance for the yield surface (MPa)
#define modelMaxSlipSearchIterations 20 // Maximum no. of active slip search iterations
#define modelMaxSolverIterations 10 // Maximum no. of iterations to achieve non-linear convergence
#define modelMaxPlasticSlipL2Norm 0.8 // L2-Norm of plastic slip strain-used for load-step adaptivity
#define adaptiveLoadStepFactor 0.5 // Load step factor

//Read Input Microstructure
unsigned int numPts[3]={20, 20, 22}; // No. of voxels in x,y and z directions
#define grainIDFile "grainID.txt" // Grain ID File
#define headerLinesGrainIDFile 5 // No. of header Lines
#define grainOrientationsFile "orientations.txt" // Slip Normals File
```

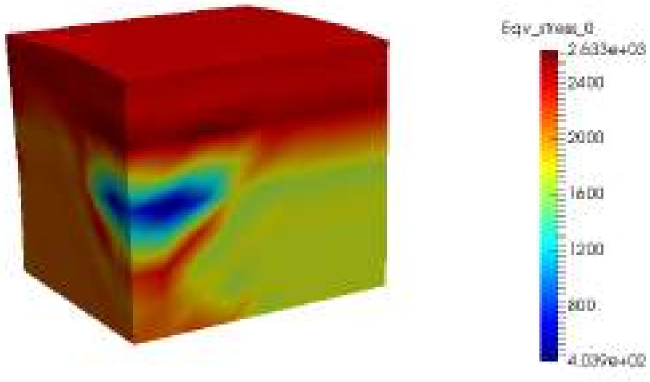

Figure C.2: Equivalent Von-Mises Stress shown on a deformation field

Table C.1: BCC Titanium Slip Systems

System Number	Slip Direction	Slip Plane
1	[1 -1 1]	(0 1 1)
2	[1 1 -1]	(0 1 1)
3	[-1 1 1]	(1 0 1)
4	[1 1 -1]	(1 0 1)
5	[-1 1 1]	(1 1 0)
6	[1 -1 1]	(1 1 0)
7	[1 1 1]	(0 -1 1)
8	[-1 1 1]	(0 -1 1)
9	[1 1 1]	(1 0 -1)
10	[1 -1 1]	(1 0 -1)
11	[1 1 1]	(-1 1 0)
12	[1 1 -1]	(-1 1 0)
13	[1 1 -1]	(1 1 2)
14	[1 -1 1]	(-1 1 2)
15	[-1 1 1]	(1 -1 2)
16	[1 1 1]	(1 1 -2)
17	[1 -1 1]	(1 2 1)
18	[1 1 -1]	(-1 2 1)
19	[1 1 1]	(1 -2 1)
20	[-1 1 1]	(1 2 -1)
21	[-1 1 1]	(2 1 1)
22	[1 1 1]	(-2 1 1)
23	[1 1 -1]	(2 -1 1)
24	[1 -1 1]	(2 1 -1)
25	[1 1 -1]	(1 2 3)
26	[1 -1 1]	(-1 2 3)
27	[-1 1 1]	(1 -2 3)
28	[1 1 1]	(1 2 -3)
29	[-1 1 1]	(3 1 2)
30	[1 1 1]	(-3 1 2)
31	[1 1 -1]	(3 -1 2)
32	[1 -1 1]	(3 1 -2)
33	[1 -1 1]	(2 3 1)
34	[1 1 -1]	(-2 3 1)
35	[1 1 1]	(2 -3 1)
36	[-1 1 1]	(2 3 -1)
37	[1 -1 1]	(1 3 2)
38	[1 1 -1]	(-1 3 2)
39	[1 1 1]	(1 -3 2)
40	[-1 1 1]	(1 3 -2)
41	[1 1 -1]	(2 1 3)
42	[1 -1 1]	(-2 1 3)
43	[-1 1 1]	(2 -1 3)
44	[1 1 1]	(2 1 -3)
45	[-1 1 1]	(3 2 1)
46	[1 1 1]	(-3 2 1)
47	[1 1 -1]	(3 -2 1)
48	[1 -1 1]	(3 2 -1)

APPENDIX D

PRISMS-Plasticity: Simple tension example -HCP AZ31 Mg alloy

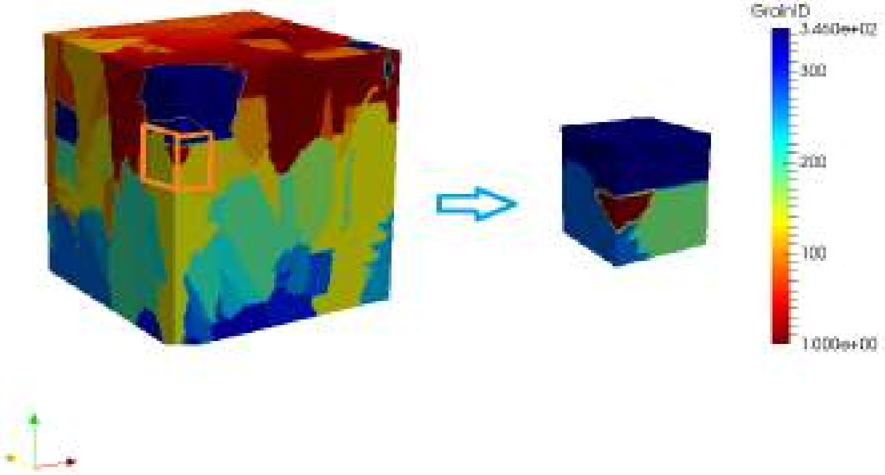

Figure D.1: Input microstructure (3D Materials Atlas

This is an illustrative example of a simple tension deformation problem. A real microstructure was tested with the hcp material parameters of AZ31 Mg alloy which were obtained from [35]

Input Parameters

```
/*FE parameters*/
#define feOrder   1 // Basis function interpolation order (1-linear)
#define quadOrder 2 // Quadrature point order n^3 (2->8 quadrature points)

/*Mesh parameters*/
//Set the length of the domain in all three dimensions
//Each axes spans from zero to the specified length
#define spanX 1.0
#define spanY 1.0
#define spanZ 1.0
// The number of elements in each direction is 2^(refineFactor) *
   subdivisions
// For optimal performance, use meshRefineFactor primarily to determine
   the element size
#define subdivisionsX 1
#define subdivisionsY 1
#define subdivisionsZ 1
#define meshRefineFactor 3 // 2^n*2^n*2^n elements(3->8*8*8 =512 elements)
#define writeMeshToEPS  true //Only written for serial runs and if number
   of elements < 10000

/*Solution output parameters*/
#define writeOutput true // flag to write output vtu and pvtu files
#define outputDirectory "."
#define skipOutputSteps 0
#define output_Eqv_strain true
```

```
#define output_Eqv_stress true
#define output_Grain_ID   true
#define output_Twin true

/*Solver parameters*/
#define linearSolverType PETScWrappers::SolverCG // Type of linear solver
#define totalNumIncrements 100 // No. of increments
#define maxLinearSolverIterations 50000 // Maximum iterations for linear
   solver
#define relLinearSolverTolerance  1.0e-10 // Relative linear solver
   tolerance
#define maxNonLinearIterations 4 // Maximum no. of non-linear iterations
#define absNonLinearTolerance 1.0e-18 // Non-linear solver tolerance
#define relNonLinearTolerance 1.0e-3 // Relative non-linear solver
   tolerance
#define stopOnConvergenceFailure false // Flag to stop problem if
   convergence fails

/*Adaptive time-stepping parameters*/
#define enableAdaptiveTimeStepping false //Flag to enable adaptive time
   steps
#define adaptiveLoadStepFactor 0.5 // Load step factor
#define adaptiveLoadIncreaseFactor 1.25
#define succesiveIncForIncreasingTimeStep 10

//Elastic Parameters
double elasticStiffness[6][6]={{59.3e3, 25.7e3, 21.4e3, 0, 0, 0},
           {25.7e3, 59.3e3, 21.4e3, 0, 0, 0},
           {21.4e3, 21.4e3, 61.5e3, 0, 0, 0},
```

```
          {0, 0, 0, 16.4e3, 0, 0},
          {0, 0, 0, 0, 16.4e3, 0},
          {0, 0, 0, 0, 0, 16.8e3}}; //   Elastic Stiffness Matrix -Voigt
   Notation (MPa)


//Crystal Plasticity
//slip parameters
#define numSlipSystems 18 // Total No. of slip systems (slip)
#define latentHardeningRatio 1.4  //q1

double initialSlipResistance[numSlipSystems]= {25.0, 25.0, 25.0, 68.0,
   68.0, 68.0, 68.0, 68.0, 68.0, 68.0, 68.0, 68.0, 68.0, 68.0, 68.0,
   68.0, 68.0, 68.0}; //CRSS of slip sytems
double initialHardeningModulus[numSlipSystems]= {100.0, 100.0, 100.0,
   130.0, 130.0, 130.0, 130.0, 130.0, 130.0, 130.0, 130.0, 130.0, 130.0,
   130.0, 130.0, 130.0, 130.0, 130.0}; //Hardening moduli of slip systems
double powerLawExponent[numSlipSystems]= {1.1, 1.1, 1.1, 0.8, 0.8, 0.8,
   0.8, 0.8, 0.8, 0.8, 0.8, 0.8, 0.8, 0.8, 0.8, 0.8, 0.8, 0.8}; // Power
   law coefficient
double saturationStress[numSlipSystems]= {70.0, 70.0, 70.0, 210.0, 210.0,
   210.0, 210.0, 210.0, 210.0, 210.0, 210.0, 210.0, 210.0, 210.0, 210.0,
   210.0, 210.0, 210.0}; // Saturation stress

//Twin parameters

#define numTwinSystems 6 // No. of twin systems
```

```
double initialSlipResistanceTwin[numTwinSystems]= {40.0, 40.0, 40.0, 40.0, 40.0, 40.0}; //CRSS of twin sytems
double initialHardeningModulusTwin[numTwinSystems]= {50.0, 50.0, 50.0, 50.0, 50.0, 50.0}; //Hardening moduli of twin systems
double powerLawExponentTwin[numTwinSystems]= {1.1, 1.1, 1.1, 1.1, 1.1, 1.1};// Power law coefficient
double saturationStressTwin[numTwinSystems]= {50.0, 50.0, 50.0, 50.0, 50.0, 50.0}; // Saturation stress

#define twinThresholdFraction 0.25 // threshold fraction of characteristic twin shear (<1)
#define twinSaturationFactor 0.25 // twin growth saturation factor (<(1-twinThresholdFraction))
#define twinShear 0.129 // characteristic twin shear


//Slip systems files
#define slipDirectionsFile "slipDirections.txt" // Slip Directions File
#define slipNormalsFile "slipNormals.txt" // Slip Normals File

//Twin systems files
#define twinDirectionsFile "twinDirections.txt" // Slip Directions File
#define twinNormalsFile "twinNormals.txt" // Slip Normals File



// Crystal Plasticity Constitutive model parameters
```

```
#define modelStressTolerance 1.0e-1 // Stress tolerance for the yield
   surface (MPa)
#define modelMaxSlipSearchIterations 1 // Maximum no. of active slip
   search iterations
#define modelMaxSolverIterations 3 // Maximum no. of iterations to achieve
   non-linear convergence
#define modelMaxPlasticSlipL2Norm 2.5 // L2-Norm of plastic slip
   strain-used for load-step adaptivity




//Read Input Microstructure
unsigned int numPts[3]={20, 20, 22}; // No. of voxels in x,y and z
   directions
#define grainIDFile "grainID.txt" // Grain ID File
#define headerLinesGrainIDFile 5 // No. of header Lines
#define grainOrientationsFile "orientations.txt" // Slip Normals File
```

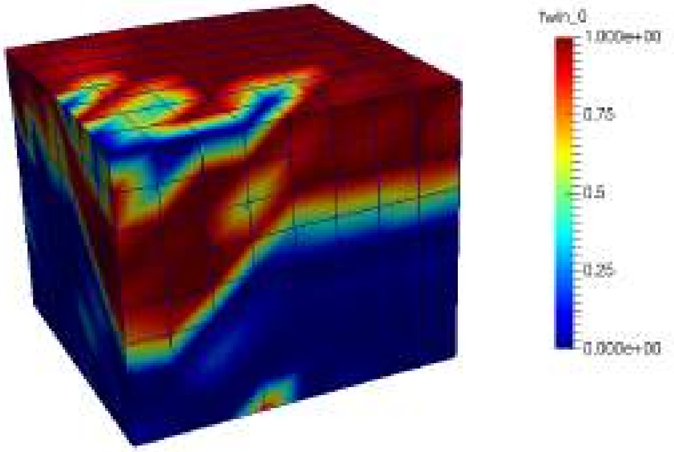

Figure D.2: Twinned region(0-no twin, 1-twin) shown on a deformation field

Table D.1: HCP Magnesium Slip Systems

System Number	Slip Direction	Slip Plane
1	[1 1 -2 0]	(0 0 0 1)
2	[-2 1 1 0]	(0 0 0 1)
3	[1 -2 1 0]	(0 0 0 1)
4	[1 -2 1 0]	(1 0 -1 0)
5	[2 -1 -1 0]	(0 1 -1 0)
6	[1 1 -2 0]	(-1 1 0 0)
7	[1 -2 1 0]	(1 0 -1 1)
8	[-2 1 1 0]	(0 1 -1 1)
9	[-1 -1 2 0]	(-1 1 0 1)
10	[-1 2 -1 0]	(-1 0 1 1)
11	[2 -1 -1 0]	(0 -1 1 1)
12	[1 1 -2 0]	(1 -1 0 1)
13	[-1 -1 2 3]	(1 1 -2 2)
14	[1 -2 1 3]	(-1 2 -1 2)
15	[2 -1 -1 3]	(-2 1 1 2)
16	[1 1 -2 3]	(-1 -1 2 2)
17	[-1 2 -1 3]	(1 -2 1 2)
18	[-2 1 1 3]	(2 -1 -1 2)
19	[-1 0 1 1]	(1 0 -1 2)
20	[1 0 -1 1]	(-1 0 1 2)
21	[-1 1 0 1]	(1 -1 0 2)
22	[1 -1 0 1]	(-1 1 0 2)
23	[0 -1 1 1 1]	(0 1 -1 2)
24	[0 1 -1 1]	(0 -1 1 2)

APPENDIX E

Run-time log of PRISMS-Plasticity code

```
reading voxel data file
reading orientation euler angles file
generating problem mesh
number of MPI processes: 240
number of elements: 1000000
number of degrees of freedom: 3090903
begin solve...


increment: 0
nonlinear iteration   0 [current residual: 2.78e+04, initial residual:
   2.78e+04, relative residual: 1.00e+00]
linear system solved in 413 iterations
nonlinear iteration   1 [current residual: 1.85e-01, initial residual:
   2.78e+04, relative residual: 6.68e-06]
linear system solved in 991 iterations
nonlinear iteration   2 [current residual: 2.88e-04, initial residual:
   2.78e+04, relative residual: 1.04e-08]
```

```
linear system solved in 915 iterations
nonlinear iteration   3 [current residual: 1.65e-08, initial residual:
   2.78e+04, relative residual: 5.93e-13]
nonlinear iterations converged in relative norm
writing orientations data to file
projecting post processing fields
linear system solved in  45 iterations
linear system solved in  45 iterations
linear system solved in  45 iterations
linear system solved in   0 iterations
output written to: .//solution-0000.pvtu and .//projectedFields-0000.pvtu

. . .
. . .
. . .

increment: 100
nonlinear iteration   0 [current residual: 2.70e+04, initial residual:
   2.70e+04, relative residual: 1.00e+00]
linear system solved in 500 iterations
nonlinear iteration   1 [current residual: 3.17e+02, initial residual:
   2.70e+04, relative residual: 1.17e-02]
linear system solved in 1382 iterations
nonlinear iteration   2 [current residual: 1.69e+02, initial residual:
   2.70e+04, relative residual: 6.25e-03]
linear system solved in 538 iterations
nonlinear iteration   3 [current residual: 1.26e+02, initial residual:
   2.70e+04, relative residual: 4.64e-03]
linear system solved in 542 iterations
```

```
nonlinear iteration   4 [current residual: 1.04e+02, initial residual:
   2.70e+04, relative residual: 3.85e-03]
linear system solved in 1136 iterations
nonlinear iterations did not converge in maxNonLinearIterations
stopOnConvergenceFailure==false, so marching ahead

. . .
. . .
. . .


increment: 200
nonlinear iteration   0 [current residual: 2.40e+04, initial residual:
   2.40e+04, relative residual: 1.00e+00]
linear system solved in 629 iterations
nonlinear iteration   1 [current residual: 3.42e+02, initial residual:
   2.40e+04, relative residual: 1.42e-02]
linear system solved in 1544 iterations
nonlinear iteration   2 [current residual: 3.98e+02, initial residual:
   2.40e+04, relative residual: 1.65e-02]
linear system solved in 1521 iterations
nonlinear iteration   3 [current residual: 3.18e+02, initial residual:
   2.40e+04, relative residual: 1.32e-02]
linear system solved in 828 iterations
nonlinear iteration   4 [current residual: 1.94e+02, initial residual:
   2.40e+04, relative residual: 8.07e-03]
linear system solved in 840 iterations
nonlinear iterations did not converge in maxNonLinearIterations
stopOnConvergenceFailure==false, so marching ahead
```

```
. . .
. . .
. . .

increment: 499
nonlinear iteration   0 [current residual: 2.41e+04, initial residual:
   2.41e+04, relative residual: 1.00e+00]
linear system solved in 645 iterations
nonlinear iteration   1 [current residual: 3.49e+02, initial residual:
   2.41e+04, relative residual: 1.45e-02]
linear system solved in 1896 iterations
nonlinear iteration   2 [current residual: 7.23e+02, initial residual:
   2.41e+04, relative residual: 3.00e-02]
linear system solved in 900 iterations
nonlinear iteration   3 [current residual: 2.97e+02, initial residual:
   2.41e+04, relative residual: 1.23e-02]
linear system solved in 1192 iterations
nonlinear iteration   4 [current residual: 7.72e+01, initial residual:
   2.41e+04, relative residual: 3.20e-03]
linear system solved in 2211 iterations
nonlinear iterations did not converge in maxNonLinearIterations
stopOnConvergenceFailure==false, so marching ahead
writing orientations data to file
projecting post processing fields
linear system solved in  50 iterations
linear system solved in  48 iterations
linear system solved in  45 iterations
linear system solved in  60 iterations
```

```
output written to: .//solution-0499.pvtu and .//projectedFields-0499.pvtu




+---------------------------------------------+------------+------------+
| Total wallclock time elapsed since start    |  1.13e+05s |            |
|                                             |            |            |
| Section                         | no. calls |  wall time | % of total |
+---------------------------------+-----------+------------+------------+
| assembly                        |      2490 |  9.65e+04s |        85% |
| mesh and initialization         |         1 |      92.2s |     0.082% |
| postprocess                     |       500 |      8.52s |    0.0075% |
| solve                           |      2475 |  1.45e+04s |        13% |
+---------------------------------+-----------+------------+------------+
```

APPENDIX F

Constitutive model of PRISMS-Plasticity code

```
template <int dim>
void crystalPlasticity<dim>::calculatePlasticity(unsigned int cellID,
                                                 unsigned int quadPtID)
{

    F_tau=F; // Deformation Gradient
    FullMatrix<double> FE_t(dim,dim),FP_t(dim,dim);  //Elastic and Plastic
   deformation gradient
    Vector<double> s_alpha_t(n_slip_systems); // Slip resistance
    Vector<double> rot1(dim);// Crystal orientation (Rodrigues
   representation)

    int old_precision = std::cout.precision();

    // Tolerance

    double tol1=modelStressTolerance;
```

```
std::cout.precision(16);


FE_t=Fe_conv[cellID][quadPtID];

FP_t=Fp_conv[cellID][quadPtID];

s_alpha_t=s_alpha_conv[cellID][quadPtID];

rot1=rot[cellID][quadPtID];


// Rotation matrix of the crystal orientation

FullMatrix<double> rotmat(dim,dim);

rotmat=0.0;

odfpoint(rotmat,rot1);



FullMatrix<double> temp(dim,dim),temp1(dim,dim),temp2(dim,dim),

temp3(dim,dim),temp4(dim,dim),temp5(dim,dim),temp6(dim,dim); //
Temporary matrices

FullMatrix<double> T_tau(dim,dim),P_tau(dim,dim);

FullMatrix<double>
Fpn_inv(dim,dim),FE_tau_trial(dim,dim),F_trial(dim,dim),

CE_tau_trial(dim,dim),FP_t2(dim,dim),Ee_tau_trial(dim,dim);


//convert to crystal coordinates F_tau=R'*F_tau*R

temp=0.0;

rotmat.Tmmult(temp,F_tau);

temp.mmult(F_tau,rotmat);



// Calculation of Schmid Tensors  and B=
symm(FE_tau_trial'*FE_tau_trial*S_alpha)
```

```
FullMatrix<double> SCHMID_TENSOR1(n_slip_systems*dim,dim),
B(n_slip_systems*dim,dim);
Vector<double> m1(dim),n1(dim);

for(unsigned int i=0;i<n_slip_systems;i++){
    for (unsigned int j=0;j<dim;j++){
        m1(j)=m_alpha[i][j];
        n1(j)=n_alpha[i][j];
    }

    for (unsigned int j=0;j<dim;j++){
        for (unsigned int k=0;k<dim;k++){
            temp[j][k]=m1(j)*n1(k);
            SCHMID_TENSOR1[dim*i+j][k]=m1(j)*n1(k);
        }
    }

    CE_tau_trial.mmult(temp2,temp);
    temp2.symmetrize();
    for (unsigned int j=0;j<dim;j++){
        for (unsigned int k=0;k<dim;k++){
            B[dim*i+j][k]=2*temp2[j][k];
        }
    }
}

// Elastic Modulus

FullMatrix<double> Dmat2(2*dim,2*dim),TM(dim*dim,dim*dim);
```

```
Vector<double> vec1(2*dim),vec2(dim*dim);
for(unsigned int i=0;i<6;i++){
    for(unsigned int j=0;j<6;j++){
        Dmat2[i][j] = elasticStiffness[i][j];
    }
}
vec1(0)=0;vec1(1)=5;vec1(2)=4;vec1(3)=1;vec1(4)=3;vec1(5)=2;
vec2(0)=0;vec2(1)=5;vec2(2)=4;vec2(3)=5;vec2(4)=1;vec2(5)=3;
vec2(6)=4;vec2(7)=3;vec2(8)=2;
for(unsigned int i=0;i<9;i++){
    for(unsigned int j=0;j<9;j++){
        TM[i][j]=Dmat2(vec2(i),vec2(j));
    }
}

Vector<double> s_alpha_tau;
FP_tau=FP_t;
FE_tau.reinit(dim,dim);
Fpn_inv=0.0; Fpn_inv.invert(FP_t);
F_tau.mmult(FE_tau,Fpn_inv);
s_alpha_tau=s_alpha_t;

Vector<double> s_beta(n_slip_systems),h_beta(n_slip_systems),
delh_beta_dels(n_slip_systems),h0(n_slip_systems),
a_pow(n_slip_systems),s_s(n_slip_systems);
FullMatrix<double> h_alpha_beta_t(n_slip_systems,n_slip_systems),
A(n_slip_systems,n_slip_systems);
FullMatrix<double> del_FP(dim,dim);
FullMatrix<double> A_PA;
```

```
Vector<double> active;
Vector<double> PA, PA_temp(1);
Vector<double>
resolved_shear_tau_trial(n_slip_systems),b(n_slip_systems),
resolved_shear_tau(n_slip_systems);
Vector<double> x_beta_old(n_slip_systems);

Vector<double> x_beta(n_slip_systems);
FullMatrix<double> Ce_tau(dim,dim),T_star_tau(dim,dim);
FullMatrix<double> T_star_tau_trial(dim,dim),diff_FP(dim,dim);

delFp_delF=0.0;
dels_delF=0.0;

double det_FE_tau,det_F_tau, det_FP_tau;
int n_PA=0; // Number of active slip systems

int iter1=1;
int flag2=0;

while (iter1) {

    if(iter1>modelMaxSlipSearchIterations){
        flag2=1;
        break;
    }

    FP_t2=FP_tau;
    Fpn_inv=0.0; Fpn_inv.invert(FP_t2);
```

```
FE_tau_trial=0.0;
F_trial=0.0;
F_tau.mmult(FE_tau_trial,Fpn_inv);F_trial = FE_tau_trial;


temp.reinit(dim,dim); temp=0.0;
temp=FE_tau_trial;
FE_tau_trial.Tmmult(CE_tau_trial,temp);
Ee_tau_trial=CE_tau_trial;
temp=IdentityMatrix(dim);
for(unsigned int i=0;i<dim;i++){
    for(unsigned int j=0;j<dim;j++){
        Ee_tau_trial[i][j] = 0.5*(Ee_tau_trial[i][j]-temp[i][j]);
    }
}


//% % % % % STEP 2 % % % % %
// Calculate the trial stress T_star_tau_trial
Vector<double> tempv1(6),tempv2(6);
tempv1=0.0;
Dmat.vmult(tempv1, vecform(Ee_tau_trial));
matform(T_star_tau_trial,tempv1);
T_star_tau.equ(1.0,T_star_tau_trial);


det_FE_tau=FE_tau.determinant();
temp.reinit(dim,dim); FE_tau.mmult(temp,T_star_tau_trial);
temp.equ(1.0/det_FE_tau,temp); temp.mTmult(T_tau,FE_tau);
det_F_tau=F_tau.determinant();
temp2.reinit(dim,dim);
temp.invert(F_tau); T_tau.mTmult(temp2,temp);
```

```
    P_tau.equ(det_FE_tau,temp2);


    //% % % % % STEP 3 % % % % %
    // Calculate the trial resolved shear stress
resolved_shear_tau_trial for each slip system


    resolved_shear_tau_trial=0.0;
    CE_tau_trial.mmult(temp,T_star_tau_trial);
    n_PA=0; // Number of active slip systems
    resolved_shear_tau_trial=0.0;
    for(unsigned int i=0;i<n_slip_systems;i++){

        for (unsigned int j=0;j<dim;j++){
            for (unsigned int k=0;k<dim;k++){

resolved_shear_tau_trial(i)+=temp[j][k]*SCHMID_TENSOR1[dim*i+j][k];
            }
        }


        if(i>numSlipSystems-1){
            if(resolved_shear_tau_trial(i)<0)
                resolved_shear_tau_trial(i)=0;
        }


        //% % % % % STEP 4 % % % % %
        //Determine the set set of the n potentially active slip
systems
        b(i)=fabs(resolved_shear_tau_trial(i))-s_alpha_tau(i);
        if( b(i)>=tol1){
```

```
            if(n_PA==0){
                n_PA=n_PA+1;
                PA.reinit(n_PA);
                PA(0)=i;
            }
            else{
                PA_temp=PA;
                n_PA=n_PA+1;
                PA.reinit(n_PA);
                for (unsigned int j=0;j<(n_PA-1);j++){
                    PA(j)=PA_temp(j);
                }
                PA(n_PA-1)=i;
                PA_temp.reinit(n_PA);     //%%%%% Potentially active
slip systems
            }
        }
        //resolved_shear_tau(i)=(resolved_shear_tau_trial(i));
    }
     if(n_PA==0)
        break;
    //% % % % % STEP 5 % % % % %
    //Calculate the shear increments from the consistency condition
    s_beta=s_alpha_tau;

    // Single slip hardening rate
    for(unsigned int i=0;i<numSlipSystems;i++){
        h_beta(i)=initialHardeningModulus[i]
        *pow((1-s_beta(i)/saturationStress[i]),powerLawExponent[i]);
```

```
}

for(unsigned int i=0;i<numTwinSystems;i++){
    h_beta(numSlipSystems+i)=initialHardeningModulusTwin[i]
    *pow((1-s_beta(numSlipSystems+i)/saturationStressTwin[i]),
         powerLawExponentTwin[i]);
}


for(unsigned int i=0;i<n_slip_systems;i++){
    for(unsigned int j=0;j<n_slip_systems;j++){
        h_alpha_beta_t[i][j] = q[i][j]*h_beta(j);
        A[i][j]=h_alpha_beta_t[i][j];
    }
}

// Calculate the Stiffness Matrix A
for(unsigned int i=0;i<n_slip_systems;i++){
    for(unsigned int j=0;j<n_slip_systems;j++){
        temp1.reinit(dim,dim); temp1=0.0;

        for(unsigned int k=0;k<dim;k++){
            for(unsigned int l=0;l<dim;l++){
                temp[k][l]=SCHMID_TENSOR1(dim*j+k,l);
            }
        }
        temp2.reinit(dim,dim); CE_tau_trial.mmult(temp2,temp);
        temp2.symmetrize();
        tempv1=0.0; Dmat.vmult(tempv1, vecform(temp2));
```

```
            temp3=0.0; matform(temp3,tempv1);

            CE_tau_trial.mmult(temp1,temp3);
            temp3=0.0; temp2.mmult(temp3,T_star_tau_trial);

            temp1.add(2.0,temp3);

            for(unsigned int k=0;k<dim;k++){
                for(unsigned int l=0;l<dim;l++){

if((resolved_shear_tau_trial(i)<0.0)^(resolved_shear_tau_trial(j)<0.0))
                        A[i][j]-=SCHMID_TENSOR1(dim*i+k,l)*temp1[k][l];
                    else
                        A[i][j]+=SCHMID_TENSOR1(dim*i+k,l)*temp1[k][l];

                }
            }
        }
    }

    x_beta_old=0.0;

    int count1=0;

    Vector<double> b_PA(n_PA);

    for(unsigned int i=0;i<n_PA;i++){
        b_PA(i)=b(PA(i));
    }
```

```
    //bool x1=1;

    while((b_PA.linfty_norm())>tol1) {

        count1=count1+1;
        if(count1>modelMaxSolverIterations)
            break;

        x_beta=0.0;

        //Modified slip system search for adding corrective term
        // [x_beta] = INACTIVE_SLIP_REMOVAL(A,b,PA,x_beta_old);

inactive_slip_removal(active,x_beta_old,x_beta,n_PA,PA,b,A,A_PA);
        temp.reinit(dim,dim);
        del_FP.reinit(dim,dim);
        del_FP=0.0;
        for (unsigned int i=0;i<n_slip_systems;i++){
            for (unsigned int j=0;j<dim;j++){
                for (unsigned int k=0;k<dim;k++){
                    temp[j][k]=SCHMID_TENSOR1[dim*i+j][k];
                }
            }

            for (unsigned int j=0;j<dim;j++){
                for (unsigned int k=0;k<dim;k++){
                    if(resolved_shear_tau_trial(i)>0)
```

```
del_FP[j][k]=del_FP[j][k]+x_beta_old(i)*temp[j][k];
                    else

del_FP[j][k]=del_FP[j][k]-x_beta_old(i)*temp[j][k];
                }
            }

        }

        matrixExponential(del_FP).mmult(FP_tau,FP_t2);

        // % % % % % STEP 8 % % % % %
        temp.invert(FP_tau);
        F_tau.mmult(FE_tau,temp);
        FE_tau.Tmmult(Ce_tau,FE_tau);
        Ee_tau_trial=Ce_tau;
        temp=IdentityMatrix(dim);
        for(unsigned int i=0;i<dim;i++){
            for(unsigned int j=0;j<dim;j++){
                Ee_tau_trial[i][j] =
0.5*(Ee_tau_trial[i][j]-temp[i][j]);
            }
        }

        Dmat.vmult(tempv1, vecform(Ee_tau_trial));
        matform(T_star_tau,tempv1);
        resolved_shear_tau=0.0;
        Ce_tau.mmult(temp,T_star_tau);
        for(unsigned int i=0;i<n_slip_systems;i++){
```

```
                for (unsigned int j=0;j<dim;j++){
                    for (unsigned int k=0;k<dim;k++){

resolved_shear_tau(i)+=temp[j][k]*SCHMID_TENSOR1[dim*i+j][k];
                    }
                }
            }



            // % % % % % STEP 9 % % % % %


            temp.reinit(dim,dim);
            det_FE_tau=FE_tau.determinant();
            FE_tau.mmult(temp,T_star_tau); temp.equ(1.0/det_FE_tau,temp);
            temp.mTmult(T_tau,FE_tau);

            det_F_tau=F_tau.determinant();
            temp.invert(F_tau); T_tau.mTmult(P_tau,temp);
            P_tau.equ(det_F_tau,P_tau);

             double h1=0;
            for(unsigned int i=0;i<n_slip_systems;i++){
                h1=0;
                for(unsigned int j=0;j<n_slip_systems;j++){
                    h1=h1+h_alpha_beta_t(i,j)*x_beta(j);
                }
                s_alpha_tau(i)=s_alpha_tau(i)+h1;
            }
```

```
        for (unsigned int i=0;i<numSlipSystems;i++){


            if(s_alpha_tau(i)>saturationStress[i])

                s_alpha_tau(i)=0.90*saturationStress[i];


        }


        for (unsigned int i=0;i<numTwinSystems;i++){


            if(s_alpha_tau(numSlipSystems+i)>saturationStressTwin[i])


s_alpha_tau(numSlipSystems+i)=0.90*saturationStressTwin[i];


        }




        for(unsigned int i=0;i<n_slip_systems;i++){

            if((resolved_shear_tau_trial(i)>0.0))

                b(i)=resolved_shear_tau(i)-s_alpha_tau(i);

            else

                b(i)=-resolved_shear_tau(i)-s_alpha_tau(i);

        }


        b_PA.reinit(n_PA);


        for(unsigned int i=0;i<n_PA;i++){

            b_PA(i)=b(PA(i));

        }

        bool x1=(b_PA.linfty_norm())>tol1;
```

```
        }

        for (unsigned int i=0;i<numTwinSystems;i++){

   twinfraction_iter[cellID][quadPtID][i]=twinfraction_conv[cellID][quadPtID][i]
            +x_beta_old[i+numSlipSystems]/twinShear;
        }

        for (unsigned int i=0;i<numSlipSystems;i++){

   slipfraction_iter[cellID][quadPtID][i]=slipfraction_conv[cellID][quadPtID][i]
            +x_beta_old[i]/twinShear;
        }

    P.reinit(dim,dim);
    P=P_tau;
    T=T_tau;


    sres_tau.reinit(n_slip_systems);
    sres_tau = s_alpha_tau;

    // Update the history variables
    Fe_iter[cellID][quadPtID]=FE_tau;
    Fp_iter[cellID][quadPtID]=FP_tau;
    s_alpha_iter[cellID][quadPtID]=sres_tau;

    }
}
```

BIBLIOGRAPHY

BIBLIOGRAPHY

[1] Acar, P., and V. Sundararaghavan (2016), Utilization of a linear solver for multiscale design and optimization of microstructures, *AIAA Journal*, *54*(5), 1751 – 1759.

[2] Acar, P., and V. Sundararaghavan (2016), Linear solution scheme for microstructure design with process constraints, *AIAA Journal*, *54*(12), 4022 – 4031.

[3] Acar, P., and V. Sundararaghavan (2016), A markov random field approach for modeling spatio-temporal evolution of microstructures, *Modelling and Simulation in Materials Science and Engineering*, *24*(7), 075,005.

[4] Acar, P., and V. Sundararaghavan (2017), Uncertainty quantification of microstructural properties due to variability in measured pole figures, *Acta Materialia*, *124*, 100 – 108.

[5] Aghion, E., and B. Bronfin (2000), Magnesium alloys development towards the 21st century, in *Materials Science Forum*, vol. 350, pp. 19–30, Trans Tech Publ.

[6] Agnew, S. R. (2004), Wrought magnesium: A 21st century outlook, *Jom*, *56*(5), 20–21.

[7] Agnew, S. R., and Ö. Duygulu (2005), Plastic anisotropy and the role of non-basal slip in magnesium alloy AZ31B, *International Journal of plasticity*, *21*(6), 1161–1193.

[8] Ahrens, J., B. Geveci, C. Law, C. Hansen, and C. Johnson (2005), ParaView: An End-User Tool for Large-Data Visualization, *The Visualization Handbook*, p. 717.

[9] Allison, J., D. Backman, and L. Christodoulou (2006), Integrated computational materials engineering: a new paradigm for the global materials profession, *JOM Journal of the Minerals, Metals and Materials Society*, *58*(11), 25–27.

[10] Aloupis, G., H. Pérez-Rosés, G. Pineda-Villavicencio, P. Taslakian, and D. Trinchet-Almaguer (2013), Fitting voronoi diagrams to planar tesselations, in *International Workshop on Combinatorial Algorithms*, pp. 349–361, Springer.

[11] Anand, L. (1985), Constitutive equations for hot-working of metals, *International Journal of Plasticity*, *1*(3), 213–231.

[12] Anand, L., and M. Kothari (1996), A computational procedure for rate-independent crystal plasticity, *Journal of the Mechanics and Physics of Solids*, *44*(4), 525–558.

[13] Ash, P. F., and E. D. Bolker (1985), Recognizing dirichlet tessellations, *Geometriae Dedicata*, *19*(2), 175–206.

[14] Aurenhammer, F. (1987), Recognising polytopical cell complexes and constructing projection polyhedra, *Journal of Symbolic Computation*, *3*(3), 249–255.

[15] Bachmann, F., R. Hielscher, and H. Schaeben (2010), Texture analysis with MTEX–free and open source software toolbox, in *Solid State Phenomena*, vol. 160, pp. 63–68, Trans Tech Publ.

[16] Banerjee, S., B. B. Bhattacharya, S. Das, A. Karmakar, A. Maheshwari, and S. Roy (2013), On the Construction of Generalized Voronoi Inverse of a Rectangular Tessellation, in *Transactions on Computational Science XX*, pp. 22–38, Springer.

[17] Bangerth, W., R. Hartmann, and G. Kanschat (2007), deal. ii—a general-purpose object-oriented finite element library, *ACM Transactions on Mathematical Software (TOMS)*, *33*(4), 24.

[18] Barber, C. B., D. P. Dobkin, and H. Huhdanpaa (1996), The quickhull algorithm for convex hulls, *ACM Transactions on Mathematical Software (TOMS)*, *22*(4), 469–483.

[19] Barnett, M., N. Stanford, P. Cizek, A. Beer, Z. Xuebin, and Z. Keshavarz (2009), Deformation mechanisms in Mg alloys and the challenge of extending room-temperature plasticity, *JOM Journal of the Minerals, Metals and Materials Society*, *61*(8), 19–24.

[20] Beaudoin Jr, A., H. Mecking, and U. Kocks (1996), Development of localized orientation gradients in fcc polycrystals, *Philosophical Magazine A*, *73*(6), 1503–1517.

[21] Becker, R., and S. Panchanadeeswaran (1995), Effects of grain interactions on deformation and local texture in polycrystals, *Acta Metallurgica et Materialia*, *43*(7), 2701–2719.

[22] Bhattacharyya, A., E. El-Danaf, S. R. Kalidindi, and R. D. Doherty (2001), Evolution of grain-scale microstructure during large strain simple compression of polycrystalline aluminum with quasi-columnar grains: OIM measurements and numerical simulations, *International Journal of Plasticity*, *17*(6), 861–883.

[23] Bhattacharyya, J., F. Wang, P. Wu, W. Whittington, H. El Kadiri, and S. Agnew (2016), Demonstration of alloying, thermal activation, and latent hardening effects on quasi-static and dynamic polycrystal plasticity of Mg alloy, WE43-T5, plate, *International Journal of Plasticity*, *81*, 123–151.

[24] Bishop, J., and R. Hill (1951), XLVI. A theory of the plastic distortion of a polycrystalline aggregate under combined stresses, *The London, Edinburgh, and Dublin Philosophical Magazine and Journal of Science*, *42*(327), 414–427.

[25] Boots, B., and D. Murdoch (1983), The spatial arrangement of random Voronoi polygons, *Computers & Geosciences*, *9*(3), 351–365.

[26] Brahme, A., M. Alvi, D. Saylor, J. Fridy, and A. Rollett (2006), 3D reconstruction of microstructure in a commercial purity aluminum, *Scripta Materialia*, *55*(1), 75–80.

[27] Bronkhorst, C., S. Kalidindi, and L. Anand (1992), Polycrystalline plasticity and the evolution of crystallographic texture in FCC metals, *Philosophical Transactions of the Royal Society of London A: Mathematical, Physical and Engineering Sciences*, *341*(1662), 443–477.

[28] Burke, E., and W. Hibbard (1951), *The plastic deformation of magnesium single crystals*, publisher not identified.

[29] Cermelli, P., and M. E. Gurtin (2001), On the characterization of geometrically necessary dislocations in finite plasticity, *Journal of the Mechanics and Physics of Solids*, *49*(7), 1539–1568.

[30] Chazelle, B. (1984), Convex partitions of polyhedra: a lower bound and worst-case optimal algorithm, *SIAM Journal on Computing*, *13*(3), 488–507.

[31] Cheng, J., and S. Ghosh (2015), A crystal plasticity FE model for deformation with twin nucleation in magnesium alloys, *International Journal of Plasticity*, *67*, 148–170.

[32] Chester, R., and I. Polmear (1983), The metallurgy of light alloys, *Institution of Metallurgists, London*, p. 75.

[33] Childs, H. (2013), VisIt: An end-user tool for visualizing and analyzing very large data.

[34] Chin, G., and W. Mammel (1970), Competition among basal, prism, and pyramidal slip modes in hcp metals, *Metallurgical and Materials Transactions B*, *1*(2), 357–361.

[35] Choi, S.-H., D. Kim, S. S. Park, and B. You (2010), Simulation of stress concentration in Mg alloys using the crystal plasticity finite element method, *Acta Materialia*, *58*(1), 320–329.

[36] Christian, J. W., and S. Mahajan (1995), Deformation twinning, *Progress in materials science*, *39*(1-2), 1–157.

[37] Eberl, F., S. Forest, G. Cailletaud, T. Wroblewski, and J. Lebrun (2002), Finite-element calculations of the lattice rotation field of a tensile-loaded nickel-based alloy multicrystal and comparison with topographical X-ray diffraction measurements, *Metallurgical and Materials Transactions A*, *33*(9), 2825–2833.

[38] Erieau, P., and C. Rey (2004), Modeling of deformation and rotation bands and of deformation induced grain boundaries in IF steel aggregate during large plane strain compression, *International Journal of Plasticity*, *20*(10), 1763–1788.

[39] Escoda, J., D. Jeulin, F. Willot, and C. Toulemonde (2015), Three-dimensional morphological modelling of concrete using multiscale Poisson polyhedra, *Journal of microscopy*, *258*(1), 31–48.

[40] Evans, D. G., and S. M. Jones (1987), Detecting Voronoi (area-of-influence) polygons, *Mathematical geology*, *19*(6), 523–537.

[41] Forest, S. (1998), Modeling slip, kink and shear banding in classical and generalized single crystal plasticity, *Acta Materialia*, *46*(9), 3265–3281.

[42] Fu, X., H. Poulsen, S. Schmidt, S. F. Nielsen, E. Lauridsen, and D. J. Jensen (2003), Non-destructive mapping of grains in three dimensions, *Scripta materialia*, *49*(11), 1093–1096.

[43] Ganesan, S., and V. Sundararaghavan (2015), An atomistically-informed energy based theory of environmentally assisted failure, *Corrosion Reviews*, *33*(6), 455 – 466.

[44] Ghosh, S., A. Kumar, V. Sundararaghavan, and A. M. Waas (2013), Non-local modeling of epoxy using an atomistically-informed kernel, *International Journal of Solids and Structures*, *50*(19), 2837 – 2845.

[45] Ghosh, S., V. Sundararaghavan, and A. M. Waas (2014), Construction of multi-dimensional isotropic kernels for nonlocal elasticity based on phonon dispersion data, *International Journal of Solids and Structures*, *51*(2), 392 – 401.

[46] Githens, A. S. (2015), Deformation Mechanisms of Magnesium Alloy WE43 under Monotonic Tensile Loading.

[47] Green, P. J., and R. Sibson (1978), Computing Dirichlet tessellations in the plane, *The Computer Journal*, *21*(2), 168–173.

[48] Groeber, M., S. Ghosh, M. D. Uchic, and D. M. Dimiduk (2008), A framework for automated analysis and simulation of 3D polycrystalline microstructures.: Part 1: Statistical characterization, *Acta Materialia*, *56*(6), 1257–1273.

[49] Groeber, M., S. Ghosh, M. D. Uchic, and D. M. Dimiduk (2008), A framework for automated analysis and simulation of 3D polycrystalline microstructures. Part 2: Synthetic structure generation, *Acta Materialia*, *56*(6), 1274–1287.

[50] Groeber, M. A., and M. A. Jackson (2014), DREAM. 3D: a digital representation environment for the analysis of microstructure in 3D, *Integrating Materials and Manufacturing Innovation*, *3*(1), 5.

[51] Gurtin, M. E. (2006), The Burgers vector and the flow of screw and edge dislocations in finite-deformation single-crystal plasticity, *Journal of the Mechanics and Physics of Solids*, *54*(9), 1882–1898.

[52] Gurtin, M. E., and L. Anand (2009), Thermodynamics applied to gradient theories involving the accumulated plastic strain: the theories of Aifantis and Fleck and Hutchinson and their generalization, *Journal of the Mechanics and Physics of Solids*, *57*(3), 405–421.

[53] Gurtin, M. E., E. Fried, and L. Anand (2010), *The mechanics and thermodynamics of continua*, Cambridge University Press.

[54] Hantzsche, K., J. Bohlen, J. Wendt, K. Kainer, S. Yi, and D. Letzig (2010), Effect of rare earth additions on microstructure and texture development of magnesium alloy sheets, *Scripta Materialia*, *63*(7), 725–730.

[55] Harren, S., and R. Asaro (1989), Nonuniform deformations in polycrystals and aspects of the validity of the Taylor model, *Journal of the Mechanics and Physics of Solids*, *37*(2), 191–232.

[56] Hartvigsen, D. (1992), Recognizing Voronoi diagrams with linear programming, *ORSA Journal on Computing*, *4*(4), 369–374.

[57] Hearmon, R. (1984), The elastic constants of crystals and other anisotropic materials, *Landolt-Börnstein Tables*, *3*(18), 559.

[58] Heilbronner, R., and N. Keulen (2006), Grain size and grain shape analysis of fault rocks, *Tectonophysics*, *427*(1), 199–216.

[59] Kelley, E., and W. Hosford (1968), The deformation characteristics of textured magnesium, *Trans Met Soc AIME*, *242*(4).

[60] Kocks, U. F., C. N. Tome, H.-R. Wenk, et al. (1998), Texture and Anisotropy. Preferred Orientations in Polycrystals and Their Effect on Material Properties, *Cambridge University, Cambridge.*

[61] Kumar, A., and V. Sundararaghavan (2017), Simulation of magnetostrictive properties of galfenol under thermomechanical deformation, *Finite Elements in Analysis and Design*, *127*, 1 – 5.

[62] Kumar, A., L. Nguyen, M. DeGraef, and V. Sundararaghavan (2016), A markov random field approach for microstructure synthesis, *Modelling and Simulation in Materials Science and Engineering*, *24*(3), 035,015.

[63] Lee, S., and V. Sundararaghavan (2010), Calibration of nanocrystal grain boundary model based on polycrystal plasticity using molecular dynamics simulations, *International Journal for Multiscale Computational Engineering*, *8*(5), 509–522.

[64] Lewis, A. C., S. M. Qidwai, and A. B. Geltmacher (2010), Slip systems and initiation of plasticity in a body-centered-cubic titanium alloy, *Metallurgical and Materials Transactions A*, *41*(10), 2522–2531.

[65] Liu, R., A. Kumar, Z. Chen, A. Agrawal, V. Sundararaghavan, and A. Choudhary (2015), A predictive machine learning approach for microstructure optimization and materials design, *Scientific reports*, *5*(11551), 1 – 12.

[66] Lloyd, S. (1982), Least squares quantization in PCM, *IEEE transactions on information theory*, *28*(2), 129–137.

[67] Ma, A., F. Roters, and D. Raabe (2006), A dislocation density based constitutive model for crystal plasticity FEM including geometrically necessary dislocations, *Acta Materialia*, *54*(8), 2169–2179.

[68] Martin, É., L. Jiang, S. Godet, and J. J. Jonas (2009), The combined effect of static recrystallization and twinning on texture in magnesium alloys AM30 and AZ31, *International journal of materials research*, *100*(4), 576–583.

[69] Martin, G., C. W. Sinclair, and R. A. Lebensohn (2014), Microscale plastic strain heterogeneity in slip dominated deformation of magnesium alloy containing rare earth, *Materials Science and Engineering: A*, *603*, 37–51.

[70] Matouš, K., and A. M. Maniatty (2004), Finite element formulation for modelling large deformations in elasto-viscoplastic polycrystals, *International Journal for Numerical Methods in Engineering*, *60*(14), 2313–2333.

[71] Mehlhorn, K., and K. Simon (1985), Intersecting two polyhedra one of which is convex, in *Fundamentals of Computation Theory*, pp. 534–542, Springer.

[72] Mika, D., and P. Dawson (1999), Polycrystal plasticity modeling of intracrystalline boundary textures, *Acta Materialia*, *47*(4), 1355–1369.

[73] Nie, J.-F. (2012), Precipitation and hardening in magnesium alloys, *Metallurgical and Materials Transactions A*, *43*(11), 3891–3939.

[74] Nielsen, S. F., E. Lauridsen, D. J. Jensen, and H. Poulsen (2001), A three-dimensional X-ray diffraction microscope for deformation studies of polycrystals, *Materials Science and Engineering: A*, *319*, 179–181.

[75] Nyberg, S. N. M. E. A. (2014), Magnesium alloys in US military applications: Past, Current and Future Solutions.

[76] Okabe, A. (1992), *Spatial tessellations*, Wiley Online Library.

[77] o'Rourke, J., A. J. Mallinckrodt, et al. (1995), Computational geometry in C, *Computers in Physics*, *9*(1), 55–55.

[78] Panozzo, R., and H. Hurlimann (1983), A simple method for the quantitative discrimination of convex and convex-concave lines, *Microscopica Acta*, *87*(2), 169–176.

[79] Panwar, S., S. Sun, and V. Sundararaghavan (2016), Modeling fatigue failure using the variational multiscale method, *Engineering Fracture Mechanics*, *162*, 290 – 308.

[80] Parisot, R., S. Forest, A.-F. Gourgues, A. Pineau, and D. Mareuse (2000), Modeling the mechanical behavior of a multicrystalline zinc coating on a hot-dip galvanized steel sheet, *Computational Materials Science*, *19*(1), 189–204.

[81] Qidwai, M. S., A. C. Lewis, and A. B. Geltmacher (2009), Using image-based computational modeling to study microstructure–yield correlations in metals, *Acta Materialia*, *57*(14), 4233–4247.

[82] Quey, R., P. Dawson, and F. Barbe (2011), Large-scale 3D random polycrystals for the finite element method: Generation, meshing and remeshing, *Computer Methods in Applied Mechanics and Engineering*, *200*(17), 1729–1745.

[83] Raeisinia, B., S. R. Agnew, and A. Akhtar (2011), Incorporation of solid solution alloying effects into polycrystal modeling of Mg alloys, *Metallurgical and Materials Transactions A*, *42*(5), 1418–1430.

[84] Sarma, G. B., B. Radhakrishnan, and P. R. Dawson (2002), Mesoscale modeling of microstructure and texture evolution during deformation processing of metals, *Advanced Engineering Materials*, *4*(7), 509–514.

[85] Schoenberg, F. P., T. Ferguson, and C. Li (2003), Inverting dirichlet tessellations, *The Computer Journal*, *46*(1), 76–83.

[86] Schreier, H., J.-J. Orteu, and M. A. Sutton (2009), *Image correlation for shape, motion and deformation measurements*, Springer US.

[87] Schumann, S., and H. E. Friedrich (2003), Current and future use of magnesium in the automobile industry, in *Materials Science Forum*, vol. 419, pp. 51–56, Trans Tech Publ.

[88] Soppa, E., P. Doumalin, P. Binkele, T. Wiesendanger, M. Bornert, and S. Schmauder (2001), Experimental and numerical characterisation of in-plane deformation in two-phase materials, *Computational Materials Science*, *21*(3), 261–275.

[89] Stanford, N., and M. Barnett (2008), The origin of "rare earth" texture development in extruded Mg-based alloys and its effect on tensile ductility, *Materials Science and Engineering: A*, *496*(1), 399–408.

[90] Stanford, N., R. Cottam, B. Davis, and J. Robson (2014), Evaluating the effect of yttrium as a solute strengthener in magnesium using in situ neutron diffraction, *Acta materialia*, *78*, 1–13.

[91] Staroselsky, A., and L. Anand (2003), A constitutive model for hcp materials deforming by slip and twinning: application to magnesium alloy AZ31B, *International journal of Plasticity*, *19*(10), 1843–1864.

[92] Sun, S., and V. Sundararaghavan (2012), A probabilistic crystal plasticity model for modeling grain shape effects based on slip geometry, *Acta Materialia*, *60*(13), 5233–5244.

[93] Sun, S., and V. Sundararaghavan (2014), A peridynamic implementation of crystal plasticity, *International Journal of Solids and Structures*, *51*(19), 3350–3360.

[94] Sun, S., and V. Sundararaghavan (2016), Modeling crack propagation in polycrystalline microstructure using variational multiscale method, *Mathematical Problems in Engineering*, *2016*(4715696), 1 – 14.

[95] Sundararaghavan, V. (2014), Reconstruction of three-dimensional anisotropic microstructures from two-dimensional micrographs imaged on orthogonal planes, *Integrating Materials and Manufacturing Innovation*, *3*(1), 19.

[96] Sundararaghavan, V., and A. Kumar (2012), Probabilistic modeling of microstructure evolution using finite element representation of statistical correlation functions, *International Journal of Plasticity*, *30*, 62 – 80.

[97] Sundararaghavan, V., and A. Waas (2011), Non-local continuum modeling of carbon nanotubes: Physical interpretation of non-local kernels using atomistic simulations, *Journal of the Mechanics and Physics of Solids*, *59*(6), 1191 – 1203.

[98] Sundararaghavan, V., and N. Zabaras (2004), A dynamic material library for the representation of single-phase polyhedral microstructures, *Acta Materialia*, *52*(14), 4111 – 4119.

[99] Sundararaghavan, V., and N. Zabaras (2005), Classification and reconstruction of three-dimensional microstructures using support vector machines, *Computational Materials Science*, *32*(2), 223 – 239.

[100] Sundararaghavan, V., and N. Zabaras (2005), On the synergy between texture classification and deformation process sequence selection for the control of texture-dependent properties, *Acta Materialia*, *53*(4), 1015 – 1027.

[101] Sundararaghavan, V., and N. Zabaras (2006), Design of microstructure-sensitive properties in elasto-viscoplastic polycrystals using multi-scale homogenization, *International Journal of Plasticity*, *22*(10), 1799 – 1824.

[102] Sundararaghavan, V., and N. Zabaras (2007), Linear analysis of texture–property relationships using process-based representations of rodrigues space, *Acta Materialia*, *55*(5), 1573 – 1587.

[103] Sundararaghavan, V., and N. Zabaras (2008), A multi-length scale sensitivity analysis for the control of texture-dependent properties in deformation processing, *International Journal of Plasticity*, *24*(9), 1581–1605.

[104] Sundararaghavan, V., and N. Zabaras (2009), A statistical learning approach for the design of polycrystalline materials, *Statistical Analysis and Data Mining*, *1*(5), 306–321.

[105] Sundararaghavan, V., A. Kumar, and S. Sun (2015), Crystal plasticity simulations using nearest neighbor orientation correlation function, *Acta Materialia*, *93*, 12–23.

[106] Sutton, M. A., N. Li, D. Garcia, N. Cornille, J. Orteu, S. McNeill, H. Schreier, X. Li, and A. P. Reynolds (2007), Scanning electron microscopy for quantitative small and large deformation measurements part II: experimental validation for magnifications from 200 to 10,000, *Experimental Mechanics*, *47*(6), 789–804.

[107] Sutton, M. A., N. Li, D. Joy, A. P. Reynolds, and X. Li (2007), Scanning electron microscopy for quantitative small and large deformation measurements part I: SEM imaging at magnifications from 200 to 10,000, *Experimental mechanics*, *47*(6), 775–787.

[108] Suzuki, A., and M. Iri (1986), Approximation of a tessellation of the plane by a Voronoi diagram., *J. OPER. RES. SOC. JAPAN.*, *29*(1), 69–97.

[109] Teodosiu, C., J. Raphanel, L. Tabourot, C. Teodosiu, and F. Sidoroff (1993), Large Plastic Deformations MECAMAT'91.

[110] Thiessen, A. H. (1911), Precipitation averages for large areas, *Monthly weather review*, *39*(7), 1082–1089.

[111] Thornburg, D., and H. Piehler (1975), An analysis of constrained deformation by slip and twinning in hexagonal close packed metals and alloys, *Metallurgical and Materials Transactions A*, *6*(8), 1511–1523.

[112] Tomé, C., R. A. Lebensohn, and U. Kocks (1991), A model for texture development dominated by deformation twinning: application to zirconium alloys, *Acta metallurgica et materialia*, *39*(11), 2667–2680.

[113] Trinchet-Almaguer, D., and H. Pérez-Rosés (2007), Algorithm for Solving the Generalized Inverse Voronoi Problem, *Revista Cubana de Ciencias Informaticas*, *1*(4), 58–71.

[114] Uesugi, T., and K. Higashi (2005), Materials design for high-strength Mg-based alloys by understanding from ab initio calculation, in *Materials Science Forum*, vol. 488, pp. 131–134, Trans Tech Publ.

[115] Van Houtte, P. (1978), Simulation of the rolling and shear texture of brass by the Taylor theory adapted for mechanical twinning, *Acta Metallurgica*, *26*(4), 591–604.

[116] Voronoï, G. (1908), Nouvelles applications des paramètres continus à la théorie des formes quadratiques. Deuxième mémoire. Recherches sur les parallélloèdres primitifs., *Journal für die reine und angewandte Mathematik*, *134*, 198–287.

[117] Wang, Y., and J. Huang (2003), Texture analysis in hexagonal materials, *Materials Chemistry and Physics*, *81*(1), 11–26.

[118] Zabaras, N., V. Sundararaghavan, and S. Sankaran (2006), An information theoretic approach for obtaining property pdfs from macro specifications of microstructural uncertainty, *TMS letters*, *3*(1), 1 – 4.

[119] Zeghadi, A., S. Forest, A.-F. Gourgues, and O. Bouaziz (2007), Ensemble averaging stress–strain fields in polycrystalline aggregates with a constrained surface microstructure–Part 2: Crystal plasticity, *Philosophical Magazine*, *87*(8-9), 1425–1446.

[120] Zeghadi, A., F. N'guyen, S. Forest, A.-F. Gourgues, and O. Bouaziz (2007), Ensemble averaging stress–strain fields in polycrystalline aggregates with a constrained surface microstructure–Part 1: Anisotropic elastic behaviour, *Philosophical Magazine*, *87*(8-9), 1401–1424.

[121] Zhang, C., H. Li, P. Eisenlohr, W. Liu, C. Boehlert, M. Crimp, and T. Bieler (2015), Effect of realistic 3D microstructure in crystal plasticity finite element analysis of polycrystalline Ti-5Al-2.5 Sn, *International Journal of Plasticity*, *69*, 21–35.